THERMAL TRANSPORT IN INDIVIDUAL NANOWIRES OF FINE STRUCTURES

By

QIAN ZHANG

Dissertation
Submitted to the Faculty of the
Graduate School of Vanderbilt University
in partial fulfillment of the requirements
for the degree of

DOCTOR OF PHILOSOPHY
in
Mechanical Engineering
August 11, 2017
Nashville, Tennessee

Approved:

Deyu Li, Ph.D.
Robert W. Pitz, Ph.D.
Weng Poo Kang, Ph.D.
D. Greg Walker, Ph.D.
Yaqiong Xu, Ph.D.

Dedicated to Chumei Wang

ACKNOWLEDGEMENTS

First of all, I want to thank my advisor, Dr. Deyu Li, for his consistent patience, insightful guidance, and support throughout my six years at Vanderbilt. Before coming to Vanderbilt, I did not know much about nanoscience and nanotechnology. Now I am proceeding to defend my Ph.D. in nanoscale heat transfer. None of these will happen without Dr. Li. His dedication, passion, and sharp insights, that have opened my eyes, extended my horizon, and greatly shaped this dissertation work to its current form. The lessons I have learnt from Dr. Li will be a valuable asset and help me to tackle future challenges.

Next, I want to thank my collaborators who have shared their excellent work and expertise with me and helped to push forward our projects, that have resulted in publications in high quality journals, a feat I could not imagine back to six years ago.

I also would like to thank my labmates, who have shared my joys and failures, and encouraged me to pursue the path. The road has been bumpy, full of ups and downs. You have made this journey enjoyable and much more pleasant than I could imagine.

Last but not the least, I want to thank my family for their support, giving me the courage to embark on this difficult yet fruitful path. Your love and support have made me a stronger person, who is now ready to face the life beyond.

TABLE OF CONTENTS

Page

Chapter

LIST OF FIGURES

Figure Page

1. Introduction

Nanowires could possess unique thermophysical properties due to both classical and quantum confinement effects on electrons and phonons (Dresselhaus et al. 2007, Lin & Dresselhaus 2003, Shi 2012, Yan et al. 2009). Studying phonon transport through these nanowires is of both fundamental scientific and practical engineering significance. Therefore, the thermal transport property of nanowires has fueled widespread interest and significant amount of efforts have been devoted to related theoretical, experimental, and numerical studies (Cahill et al. 2003, 2014; Li & McGaughey 2015). Importantly, the unique thermophysical properties of nanowires are closely associated with their structures. Therefore, understanding of the relations between structures and transport properties of nanowires is essential for engineering the thermal properties of nanowires for various demands. One particular example of great interest in the past two decades is to reduce the nanowire thermal conductivity for thermoelectric energy conversion (Lan et al. 2010).

In view of the crucial structure-transport property relations for nanowires, this dissertation seeks to experimentally extract the thermal conductivity of several different kinds of nanofibers and nanowires, whose structures have been carefully characterized. In the introduction section, we first briefly review the pioneering work that has been done to study thermal transport through individual nanowires and the development of nanowires of interesting structures.

1.1 Phonon Transport in Nanowires

Even before experimental studies were conducted, thermal transport through nanowires had attracted some attention and a molecular dynamics (MD) study predicted orders of magnitude reduction for the thermal conductivity of silicon nanowires. Such dramatic reduction may arise from different factors including i) escalated phonon boundary scattering, and ii) modified phonon dispersion relation (Volz & Chen 1999). The first systematic measurement of the thermal conductivity of nanowires was conducted on different diameter silicon nanowires by Li et al. with a suspended micro-bridge platform as shown by a Scanning Electron Microscope (SEM) micrograph in **Figure 1.1(c)** (Li et al. 2003b, Shi et al. 2003). The measured thermal conductivity of individual 22, 37, 56, and 115 nm diameter silicon nanowires were significantly smaller than the corresponding bulk value and exhibited a strong diameter dependence, with lower thermal conductivity for smaller diameter wires, as shown in **Figure 1.1(a)**.

The measured Si nanowires were prepared by the Vapor-Liquid-Solid (VLS) method and Transmission Electron Microscopy (TEM) examination of these nanowires indicated their single crystalline nature (Li et al. 2003b). The results clearly demonstrate strong suppression of phonon transport by boundary scattering in single crystalline Si nanowires. Interestingly, the thermal conductivity of the 22 nm Si nanowire deviates from the Debye T^3 dependency at low temperature, showing a linear temperature dependence, which suggests that at that scale, size effects beyond boundary scattering could play an important role (Li et al. 2003b).

To further examine phonon transport in thin silicon nanowires (<30 nm), Chen et al. fabricated small diameter silicon nanowires by either thermally oxidizing large diameter wires and then removing the oxide layer or directly synthesizing thin Si nanowires from 9 nm diameter Pt nanoparticles through the VLS growth method (Chen et al. 2008). The obtained thermal conductance of the thin Si nanowires scales linearly with temperature in the range of 20 to 100K, showing similar trends as the 22 nm Si nanowire measured by Li et al. (Li et al. 2003b). They presented a model based on Landauer expression and showed satisfactory fitting with the experimental data at low temperatures. It is claimed that the linear dependence of thermal conductivity on temperature was due to frequency-dependent phonon boundary scattering. The contribution from specularly reflected phonons could not be neglected in thin Si nanowires case and the competition between different modes gives rise to the unique temperature dependence in thin Si nanowires.

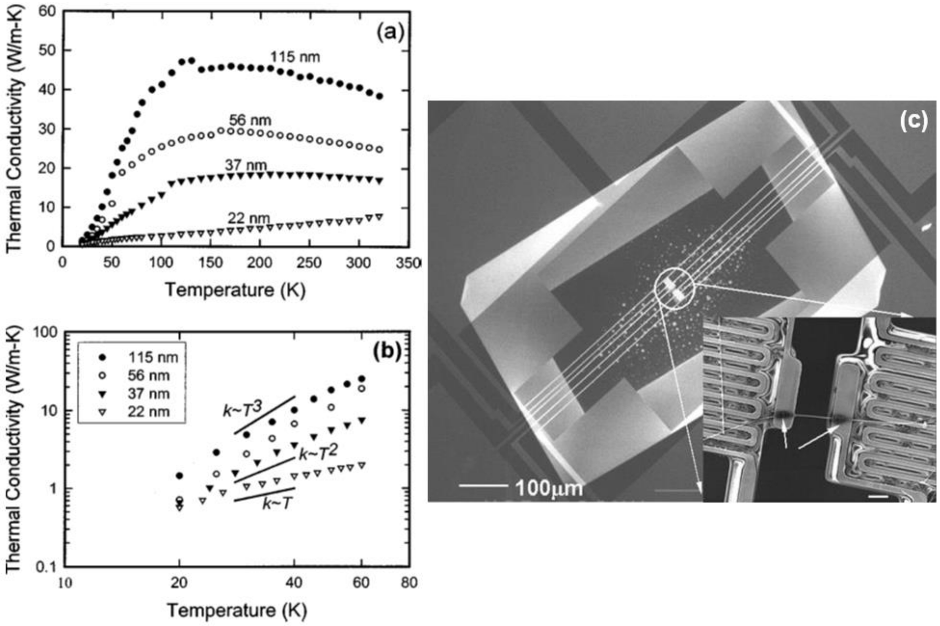

Figure 1.1 Thermal conductivity of silicon nanowires and the used microdevice for thermal measurement (Li et al. 2003b). (a) Measured thermal conductivity of different diameter Si nanowires. The number besides each curve denotes the corresponding wire diameter. (b) Low temperature experimental data on a logarithmic scale. Also shown are T^3, T^2, and T^1 curves for comparison. (c) SEM images of the suspended micro-bridge device. The lower inset shows a 100 nm Si nanowire bridging the two side-by-side suspended membranes, with wire-membrane junctions wrapped with locally-deposited amorphous carbon (shown by arrows) to minimize the contact thermal resistance.

One experimental challenge is that the small thermal conductance of thin Si nanowires is approaching the limit of the 4-point I-V measurement technique. To address the issue of measuring lower thermal conductance, Wingert et al. modified the suspended micro-bridge set-up through introducing a reference device into the cryostat to form a Wheatstone bridge, which effectively cancels out the signal drift from the temperature fluctuation of the sample holder and pushed the detection limit down to a ~10 pW/K thermal conductance (Wingert et al. 2011, 2012). Armed with this powerful scheme, the thermal conductivity of thin Ge and SiGe core-shell nanowires were measured and while the thermal conductivity of large diameter nanowires could be well accounted for by theoretical modeling, the data for smaller diameter wires (~15 nm) deviated significantly from the prediction based on the classical size effect. The significant difference between the experimental data and theoretical prediction was attributed to the bulk-like phonon dispersion relation used in the modeling (Wingert et al. 2011). More recently, a study reported by Wingert et al. on thin silicon nanotubes (NTs) with wall thickness as thin as 5 nm showed a thermal conductivity reduction much stronger than that could be accounted for by diffuse boundary scattering. They found that the Young's modulus of these individual Si NTs could be 6-fold smaller than the bulk value, suggesting that there were strong elastic softening effects in the crystalline Si NTs, which led to much reduced phonon group velocity, and subsequently lower thermal conductivity (Kwon et al. 2016, Wingert et al. 2015).

The boundary effects of Si nanowires are more complicated in rough wires, which showed drastic reduction of thermal conductivity compared with VLS-grown Si nanowires of similar diameter (Hochbaum et al. 2008). The significant reduction was exploited to enhance the thermoelectric property of Si nanowires, achieving a thermoelectric figure of merit (ZT) over two orders of magnitude higher than the bulk value. The drastically reduced thermal conductivity triggered enormous interest in understanding the effects of rough boundaries. For example, Moore et al. employed Monte Carlo (MC) simulation to demonstrate that the sawtooth roughness of a nanowire could incur phonon backscattering and yield a thermal conductivity even lower than the fully diffusive surface limit (Moore et al. 2008). Similarly, Sansoz et al. showed through MD simulations of thermal transport in various surface faceted and circular nanowires that carefully sawtoothed nanowires with specific facet displayed a thermal conductivity considerably lower than that of smooth Si NWs (Sansoz 2011).

While most reported data on the thermal conductivity of Si nanowires have been performed at temperatures lower than 500 K, there is a recent effort to push the measurable temperature range up to 700 K, higher than the Debye temperature of Si (~645 K), with the implementation of a specially designed sample holder (Lee et al. 2016). With the optimized setup, they measured the thermal conductivity of both smooth VLS Si NWs and rough Si NWs in temperatures ranging from 20 K to 700 K. It was suggested that study of phonon transport in Si NWs at higher temperatures cannot simply neglect the contribution from optical phonons when they are fully excited and can contributes a considerable portion to their thermal conductivity. High frequency optical phonons scatter much more frequently than their acoustic counterparts, which possess longer phonon mean free path. Therefore, acoustic phonons suffer stronger phonon boundary scattering in nanowires; and the relative contribution to thermal transport from acoustic phonons decreases with reducing diameters, which renders optical phonons more important. Furthermore, their work on rough Si NWs further confirms the importance of surface roughness in reducing the thermal conductivity in measured temperature range.

Beyond Si nanowires, thermal transport in various other kinds of semiconductor nanowires has also been explored (Hsin et al. 2013, Lee et al. 2012, Martin et al. 2010, Moore et al. 2009, Shi et al. 2004). For example, using the same microfabricated platform as Li et al. (Li et al. 2003b), Shi et al. measured the thermal conductivity of 53 nm and 64 nm thick tin dioxide nanobelts (SnO_2) in a temperature range of 80-350 K. The measurements showed significantly lower thermal conductivities than the bulk values and modeling based on a full dispersion transmission function suggested the phonon-boundary scattering is the primary cause (Shi et al. 2004). Moore et al.

experimentally explored the thermal conductivity of a 232 nm single crystalline bismuth nanowire and polycrystalline bismuth nanowires of diameters ranging from 74-255 nm over a temperature range between 100 and 300 K, all showing notable reduction compared to bulk values, while the thermal conductivities of polycrystalline samples showed no noticeable dependence on diameter. Subsequent modelling determined that the grain boundary phonon scattering dominates over phonon boundary scattering, limiting the mean free path within a range of 15-40 nm, significantly smaller than the nanowire diameter (Moore et al. 2009). Lee et al. measured thermal conductivity of SiGe alloy nanowires and simultaneously probed the electrical conductivity and Seebeck coefficient. Despite the strong impurity scattering in SiGe nanowires, the phonon boundary scattering is still pronounced and gives rise to a thermal conductivity as low as ~1.2 W/m-K at 450 K, considerably lower than the corresponding bulk value, which lift the ZT up to ~0.46 at 450 K (Lee et al. 2012).

To model thermal transport in surface-roughened GaAs and Ge nanowires, Martin et al. proposed a method based on Holland’s formalism on the basis of a full phonon dispersion relation and quantified the effect of the surface roughness based on a perturbation theory. They found that the thermal conductivity in rough Ge and GaAs nanowires with diameters smaller than 200 nm can be modulated by adjusting the surface roughness, which could yield a thermal conductivity as low as 0.1 W/m-K for a 56 nm rough Ge nanowire with a root-mean-square (RMS) roughness of 3 nm (Martin et al. 2010). In general, the thermal conductivity of semiconductor nanowires is significantly reduced due to phonon boundary scattering. In conjunction with preserving/enhancing electrical conductivity and Seebeck coefficient, nanowires could make a class of promising materials for thermoelectric applications (Dresselhaus et al. 2007, Kim 2011).

In addition to crystalline inorganic nanowires, another type of nanowires, or more commonly referred to as nanofibers, are made of polymers and recently witness resurging interests in engineering their thermal conductivity. Polymers are composed of long molecular chains with each chain consisting of repeated structural units called monomers. The process of connecting the monomer units together in a chemical reaction to form polymer chains or three-dimensional (3D) networks is termed polymerization. Polymeric materials have found widespread applications in modern civilization, such as structural materials for various products ranging from bicycles to airplanes and rockets. In spite of many advantages polymeric materials boast of, one limiting factor is their low thermal conductivity (Henry 2014). This poor thermal property poses enormous challenges for their usage in applications such as flexible electronics, photovoltaic energy conversion, and advanced structural materials mounted with high power electronics.

Bulk polymers usually possess extremely low thermal conductivity on the order of 0.1 W/m-K, which is due to the randomly aligned and entangled polymer chains and voids. However, the intra-chain heat conduction along each polymer chain can be in fact very efficient, because of the strong covalent bonds between atoms in each chain. The issue is that inter-chain heat transfer is much less efficient, resulting from the weak van der Waals (vdW) interactions (Henry 2014). As such, the polymer chains, if aligned, could lead to dramatic enhancement in both thermal conductivity and mechanical strength. It has been found that polyethylene (PE) films with highly aligned chains attained from mechanical stretching can have a much higher thermal conductivity, up to 40 W/m-K, as well as a Young's modulus significantly larger than the typical bulk value (Choy 1977, Choy & Leung 1983, Choy et al. 1999).

More strikingly, recent MD simulations predicted a thermal conductivity as high as 350 W/m-K or even divergent thermal conductivity for a single chain of PE (Henry & Chen 2008, Jiang et al. 2012a), which has been supported by subsequent experimental measurements of ultra-drawn PE nanofibers, yielding a thermal conductivity value of ~104 W/m-K (Shen et al. 2010). Using a time-domain thermoreflectance (TDTR) method, Wang et al. measured the thermal conductivities of several commercially available high-modulus polymer fibers (Wang et al. 2013). Their results indicate that liquid crystalline p-phenylene benzobisoxazole (PBO) fibers have the highest room temperature thermal conductivity of ~20 W/m-K, surpassing the thermal conductivity of commercially available highly crystalline PE. One more interesting result on polythiophene nanofibers (Singh et al. 2014) shows that, despite remaining mostly amorphous, aligned pure polythiophene nanofibers can have a thermal conductivity up to ∼4.4 W/m-K (more than 20 times higher than the bulk polymer value). These pioneering studies strongly suggest that the thermal conductivity of a polymeric material is closely related to its microstructure, particularly the molecular chain orientation and crystallinity.

The highest experimentally observed thermal conductivity of polymers is demonstrated by Shen et al. (Shen et al. 2010) through drawing single crystalline PE nanofibers using a tipless bi-layer (Si_3N_4/Au) atomic force microscope (AFM) tip, achieving a drawing ratio up to 400. The resulted nanofibers are in a diameter range from 50 to 500 nm. The thermal measurement was carried out with the AFM cantilever serving as a temperature sensor and the highest measured value is 104 W/m-K at a drawing ratio of 400, the highest ever achieved with polymers, as shown in **Figure 1.2**. The exciting results stimulate great interests in quest of highly heat conducting polymers and show the potential of engineering polymer chains at the molecular level for practical purposes.

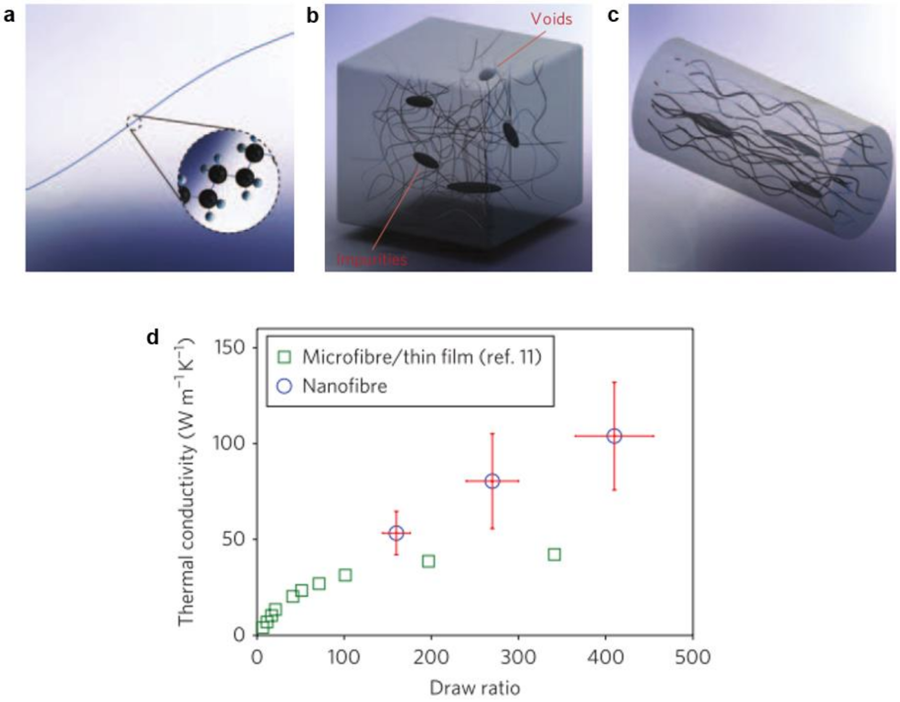

Figure 1.2 Illustration of polyethylene (PE) chains and fibers and measured thermal conductivity of the ultradrawn nanofibers (Shen et al. 2010). (a) One single molecular chain of PE. The inset shows the chemical structure of PE (carbon atoms are of black color and hydrogen atoms are of white color). (b) Chain ends, entanglements, voids, and defects in bulk PE. (c) Stretched PE microfiber. (d) Measured thermal conductivity of individual PE nanofibers versus their corresponding draw ratios, in comparison with drawn bulk PE thin films.

Although the ultra-drawing method is capable of producing nanofibers of high thermal conductivity, the yield is too low to be implemented in bulk fabrication for practical purposes. Alternatively, electrospinning has proven to produce large quantities of micro/nanoscale fibers of high aspect ratio with aligned molecular chain in high throughput (Greiner & Wendorff 2007). In electrospinning, a very high voltage is applied between the needle of a syringe containing polymer solutions and a grounded collector. As a result, a high electric field is exerted on the solution travelling towards the collector, leading to a strong force that facilitates the formation of chain-aligned polymer fibers. For instance, Zhong et al. fabricated electrospun nylon-6 nanofibers under a voltage of 6-7 KV and demonstrated an increasing thermal conductivity trend with decreasing diameter, achieving nearly one order of magnitude enhancement compared to the bulk nylon value. The enhancement was mainly attributed to the significantly promoted chain alignment and crystallites orientation, rather than the increasing crystallinity (Zhong et al. 2014). It is worth noting that hot-stretching of the as-spun nanofibers can further boost the thermal conductivity, as shown in **Figure 1.3**, indicating the potential for further improvement of the thermal transport properties of electrospun nanofibers by mechanical drawing at elevated temperatures.

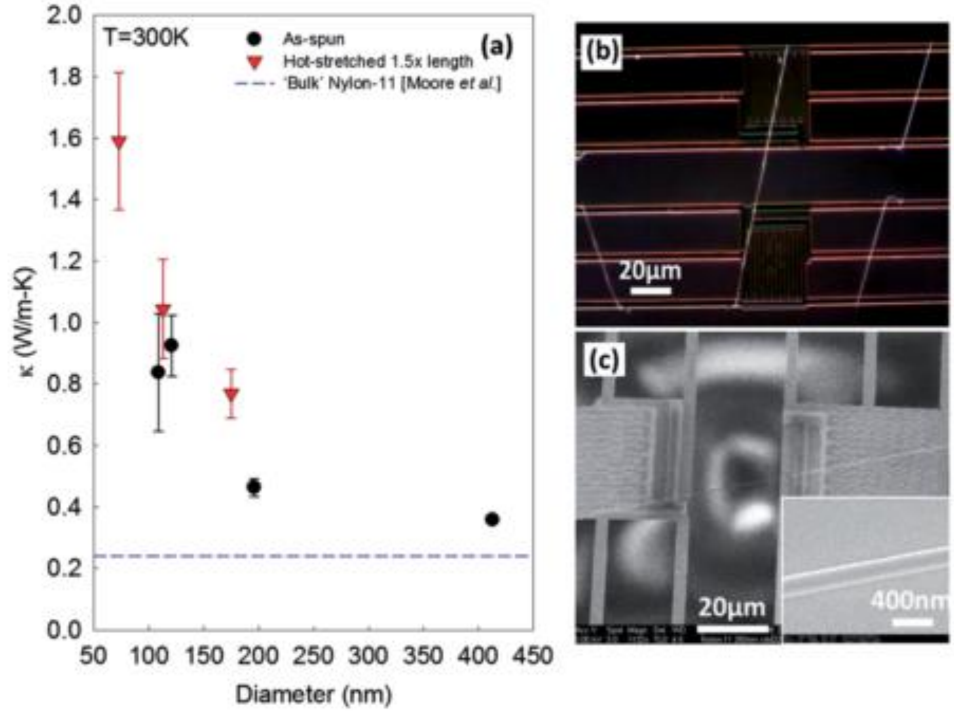

Figure 1.3 Thermal conductivity of electrospun Nylon-6 nanofibers. (a) Thermal conductivity versus nanofiber diameter at 300 K (Zhong et al. 2014). Black circles represent as-spun nanofibers and red triangles represent nanofibers hot-stretched to 1.5× original length. The thermal conductivity of all samples increases as the diameter decreases, with a larger increase for hot-stretched nanofibers. The blue dashed line stands for the bulk Nylon-11 thermal conductivity. (b) A dark-field optical image of nanofibers on a suspended micro-device for thermal measurement. (c) An SEM micrograph of the same fiber in (b) with the inset of a close-up of the fiber segment on the supporting pad.

More recently, Canetta et al. presented values ranging from 6.6 W/m-K to 14.4 W/m-K for electrospun polystyrene nanofibers (Canetta et al. 2014). Aside from the efforts to realize better aligned polymers, other efforts invested in enhancing inter-chain interactions witnessed thermal conductivity enhancement as well. Kim et al. achieved a significant increase of *k* through the introduction of dense and continuous inter-chain bonds in amorphous polymer blends (Kim et al. 2014). These pioneering results indicate the potential of exploring the upper limits of the thermal conductivity of polymer nanofibers for various applications.

Polymers with single crystalline structure and perfectly aligned molecular chains belong to one group of vdW materials, usually termed quasi-one-dimensional (quasi-1D) vdW materials. Such structure boasts of strongly anisotropic bonding, which leads to thermal transport behavior that can be drastically different from the case of semiconductor nanowires, which are relatively isotropic and usually have a dramatically reduced thermal conductivity owing to phonon boundary scattering. In contrast, one MD study on thermal conductivity of PE revealed that, as the dimensionality of PE transitions from 1D to 2D and then 2D to 3D, the thermal conductivity gradually decreases to the bulk value, with a single PE chain possessing the highest thermal conductivity of 150 W/m-K. This different size dependence was attributed to increased anharmonic scattering brought by extra phonon modes when size increases (Henry et al. 2010). The absence of phonon boundary scattering in aligned polymer chains originates from the strong phonon focusing effect, which guides majority of the phonons to travel predominately along chain direction rather than to travel randomly. The combination of these uniquenesses could give rise to a divergent thermal conductivity along a single PE molecular chain, as demonstrated by increasing thermal conductivity with chain length (Henry & Chen 2008, 2009).

Despite the lack of experimental reports on thermal transport in intrinsically 1D system, one particular material, single-walled carbon nanotubes (SWCNTs), have received considerable attention. As an ideal 1D material system, experimental measurements have shown that thermal conductivity of SWCNTs can be as high as ~3500 W/m-K at room temperature for an SWCNT of 2.6 µm long and 1.7 nm in diameter (Pop et al. 2006). Theoretically, it has been predicted that their thermal conductivity can be as high as 6600 W/m-K, about three times that of the diamond. This superior thermal conductivity partly stems from the absence of boundary scattering, which preserves a large phonon mean free path (Berber et al. 2000). Experimentally, employing a Raman thermal measurement technique, Liu et al. determined a ballistic phonon transport length up to ~10 µm in SWCNT at 360 K (Liu et al. 2017). However, in contrast to the explosive interests their 2D counterparts have triggered recently, the thermal properties of intrinsically 1D material systems have been large understudied. More work remains to be done to fully explore their potentials and pave the way for their practical applications.

1.2 Nanowires of Complex Structures

Other than polymer nanofibers, most research on thermal transport through nanowires has been conducted on wires of simple straight configurations and single crystalline structure. However, advances in synthesis methods have enabled preparation of nanowires of more complex morphologies for novel devices and applications (He et al. 2015; Jiang et al. 2011, 2012b; Tian et al. 2009), and thermal transport properties of these nanowires have not been characterized experimentally so far.

One class of nanowires are those with stacking faults between crystalline planes. For example, Caroff et al. (Caroff et al. 2009) have synthesized InAs nanowires with controlled twin planes similar to the structure of superlattices. The approach also shows the capability of growing polytypic nanowires that comprise of alternating segments of different crystal phases. Different crystal phases of the same materials could lead to different transport properties. Many binary compounds made from III-V materials, for example, InAs, GaAs, GaP and InP, can grow into two different crystal phases, i.e., the wurtzite (WZ) and the zinc blende (ZB) phase. Although there have been no experimental reports on thermal transport properties of nanowires with mixed crystal phases, Thelander et al. (Thelander et al. 2011) have conducted electrical resistivity measurements of these InAs nanowires. They have achieved rational synthesis of superlattice-like nanotwinned InAs nanowires with mixed crystal phases, grown by metal-organic vapor phase epitaxy (MOVPE) and molecular beam epitaxy (MBE), as shown in **Figure 1.4**. The electrical resistivity measurements indicate that the nanowires of mixed crystal phases exhibit a resistivity up to 2 orders of magnitude larger than that of single phase nanowires.

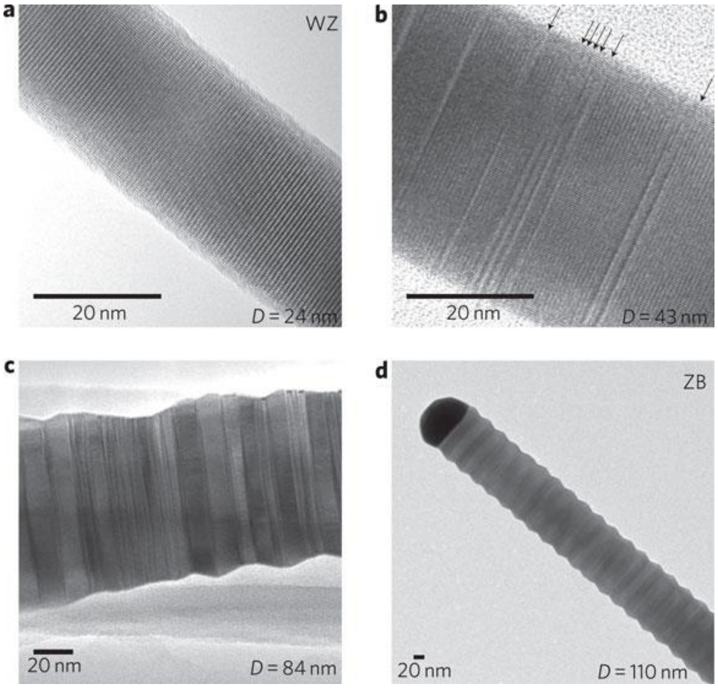

Figure 1.4 Crystal structure of InAs nanowires changes from wurtzite (WZ) to zinc blende (ZB) as the wire diameter increases (Caroff et al. 2009). (a–d), TEM images viewed along the <110> zone axis (zinc blende notation), from (a) to (d), with increased diameter, the crystal structure changes progressively from (a) pure WZ, to (b) WZ with single stacking faults, which are noted by arrows, to (c) a mixed WZ–ZB structure, and finally to (d) pure ZB.

Synthesis of nanowires with kinks or curvatures has also been realized. For example, Tian et al. (Tian et al. 2009) first demonstrated the rational design and synthesis of both silicon and germanium single crystalline kinked nanowires. They further achieved dopant-modulated structures that have the properties of p-n diodes and field effect transistors, which could have many interesting applications. For example, Jiang et al. and Qing et al. implemented kinked silicon nanowires as encoded field-effect transistors to record action potentials intracellularly (Jiang et al. 2012b, Qing et al. 2013). Pevzner et al. further developed an on-surface confinement-guided nanowire growth method that enables a perfect control over their geometry, as demonstrated by the growth of Si, Ge, and SiGe nanowires with different shapes in pre-patterned trenches via the VLS mechanism, as depicted in **Figure 1.5**. The successful synthesis of any kinked (variable turning angles), sinusoidal, linear, and spiral shaped nanowires illustrates the power of this approach to grow nanowires of any other desirable shapes (Pevzner et al. 2012).

The nanowires synthesized by Jiang et al. demonstrated the capability of rational growth of branched nanowire heterostructures based on bare nanowires or core-shell nanowires, termed as type I and type II in their paper (Jiang et al. 2011). Basically, Au nanoparticles were deposited onto the surface of the base nanowires, and then they serve as seeds/catalysts to guide the growth of the branched nanowires, as shown in **Figure 1.6**.

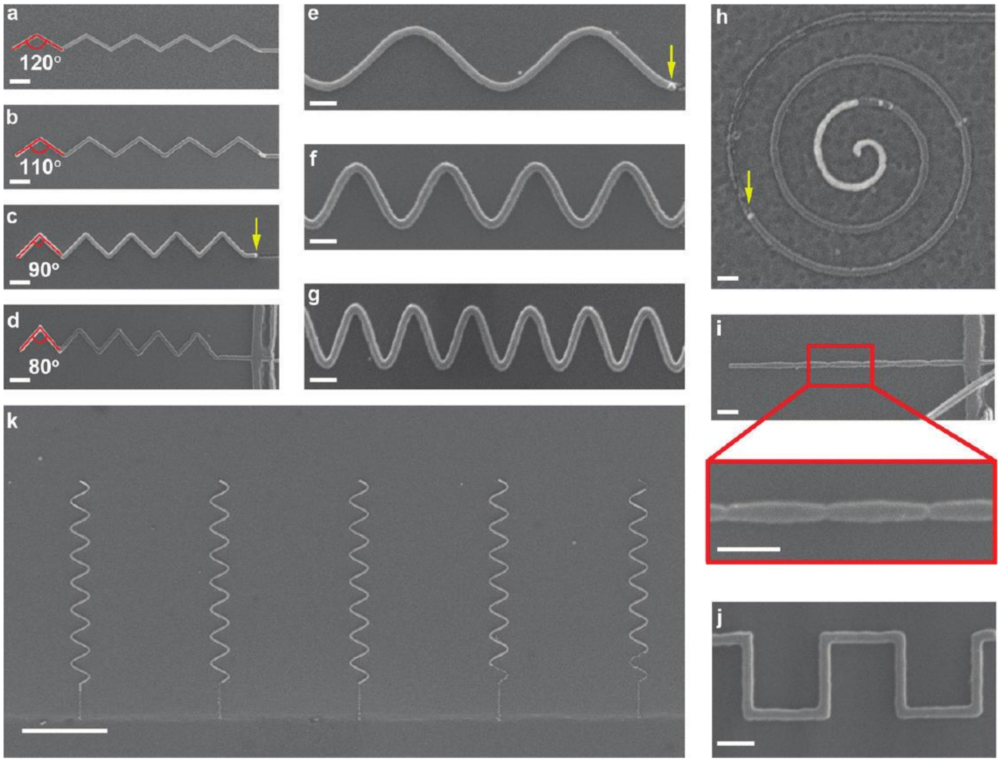

Figure 1.5 SEM images of synthesized nanowires with various two dimensional shapes (Pevzner et al. 2012). (a−d) SEM images of multiple kinked two-dimensional Si nanowires with different turning angles from 120° to 80°. The yellow arrow (panel c) indicates the position of the catalyst. The scale bars are 250 nm. (e−g) SEM images of sinusoidal shaped two-dimensional silicon nanowires with different periods. The yellow arrow (panel e) highlights the position of the nanocluster catalyst. The scale bars are 250 nm. (h) An SEM image of a two-dimensional spiral shape Si nanowire. The yellow arrow highlights the position of the nanocluster catalyst. The scale bar is 250 nm. (i) An SEM image of a 1D shape-controlled SiNW, by modulation of nanotunnel shape along the growth direction. The scale bar is 250 nm (zoom-in image, scale bar is 250 nm). (j) An SEM image of a square-wave shaped silicon nanowire. Scale bar is 250 nm. (k) An SEM image of a sample showing multiple sinusoidal-shaped silicon nanowires. Scale bar is 2.5 µm.

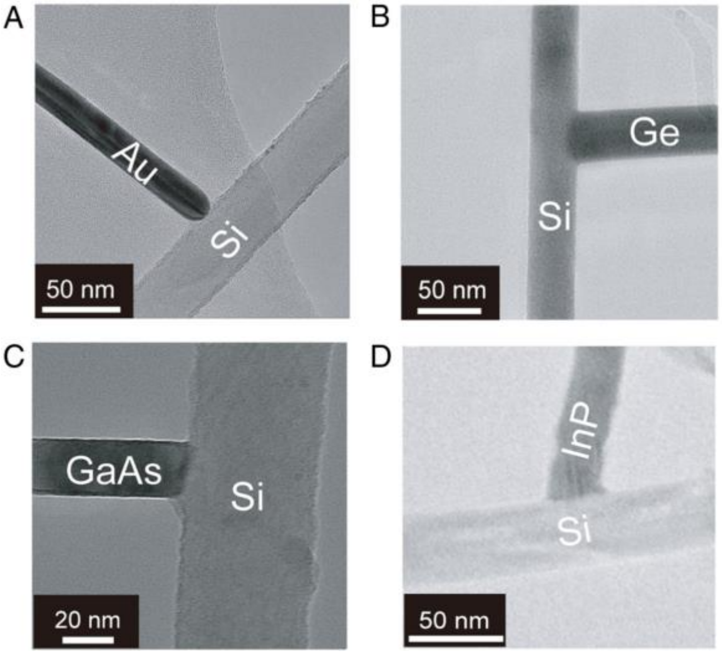

Figure 1.6 TEM images of different kinds of branched heterostructure nanowires (Jiang et al. 2011). The consisting materials are (A) Si/Au, (B) Si/Ge, (C) Si/GaAs, and (D) Si/InP.

Such nanowires of complex structures have also been predicted to possess a lot of potentials when it comes to modulating heat conduction and increasing thermoelectric performance. For example, MD simulation of the mechanical properties of kinked Si nanowires (k-SiNWs) projected a much larger fracture strain than that of straight Si nanowires (Jiang et al. 2013b). In terms of transport properties, Jiang et al. constructed an MD model of k-SiNWs of varying arm lengths and showed that the thermal conductivity of these wires could decrease up to 70% relative to that of the straight ones at room temperature, as shown in **Figure 1.7** (Jiang et al. 2013a). The significantly reduced thermal conductivity was ascribed to two mechanisms, i.e., (1) the resistance of interchanging between longitudinal and transverse phonon modes, and (2) the phonon pinching effect, which localized certain frequency of twisting and transverse phonon modes. Another study by Xiong et al. have studied similar kinked structure of SiNWs with a turning angle of 109.4° instead of 90° and found a similar level of thermal conductivity reduction up to 65% (Xiong et al.

2014). The kinked morphology induced thermal conductivity reduction could be combined with other currently known mechanisms to further reduce thermal conductivity, thus opening a new venue for enhancing the thermoelectric efficiency.

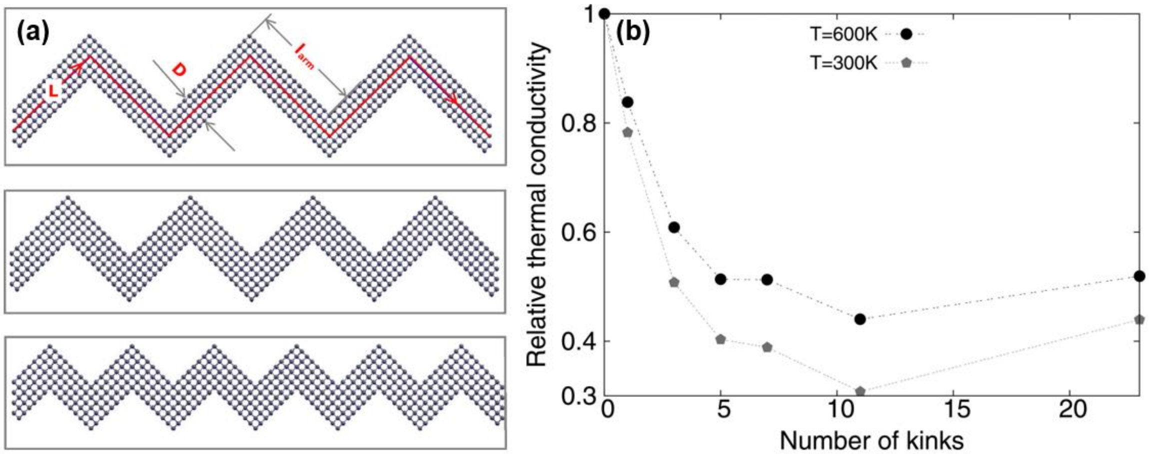

Figure 1.7 Thermal conductivity of kinked silicon nanowires from MD simulation. (a) Configurations of k-SiNWs with diameter D = 11.0 Å and axial length L = 190.0 Å. l_{arm} is the arm length. The numbers of kinks are 5, 7, and 11 in the structures from top to bottom. (b) Relative thermal conductivity versus number of kinks in k-SiNWs. The value of thermal conductivity for the corresponding straight SiNWs are 7.67 and 5.78 W/m-K at 300 and 600 K, respectively (Jiang et al. 2013a).

MD simulations of nanowires are normally limited to small dimensions with less than 10 nm diameter, constrained by the available computational capability. One study employing MC simulation to explore thermal transport in curved nanowires with a larger dimension ranging from 10 to 50 nm diameter suggested that curved nanowires with radius one order of magnitude smaller than the phonon MFP show a notable reduction of thermal conductivity compared to straight ones, resulting from the impedance of phonon ballistic transport (Liu et al. 2009). In addition, such curved nanowires could affect the thermoelectric property through another path as shown by other studies (Pye et al. 2015, Zhou & Yang 2011). Zhou et al. investigated ballistic thermoelectric transport in double-bend nanowires, showing that the quantum interference effects, incurred by the geometric confinement of the bent structure, could result in large Seebeck coefficients (Zhou & Yang 2011). Pye et al. further studied the thermoelectric transport in single, double and U-bend structures based on a quantum transport theory using Green's functions, predicting a ZT beyond unity. Moreover, the introduction of disorders could further enhance the ZT as the thermopower remains robust against moderate degrees of imperfections, such as disorders and surface roughness (Pye et al. 2015). Both studies indicated the potential of modulating thermoelectric transport with kinked or curved nanowires.

In addition to phase boundaries and kinks, crystalline defects, such as twin boundaries and stacking faults, have been observed among different kinds of nanowires grown by chemical vapor deposition (CVD) methods. While most efforts have been devoted to decipher the growth mechanism and controllable synthesis of these planar defects, their effects on transport properties have also attracted some attention. Metal nanoparticle-seeded growth of semiconductor nanowires enables control of the aspect ratio, diameter, and crystalline structure through variations of growth parameters. Barth et al. showed that the defects of Ag seeds could be transferred to the produced Ge nanowires, in the form of radial twins (Barth et al. 2011). Zhe et al. demonstrated that in boron carbide nanowires, the stacking faults could grow in both axial direction and transverse directions (Guan et al. 2012). Stacking faults are found to significantly affect the mechanical properties of nanowires (Afanasyev & Sansoz 2007, Jang et al. 2012). As one example, in GaAs nanowires, stacking faults are found to increase the Young's moduli of defective wurtzite nanowires by 13% in comparison to those defect-free ones (Chen et al. 2016). The authors attributed the stiffening effects of stacking faults to altered interatomic bonding at the stacking faults. The nanowires were grown via a MOVPE method, with the ones with stacking faults and the ones without faults on the same piece of substrate. **Figure 1.8** shows the low-magnification and high resolution TEM images of both kinds of nanowires.

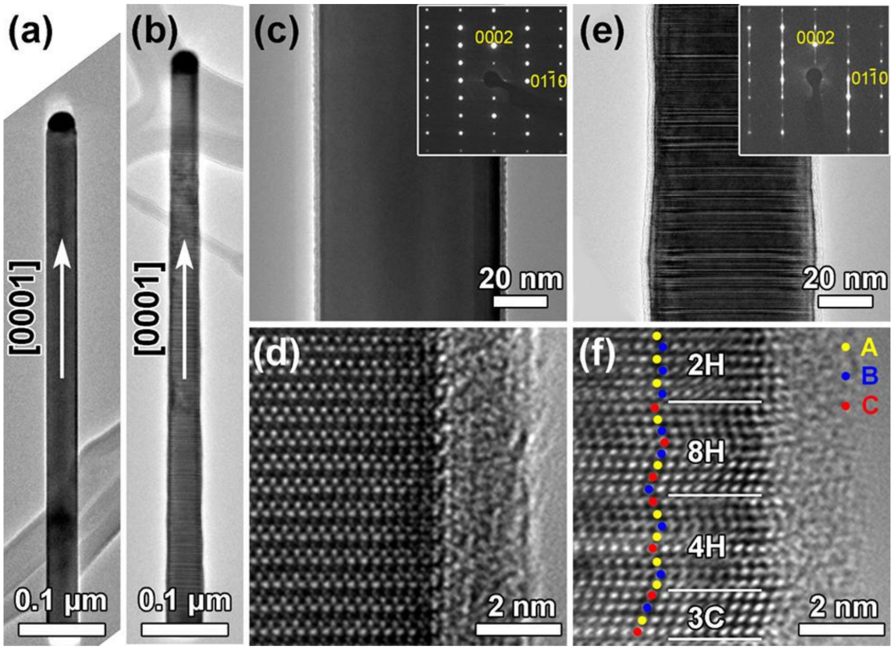

Figure 1.8 Low-magnification TEM images of GaAs nanowires of (a) hexagonal WZ and (b) WZ-SF (SF for stacking faults). Diffraction contrast (c) and HRTEM (d) images of WZ GaAs nanowires. Diffraction contrast (e) and HRTEM (f) images of WZ-SF GaAs nanowires. The insets in (c) and (e) are their corresponding SAED patterns (Chen et al. 2016).

Other than inorganic nanowires, microstructures hold equivalent importance in determining the thermal conductivity of polymer nanofibers, i.e., the chain alignment, crystallinity, and backbone structures. As demonstrated by Zhang et al. through MD simulation, the thermal transport carried through the strong covalent bonds is responsible for majority of the effective thermal conductivity, rather than the contributions from the weak vdW interactions (Zhang & Luo 2016). In another MD study by Zhang et al., they demonstrated that in PE nanofibers, there exists a chain morphology dependence for the thermal conductivity, which showed as a dramatic reduction by about 90% when temperature increases up to ~400 K (Zhang & Luo 2012). In their simulation, they built a simulation volume consisting of multiple well-aligned PE chains and monitored the volume and chain morphology changes when the simulation domain was heated from 300 K to 800 K at atmospheric pressure. They found that the well-aligned crystalline PE chains maintained the well-ordered structure up to 400 K, and the volume showed a significant jump around 400 K, disrupting the intra-chain order, although the inter-chain structure order is maintained. When temperature increases beyond 600 K, another volume jump occurred, and the crystal is melted and the chains are tangled altogether in an amorphous phase. Meanwhile, thermal expansion with increasing temperature leads to voids and, together with the entangle chains that serve as efficient phonon scattering sites, reduced thermal conductivity. Later, they published another work, taking advantage of the phase-dependent thermal conductivity of PE, discussed a thermal diode that showed a scaled rectification ratio ranges from 12 to 25 (Zhang & Luo 2015). The practice of improving the molecular chain alignment and/or crystallite orientation is also desirable for charge transport in polymers, which can be helpful for polymeric material based semiconductors. Many polymer materials tend to be partially crystalline, some of their polymer chains stack in well-organized crystallites. However, in bulk form, the crystallite orientation could still be in a random manner, which results in inefficient charge/phonon transport. Kline et al. attempted deposition of the polythiophene on a hydrophobic surface and used X-ray diffraction to find that the fraction of mis-oriented crystallites depends on surface hydrophobicity (Joseph Kline et al. 2006). Polythiophene films spin-casted on self-assembled monolayer (SAM) coated surface have much better alignment of the crystallites than the bulk counterparts.

Apart from the transport properties, purposely aligned crystallites/molecular chains and improved crystallinity could enhance the Young’s modulus of polymers along the chain direction as well. Li et al. managed to fabricate crystalline PE nanofibers following an approach combining a traditional gel-based spinning method with a tip-drawing technique (Li et al. 2014). The microstructure change at each drawing stage is illustrated in **Figure 1.9**.

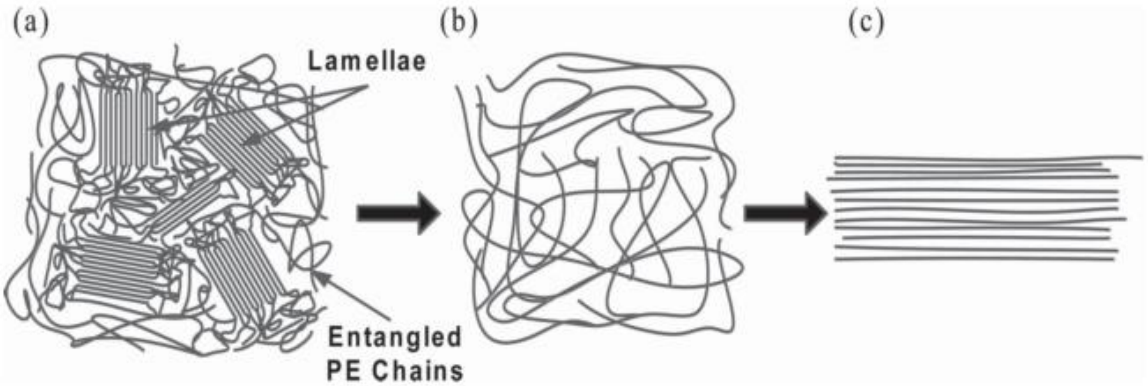

Figure 1.9 Microstructure change during the fiber drawing process. (a) Semi-crystalline PE gel with crystalline and amorphous regions. (b) PE molecular chains dissolved in Decalin solvent. The PE chains are randomly entangled in the solution. (c) Crystalline PE nanofiber with aligned chains (Li et al. 2014).

In bulk form, the long PE molecular chains are folded locally in the form of crystallites, usually called “lamellae”. The lamellas are surrounded by other amorphous phase PE molecular chains, which hinder efficient transport of charges/phonons and result in a low elastic modulus. When dissolved in solvent, the local crystallites and amorphous phase PE molecules are loosely entangled. When drawn by a glass tip, the loosely entangled molecules will align in the direction of drawing and crystallize, resulting in highly aligned and crystalline PE nanofibers. The approach greatly suppresses the formation of amorphous domains and voids that degrade the material properties. This approach was able to produce nanofibers having a high Young’s Modulus around 312 GPa, approaching the theoretical limits as predicted for single PE chain (Jiang et al. 2012a, Li et al. 2014). Selective area electron diffraction pattern (SAED) of different diameter as-fabricated nanofibers indicated a trend of higher crystallinity for smaller diameter PE nanofibers. The SAED pattern of an 80.9 nm PE nanofiber indicates a remarkable single crystalline nature. These results illustrate a venue of engineering the microstructure to modulate both the transport and mechanical properties of polymer fibers.

1.3 Summary

All the work discussed here showed that to fully understand the transport mechanisms in various kinds of nanowires, either semiconducting or polymeric, requires thorough knowledge of the structural information, that is, crystalline structure, diameter, composition, morphology, etc. It is demonstrated that structure is of paramount importance for nanowire transport properties. The emergence of nanowires with complex structures demands systematic studies with thorough structural characterization and thermal transport property measurement, which could lead to better understanding on how these novel structures affect phonon transport.

In the following chapters, we employed a well-established suspended micro-bridge method to experimentally study thermal transport properties of different polymeric nanowires, boron carbide nanowires, and quasi-one-dimensional (quasi-1D) $Ta_2Pd_3Se_8$ nanowires, which are all of complex structures. The dissertation is organized as follows.

In chapter 2, we discuss the implementation of the micro-bridge sensing method with enhanced measurement sensitivity and show the effects of several different factors on the measurement results. The sample preparation, measurement approach, and uncertainty analysis will also be covered.

In chapter 3, we describe thermal conductivity measurement and structural characterization with micro-Raman spectroscopy of individual electrospun PE nanofibers fabricated at various conditions.

In chapter 4, we present studies of individual boron carbide nanowires of different diameters, compositions, stacking fault density and orientations. Details of structural characterization using TEM and the impacts of microstructures on thermal transport are carefully investigated. For the first time, we show experimentally the significant effects of kinks on thermal conductivity of boron carbide nanowires. The effects of defects in the kinked region on thermal transport across the kink were also explored.

In chapter 5, we discuss the thermal transport properties of the novel quasi-1D vdW $Ta_2Pd_3Se_8$ nanowires prepared through wet exfoliation. The irregular cross sections of these nanowires are carefully examined and the dependence of thermal conductivity on cross-sectional size and length were studied.

Chapter 6 provides a summary of the key conclusions from this dissertation.

2. Experimental Setup

Various techniques have been developed to measure the thermal transport properties of nanoscale materials, such as thin films and nanowires. For example, 3 omega method (3ω) and time-domain thermoreflectance (TDTR) method are widely applied to measure the cross-plane thermal conductivity and interfacial thermal resistance of thin films (Cahill 1990, 2004; Weathers & Shi 2013). However, these techniques could be not readily applied for the thermal property measurement of nanowires. To cope with the challenge, a thermal bridge method based on a suspended microdevice for measuring thermal conductivity and thermoelectric properties of nanowires was developed, which can measure the thermal conductance of individual nanowires as low as ~1 nW/K (Li et al. 2003b, Shi et al. 2003). This experimental scheme has been successfully applied to study the thermal transport property of individual carbon nanotubes (Kim et al. 2001, Yu et al. 2005), various kinds of nanowires (Chen et al. 2008, Li et al. 2003b), nanoribbons (Yang et al. 2012), and more recently, contacts and interfaces between individual nanostructures (Yang et al. 2010, 2014). In addition, Chang et al. (Chang et al. 2007) further extended the capability to study phonon transport in nanowires under strain/buckling. These studies greatly advanced our understanding of the behavior of phonons, the energy carriers, in the highly confined nanostructures.

The sensitivity of the four point I-V measurement setup is limited to a noise equivalent thermal conductance of about 0.5 nW/K at room temperature. Two major noise sources are the radiation dominated background conductance and a rather long period (~20 minutes) temperature drift of the sample holder in the cryostat. To push for a lower thermal conductance detection limit, a new measurement scheme first demonstrated by Wingert et al. has been implemented in this dissertation, which achieved a detectable thermal conductance as low as ~10 pW/K (Wingert et al. 2012). To eliminate the major noise source from the temperature fluctuation of the sample holder, Wingert et al. (Wingert et al. 2012) introduced a Wheatstone bridge setup with a reference device also placed on the sample holder in the cryostat, which experience the same temperature fluctuation with the measurement device. Through common mode rejection, the effects of sample holder temperature fluctuation can be effectively canceled out. Herein, we successfully incorporate the technique into our measurement setup and this chapter is dedicated to the demonstration and discussion of the experimental approach.

2.1 Measurement Devices

Figure 2.1 shows an SEM micrograph of the microdevice for nanowire thermal and thermoelectric property measurements, which consists of two side-by-side 18.2 μm × 27.1 μm low stress silicon nitride (SiNx) membranes suspended by six 0.5 μm thick, 415.9 μm long and 2.2 μm wide SiNx beams. Each SiNx membrane has one platinum resistance thermometer (PRT) composed of 30 nm thick and 500 nm wide platinum (Pt) line patterned on top, which can also be used as a microheater through joule heating. The serpentine Pt line is covered by 200 nm thick low temperature silicon oxide (LTO) layer, to avoid the potential of shorting the Pt coils when measuring electrically conductive samples. The PRT is connected to 400 μm × 500 μm Pt contact pads situated on the substrate through 1.2 μm wide Pt leads on the long SiNx beams. One or two additional Pt electrodes can be fabricated on the edge of each SiNx membrane, facilitating simultaneous characterization of electrical conductivities and Seebeck coefficients, to probe the thermoelectric property of tested nanostructures. Additionally, the substrate could be etched through to allow TEM examination of the microstructure of measured samples.

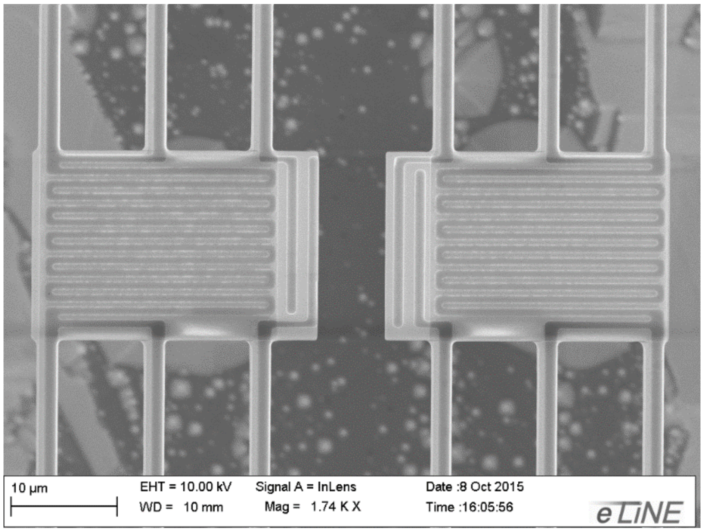

Figure 2.1 An SEM micrograph of the suspended microdevice with electrodes and integrated microheaters/thermometers made from serpentine Pt lines.

2.2 Sample Preparation

For measurements of nanowire thermophysical properties with the device described above, a crucial step is to place an individual nanowire sample between the two suspended membranes. It is made possible by using an in-house assembled micromanipulator, as shown in **Figure 2.2**, to maneuver the samples and sit them at desirable locations and in proper orientations.

The sample placement process usually includes two steps. First, a small amount of samples, such as carbon nanotubes or different kinds of nanowires, are dispersed in solutions such as reagent alcohol or isopropanol alcohol (IPA) to form a suspension, using ultrasonic sonication. A few drops of the suspension are then casted onto a piece of polydimethylsiloxane (PDMS). We choose PDMS as the substrate because the soft material lowers the risk of damaging the very sharp tip used to pick up the nanowire sample. After the solvent evaporated, many individual nanowires can be found on the PDMS surface. In addition to drop-casting, stamping can also be used to transfer nanowires or nanotubes from the substrate on which they are grown or fabricated to the elastomeric PDMS piece.

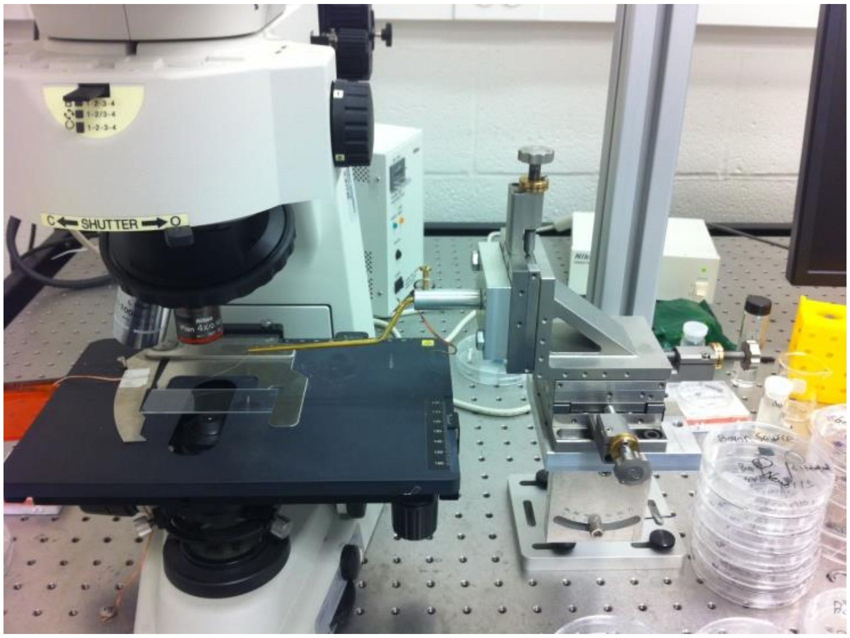

Figure 2.2 A photograph showing the custom-built micromanipulator integrated with a Nikon microscope (Nikon ECLIPSE 50i) used to manipulate the individual nanowires.

After the samples are transferred onto the PDMS substrate, we can use a sharp probe (The Micromanipulator Co. model 7X) with a tip radius of ~0.1 μm mounted on the mechanical translation stage to pick up a single nanowire lying on the PDMS and place it between the two suspended membranes. The whole process is performed under a 100×, long working distance (6.5 mm) objective lens mounted on a Nikon optical microscope. **Figure 2.3** shows a silicon nanoribbon situated between the two suspended membranes. Cross-contact nanowire samples can also be prepared in a similar manner by carefully orienting individual nanowires in a desired manner to probe point contact thermal resistance between various nanostructures.

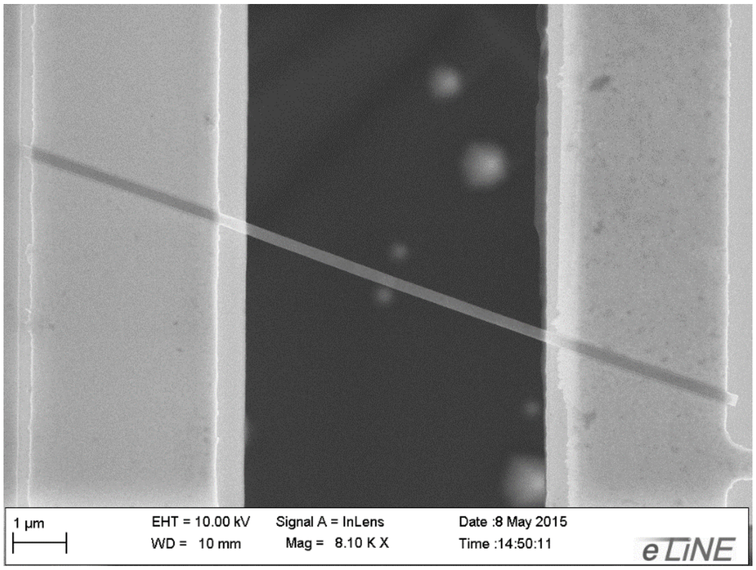

Figure 2.3 An SEM micrograph of an individual silicon nanoribbon bridging the two side-by-side suspended membranes.

To improve the thermal and/or electrical contacts between the sample and the membranes, electron beam induced deposition (EBID) can be used to locally deposit Au/Pt pads to increase the contact area between the nanowire sample and the suspended membranes (Chen et al. 2008), as shown in **Figure 2.4**.

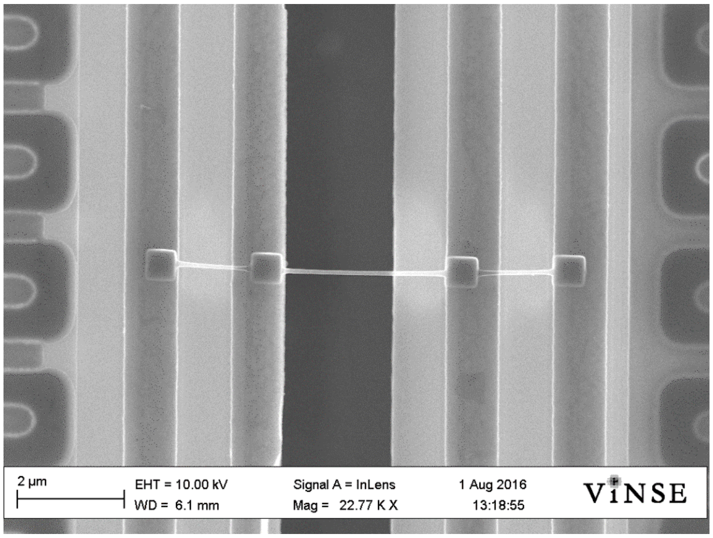

Figure 2.4 An SEM micrograph of a boron carbide nanowire bridging the four electrodes on the microdevice with local deposition of Pt at the contact using EBID.

2.3 Measurement Setup

Figure 2.5 shows a schematic drawing of the measurement setup. The suspended microdevice with a nanowire is placed in a cryostat (Janis CCS-450) with a vacuum level below 10^{-6} Torr, achieved with a turbomolecular pump (Edwards E2M1.5). Two lock-in amplifiers (Stanford Research SR850) are used to monitor the voltage change of the PRTs on the heating and sensing membranes, respectively.

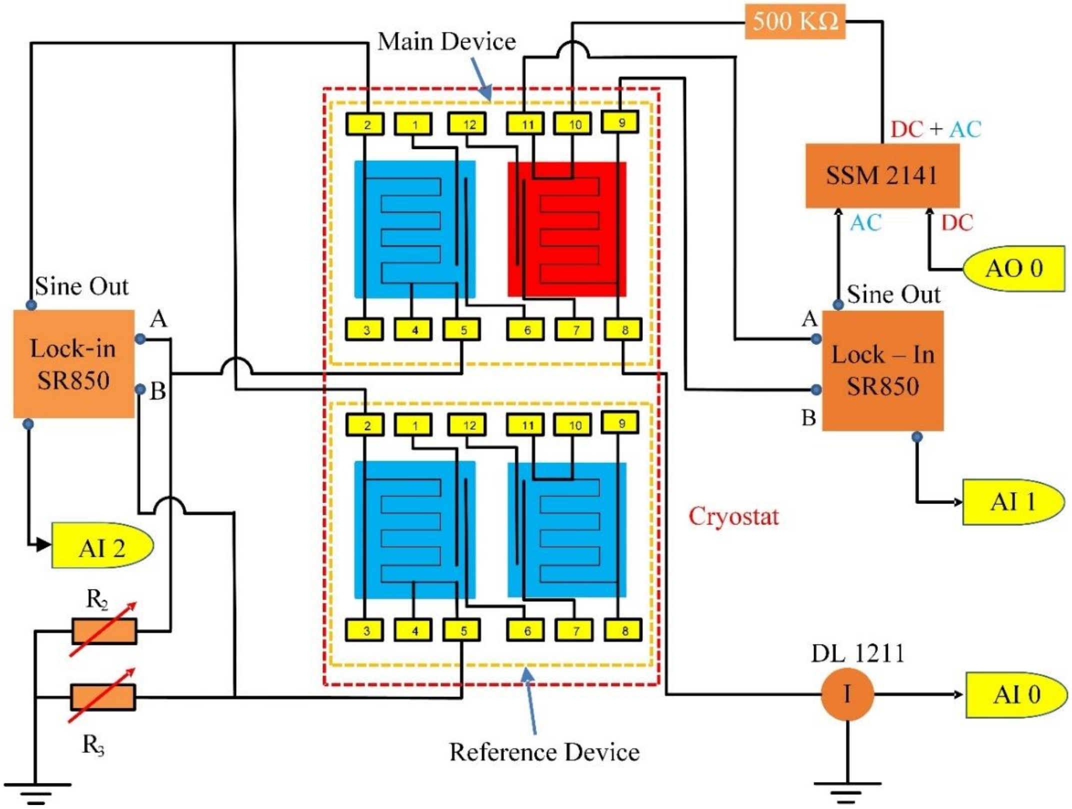

Figure 2.5 Schematic diagram of the common mode measurement setup.

A small sinusoidal alternating current (AC) signal from the lock-in amplifier on the heating side is coupled with a direct current (DC) heating current source through an integrated differential amplifier (Analog Devices SSM2141). One resistor of large resistance (505 kΩ) is connected into the heating side circuit to achieve a constant current condition under each designated DC heating voltage. The sensing side circuit is connected by coupling a reference device, situated right aside of the measurement device (<5 mm), both of which are connected with a precision resistor (Extech 380400) sitting in ambient condition to form a Wheatstone bridge.

During the measurement, a sweeping DC current is applied to the Pt coil on one membrane to generate Joule heating and the temperature of both membranes will change accordingly. The temperature changes induce resistance changes to both the heating and sensing side, which lead to changes to the AC output voltages that are measured by the lock-in amplifiers and fed into a data acquisition (DAQ) board (National Instruments PCI-6052e). The DC heating current is measured by a high accuracy current preamplifier (DL Instruments Model 1211).

Figure 2.6 shows the thermal circuit of the measurement setup. The two suspended membranes on the left denote the heating membrane and the sensing membrane, respectively. A DC current (I) passes through the PRT on the heating membrane and produces a certain amount of Joule heat, $Q_h = I^2R_h$, where R_h is the PRT's electrical resistance. The PRT on each membrane is connected to the contact pads by four Pt leads, allowing for four-probe resistance measurement. The resistance of each Pt lead is R_L, which is about the same as R_h. Therefore, there is also Joule heating dissipated in the two Pt leads that carries the DC current to the heating PRT, which can be written as $2Q_L = 2I^2R_L$.

Assuming that the temperature of the heating membrane is raised to a uniform temperature T_h, which can be justified by the fact that the internal thermal resistance of the membrane is much smaller than the thermal resistance of the long narrow beams that thermally connects the membranes to the silicon substrate at temperature T_0. A certain amount of heat Q_2 is conducted through the sample from the heating membrane to the sensing one, raising its temperature to T_s. In high vacuum and with a small ΔT_h ($\Delta T_h = T_h - T_0 < 5$ K), the background heat transfer between the two membranes by residual air conduction/convection and direct thermal radiation could be negligible compared to Q_2, as discussed below. The heat conducted through the sample, Q_2, is further transferred to the substrate through the six beams supporting the sensing membrane. The rest of the heat, i.e. $Q_1 = Q_h + 2Q_L - Q_2$, is conducted to the environment through the other six beams connected to the heating membrane.

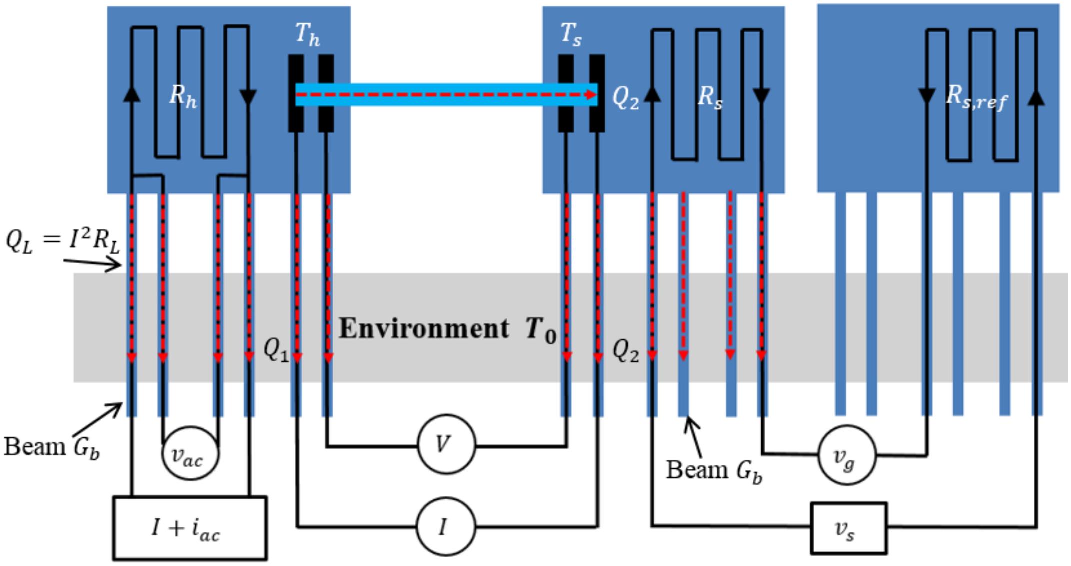

Figure 2.6 The thermal circuit of the common mode measurement setup.

The six supporting beams of each membrane are designed to be identical and fabricated under the same condition. Assuming that the radiation heat loss and residual air molecules conduction/convection are negligible compared to the conduction heat transfer through the beams, the total thermal conductance of the six suspending beams can be written as $G_b = R_b^{-1} = 6k_l A/L$, where k_l, A, and L are the thermal conductivity, cross sectional area, and length of each beam, respectively. Following the thermal circuit in **Figure 2.6**,

$$Q_2 = G_b(T_s - T_0) = G_s(T_h - T_s), \tag{2.1}$$

where G_s is the thermal conductance of the nanowire bridging the two membranes. The inverse of G_s, that is, R_s, includes both the intrinsic thermal resistance of the nanowire sample and the contact thermal resistance between the sample and the membranes, which is

$$R_s = R_i + R_c . \tag{2.2}$$

Here $R_i = L_n/A_nk_n$ is the intrinsic thermal resistance of the measured nanowire, where k_n, A_n and L_n are the thermal conductivity, cross sectional area, and length of the nanowire segment suspended between the two membranes, respectively. R_c is the contact thermal resistance between the sample and the two membranes. Because the temperature rise ΔT_h is carefully controlled to be small (~5 K), G_s, G_b, and G_c can be taken as constants as ΔT_h is ramped up.

Based on the thermal resistance circuit, G_b and G_s can be further expressed as a function of ΔT_h, ΔT_s ($\Delta T_s = T_s - T_0$), Q_h and Q_L, as

$$G_b = \frac{Q_h + Q_L}{\Delta T_h + \Delta T_s} , \tag{2.3}$$

and

$$G_s = G_b \frac{\Delta T_s}{\Delta T_h - \Delta T_s} . \tag{2.4}$$

Q_h and Q_L can be readily calculated from the current and the voltage drops across the heating PRT and the Pt leads. ΔT_h and ΔT_s are derived from the measured resistance change of the two PRTs and their temperature coefficients of resistance (TCR = $(\mathrm{d}R/\mathrm{d}T)/R$).

Figure 2.7 shows the simplified electrical circuits for both the heating and sensing sides. The four-probe electrical resistance R_h of the heating PRT is measured using an SR850 lock-in amplifier with a ~300 nA 1400 Hz sinusoidal excitation current. The resistance change of the sensing side resistor is calculated based on the Wheatstone bridge voltage output Δv_g .

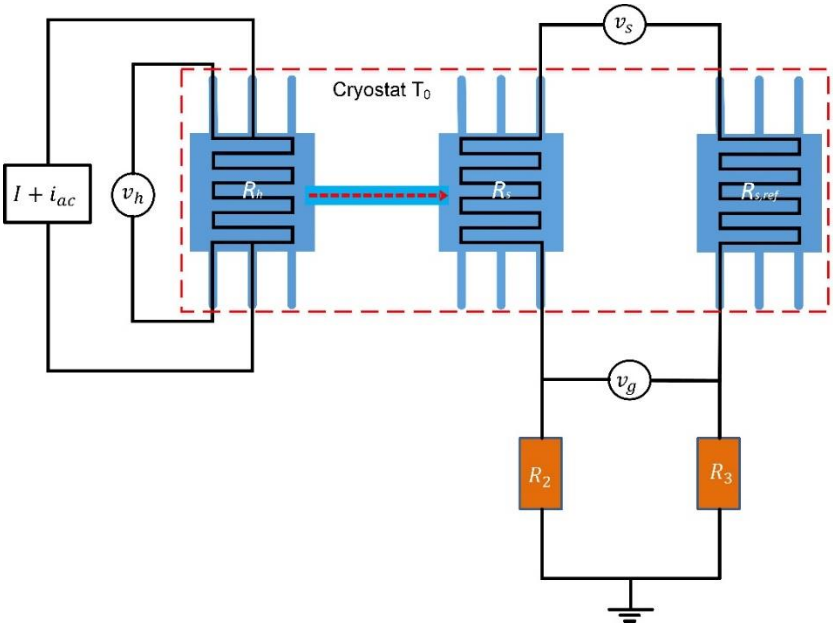

Figure 2.7 The simplied electrical measurement circuit (the Wheatstone bridge circuit).

The temperature rise of the heating membrane (ΔT_h) depends on the DC current I applied to the heating PRT and is related to R_h per the following equation

$$\Delta T_h(I) = \frac{\Delta R_h(I)}{\frac{dR_h}{dT}}, \tag{2.5}$$

where $\Delta R_h(I) = R_h(I) - R_h(0)$.

A 300-500 nA sinusoidal current, i_{ac}, with a frequency f is coupled to the much larger DC heating current I. An SR850 lock-in amplifier is used to measure the first harmonic component (v_{ac}) of the voltage drop across the heating PRT, yielding $R_h = v_h/i_{ac}$. For R_h obtained by this method, it has been shown that

$$\Delta T_h(I) = \frac{\Delta R_h(I)}{3\frac{dR_h}{dT}}, \text{ for } f \ll \frac{1}{2\pi\tau}, \tag{2.6a}$$

and

$$\Delta T_h(I) = \frac{\Delta R_h(I)}{\frac{dR_h}{dT}}, \text{ for } f >> \frac{1}{2\pi\tau} . \tag{2.6b}$$

Here τ is the thermal time constant of the suspended device and is estimated to be on the order of 10 ms. The difference between these two solutions for different frequency ranges arises from a first harmonic modulated heating component, i.e., $2i_{\text{ac}}IR_h$. At a very low (high) frequency compared to $1/(2\pi\tau)$, the modulated heating yields a nontrivial (trivial) first harmonic component in T_h. This further causes a nontrivial (trivial) first harmonic oscillation in R_h. The effect gives rise to a factor of 3 difference in ΔR_h measured by the lock-in method. In addition, τ is proportional to C/K, where C and K are the heat capacity and thermal conductance, respectively. According to the kinetic theory, K is proportional to Cl, where l is the phonon mean free path and increases with decreasing temperature. Hence, τ is proportional to $1/l$ and decreases as temperature drops. Therefore, the transition between the two solutions in Eq. (2.6) occurs at an increased frequency as the temperature decreases. In practice, we use f = 1400 Hz, for which Eq. (2.6b) is valid in the temperature range of 20 - 420 K.

The temperature rise of the sensing membrane, ΔT_s, is obtained from the Wheatstone bridge output voltage change. The bridge circuit is composed of sensing side resistor R_s of the measurement device, a reference device resistor $R_{s,ref}$, and two additional precision resistors, R_2 and R_3, connected in parallel, as shown in **Figure 2.7**. The measured bridge output voltage v_g based on the four resistances and the source voltage v_s supplied by the lock-in amplifier is then,

$$v_g = \left(\frac{R_2}{R_s + R_2} - \frac{R_3}{R_{s,ref} + R_3}\right)v_s . \tag{2.7}$$

Equation (2.7) could be rearranged to express R_s in terms of other components,

$$R_s = \frac{R_2}{\left(\frac{R_3}{R_{s,ref} + R_3} + \frac{v_g}{v_s} \right)} - R_2 . \tag{2.8}$$

The bridge output voltage change Δv_g could be readily calculated to reflect the true resistance change of the sensing side, ΔR_s, as a result of heat transferred to the sensing side. Different from the heating side measurement circuit, which directly reflects the PRT resistance change, the sensing side measurement yields the total resistance change including the resistance of the PRT, R_m, and the resistance of the two current-carrying beams, $2R_b$. As a result of the heat conduction through the nanowire sample, the temperature of the sensing membrane is raised to a uniform temperature, T_s. However, the temperature of the long suspended beams varies linearly from the membrane temperature, T_s, to the ambient temperature of the controlled cryostat substrate temperature, T_0. As such, the total sensing side resistance can be expressed as,

$$R_s + \Delta R_s = 2\left[R_b + \frac{dR_b}{dT}\left(\frac{T_s - T_0}{2} \right) \right] + R_m + \frac{dR_m}{dT}(T_s - T_0) . \tag{2.9}$$

Straightforward simplification of the above expression leads to,

$$\Delta R_s = \left(\frac{dR_b}{dT} + \frac{dR_m}{dT} \right)(T_s - T_0) . \tag{2.10}$$

The resistance change is equivalent to a uniform temperature rise over the membrane and one single beam. Thus, an effective dR_s/dT could be calculated as,

$$\frac{dR_{s,eff}}{dT} = \left(\frac{R_b + R_m}{2R_b + R_m} \right) \frac{dR_s}{dT} . \tag{2.11}$$

Therefore, the temperature rise of the sensing side could be extracted using,

$$\Delta T_s = \frac{\Delta R_s}{\frac{dR_{s,eff}}{dT}} \tag{2.12}$$

To measure additional electrical properties (Seebeck coefficients and electrical conductivities) of nanowires, the sample can be placed across the four Pt electrodes on the SiNx membrane, as shown in **Figure 2.8**. The contacts between the sample and Pt electrodes can be treated with EBID to minimize the electrical and thermal contact resistance, as discussed earlier. For nanowires with thin native oxide sheath, prior to EBID, electrical contact is made possible by using electron beam induced etching (EBIE) to etch away the oxide layer. Alternatively, focused ion beam (FIB) could be used to locally etch away the amorphous sheath that cannot be taken away by EBIE. The four inner electrodes on the suspended membranes enable four-probe electrical resistance measurement of the nanowire sample, which is essential for accurate determination of the intrinsic electrical resistance (Long et al. 2010). For measurement of large resistance sample (>1 MΩ), the measured voltage signal is passed through an instrumentation amplifier (Texas Instruments INA110) having an extremely large input impedance (>1 GΩ) before being fed into an voltage amplifier (SR560) to avoid inaccurate measurements (Werheit et al. 2009). The input impedance of the SR560 is around 100 MΩ, inadequate for high resistance measurement, such as the boron carbide nanowires in this dissertation.

To achieve accurate Seebeck coefficients measurement, the Seebeck voltage is extracted from the two inner electrodes contacting the nanowires as a function of temperature gradient, i.e., $V_{TE}=(S_s-S_{Pt})(T_h-T_s)$ (Mavrokefalos et al. 2007, Werheit et al. 2009). It is also confirmed that the Seebeck voltage signal vanishes when tested under atmospheric pressure when no temperature difference existed. In actual experiment, the circuit is cut off (the relay closed) for Seebeck voltage measurements to avoid unwanted heating of the devices owning to the small current travelling through. The circuit is connected (the relay opened) for electrical resistance measurement of the nanowire. A series of I-V results were measured to extract the resistance of the suspended portion of the nanowire.

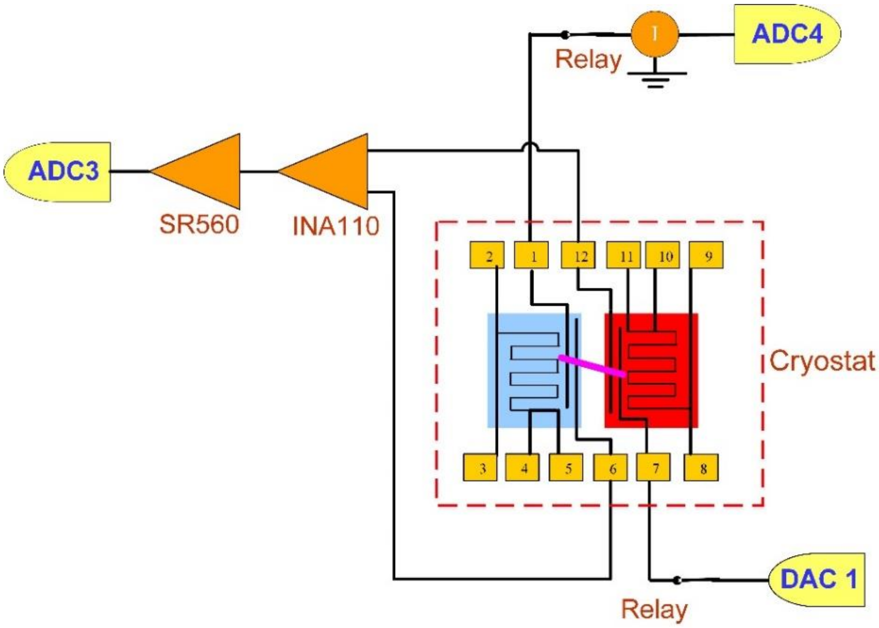

Figure 2.8 Illustration of the additional Seebeck and four-probe electrical resistance measurement setup when the circuit is connected (Relay opened).

2.4 Characterization of the Wheatstone Bridge Measurement Scheme

The traditional 4-point *I-V* measurement approach has a measurement sensitivity of ~0.5 nW/K, which is mainly limited by two factors: i) rather long period temperature drifts of the proportional-integral-derivative (PID) controlled temperature stage (~100 mK), ii) the amplifier noise due to the large dynamic reserve required to measure small voltage changes on top of a large output voltage (Wingert et al. 2012). The implementation of Wheatstone bridge measurement scheme ideally resolves these two issues, pushing the lower thermal conductance measurement limit down to ~10 pW/K, which represents two orders of magnitudes enhancement over the 4-point method.

Figure 2.9 shows the temperature fluctuations of the sample stage as captured by both the bridge and four-point measurement method concurrently for two hours with the temperature controller set at 300 K. Note that the fluctuation noise here also carries the uncertainty from DC voltage, SSM2141 coupling, and inherent noise of the lock-in amplifiers. The adopted bridge sensing parameters are v_s = 10 mV and a sensitivity of 20 μV for the lock-in amplifier. The temperature fluctuation measured by the bridge scheme is below 10 mK, while the 4-point approach yields a drift/fluctuation spanning ~80 mK. The signal from the 4-point method suffers from a periodic temperature drift on the device side, which is typical for PID temperature control. Such fluctuation is absent in the signal from the bridge scheme based on common mode rejection, which leads to a dramatic enhancement of the measurement sensitivity.

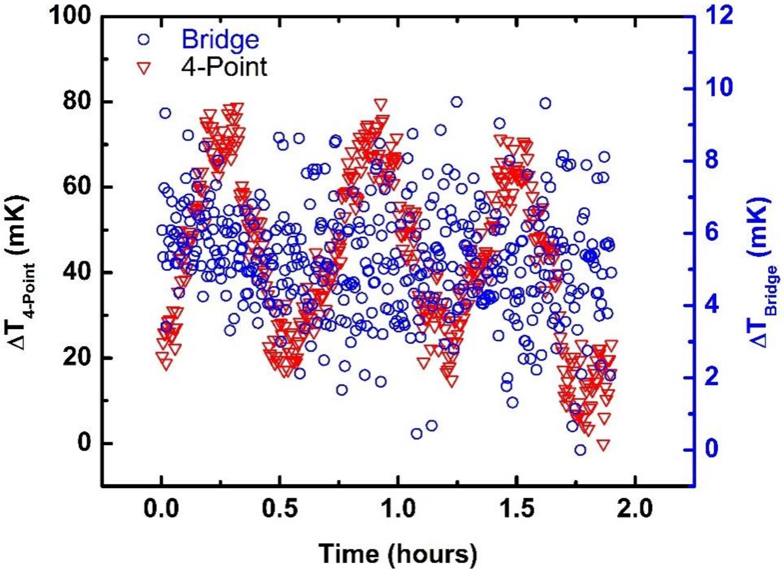

Figure 2.9 The temperature fluctuation in the vacuum chamber concurrently monitored by the bridge and 4-point measurement methods in 2 hours.

While Wingert et al. demonstrated a temperature sensitivity of 0.6 mK, it is achieved with a large bridge driving voltage, v_s = 100 mV and a sensitivity of 5 μV (Wingert et al. 2012). Raising the driving voltage v_s of the bridge method could lead to unwanted ac heating and unbalanced base temperature rise of the heating and sensing membranes, a matter that will be discussed later. The parameters adopted here are chosen based on our practice that allows for sensitive measurement in a large temperature range and reasonable data acquisition time.

Taking a noise equivalent temperature (NET_s) equal to 10 mK, a noise equivalent conductance (NEG_s) can be calculated. To calculate this resolution, we use the thermal conductance of beams measured experimentally at 300 K (75 nW/K), and assume a temperature difference between the heating and sensing membranes to be 5 K,

$$NEG_s = G_b \frac{NET}{\Delta T_h - \Delta T_s} \approx 76 \;\; nW/K \times \frac{10 \;\, mK}{5 \;\, K} = 0.152 \; nW/K \;. \tag{2.13}$$

The calculated sensitivity is approximately one order of magnitude enhancement compared to the traditional 4-point *I-V* measurement. Since the noise almost remains the same when adjusting the bridge driving voltage, v_s, the NEG_s scales inversely with the applied v_s. Hence, the sensitivity could be further enhanced to 15.2 pW/K if using a 100 mV driving voltage. Even better sensitivity could be obtained by using longer time constant (>1 *s*) and increasing temperature difference (~10 K).

2.5 Effect of AC current and Radiation Shield

2.5.1 Driving voltage of the sensing side Wheatstone bridge circuit

In 4-point *I-V* measurement, the AC current of the heating and sensing sides are deliberately controlled to be approximately the same (~0.3 μA), such that the temperature rises arising from AC heating are small (on the order of ~1 mK) and also carefully balanced considering the identical conditions of both sides. However, the AC heating effects on both membranes are not as well balanced in Wheatstone bridge measurement scheme. In addition, the AC current is changing due to the resistance change as temperature shifts. On the other hand, application of larger driving voltage on the sensing side offers better measurement sensitivity. For example, Liu et al. applied a large AC current (<= 10 μA) for the 4-point *I-V* resistance measurement to raise the signal-to-noise ratio (SNR), which causes temperature rises of both membranes by ~8 K (Liu et al. 2014). This section is dedicated to a discussion of the unbalanced temperature rise induced by AC heating, and whether such unbalanced heating incurred by the sensing current would bring significant errors to the measurement.

Figure 2.10 shows the thermal circuit of the measurement setup, including the components of both AC and DC induced heating. Similar to the analysis of the heat transfer diagram from DC heating effect, application of the AC sensing voltage/current also gives rise to Joule heating at both heating and sensing side membranes and beams. The difference is that previous analysis only considers the DC heating while neglecting the AC heating from the small AC current, here both heating effects are rigorously discussed. For the heating side, a DC current (I) coupled with an AC current ($i_{\mathrm{ac,h}}$) conveyed through the heating membrane, as a result, two Joule heating effects, $Q_H = I^2R_h$ and $Q_h = i^2_{ac,h}R_h$, are generated on the PRT membrane. The membrane is connected to the substrate by six long suspended beams. The resistance of each beam is R_L; and therefore, Joule heating in the beam as a result of both currents, $Q_L = I^2R_h$ and $Q_{lh} = i^2_{ac,h}R_h$ are also generated. On the sensing side, similarly, an AC current ($i_{ac,s}$) passes through the suspended membranes, which gives rise to Joule heating $Q_s = i^2_{ac,s}R_s$ and $Q_{ls} = i^2_{ac,s}R_s$ on the sensing side PRT membrane and current-carrying beams, respectively.

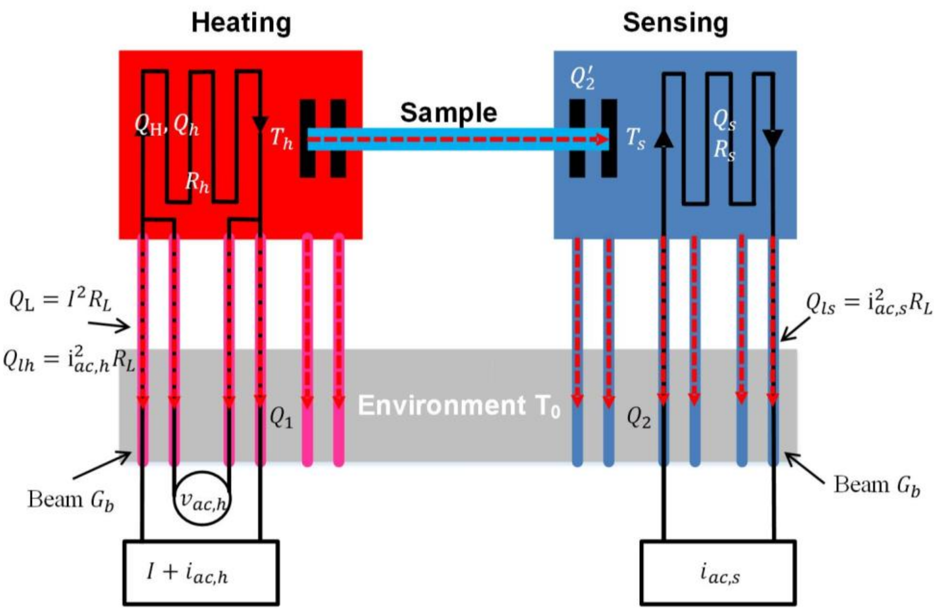

Figure 2.10 Heat transfer diagram of the suspended micro-heater device when considering alternating current (AC) Joule heating.

Since the internal thermal resistance of heating membrane is much smaller than the long supporting beams, the temperature of the membrane is assumed to be uniform and denoted as T_h. A certain amount of heat, Q_2', is conducted to the sensing side through the suspended nanowire sample. Ignoring the radiation heat transfer, a certain amount of heat Q_2 is conducted to the substrate through the six supporting beams. Heating side beams also lose an amount of heat, Q_1, to the substrate. Based on energy conservation, we could have the following equations:

$$Q_H + 2Q_L + Q_h + 2Q_{hl} + Q_s + 2Q_{ls} = Q_1 + Q_2 \tag{2.14}$$

$$Q_2' = G_s(\Delta T_h - \Delta T_s) \tag{2.15}$$

$$Q_2' + Q_s + 2Q_{ls} = Q_2 \tag{2.16}$$

$$Q_2 = Q_{ls} + G_b \Delta T_s \tag{2.17}$$

$$Q_1 = Q_L + Q_{hl} + G_b \Delta T_h \tag{2.18}$$

The expressions ΔT_h and ΔT_s are then derived as,

$$\Delta T_h = \frac{G_b + G_s}{(G_b + 2G_s)G_b}(Q_H + Q_L) + \frac{G_b + G_s}{(G_b + 2G_s)G_b}(Q_h + Q_{lh}) + \frac{G_s}{(G_b + 2G_s)G_b}(Q_s + Q_{ls}) \tag{2.19}$$

$$\Delta T_s = \frac{G_s}{(G_b + 2G_s)G_b}(Q_H + Q_L) + \frac{G_s}{(G_b + 2G_s)G_b}(Q_h + Q_{lh}) + \frac{G_b + G_s}{(G_b + 2G_s)G_b}(Q_s + Q_{ls}) . \tag{2.20}$$

Equation (2.19) and (2.20) give the temperature rises of both membranes, which both consist of three components, i.e., temperature rise from DC Joule heating, heating side AC Joule heating, and sensing side AC Joule heating. The temperature rises superpose over each other. Ideally, the heating arising from the AC current in both heating and sensing sides shall be controlled within a negligible level. The temperature difference between the heating and sensing membranes, considering only the DC heating effect, can be written as,

$$\Delta T_h - \Delta T_s = \frac{Q_H + Q_L}{(G_b + 2G_s)} . \tag{2.21}$$

However, in reality, the temperature difference considering the AC heating effect is,

$$\Delta T_h - \Delta T_s = \frac{Q_H + Q_L}{(G_b + 2G_s)} + \frac{Q_h + Q_{lh}}{(G_b + 2G_s)} - \frac{Q_s + Q_{ls}}{(G_b + 2G_s)} . \tag{2.22}$$

The derived equations could help us to evaluate the effects of Joule heating from the exerted AC sensing current. The thermal conductance of most samples studied in this dissertation is much smaller than that of the beams, i.e., $G_b >> G_s$. Therefore, the dominant AC heating terms in Equations (2.19) and (2.20) can be written as,

$$\Delta T_h = \frac{Q_h + Q_{lh}}{G_b} , \tag{2.23}$$

$$\Delta T_s = \frac{Q_s + Q_{ls}}{G_b} . \tag{2.24}$$

In a typical 4-point *I-V* measurement, the AC currents in both heating and sensing side go through a resistor of large resistance, i.e., 500 KΩ and 1 MΩ, respectively, exerting a constant AC current (~0.3 μA) of almost the same magnitude. Thus, the temperature rise on both sides are carefully balanced and kept below the temperature fluctuation level of the sample holder.

The temperature rise of both membranes in a 4-point measurement, as plotted in **Figure 2.11**, increases with decreasing temperature, mainly due to the decreasing thermal conductance of the supporting beams at lower temperature. The temperature rise due to AC heating is lower than 100 mK across the whole temperature range, much less than the temperature difference (~5 K) typical for the measurement. The maximum temperature difference between the two membranes due to AC heating is below 10 mK, much lower than the sensitivity of typical 4-point measurement. Overall, the balanced temperature rise on both sides validates the assumption that the temperature difference is solely from the ramping DC heating.

In the Wheatstone bridge scheme, a larger AC driving voltage that is applied to the bridge can improve sensing voltage. Meanwhile, it will also exert a larger AC current on the sensing membrane, incurring more heating to the sensing membrane, and thus the temperature rises due to AC heating at both heating and sensing membranes are not balanced. **Figure 2.12** shows the calculated temperature that arises from different applied bridge driving voltage.

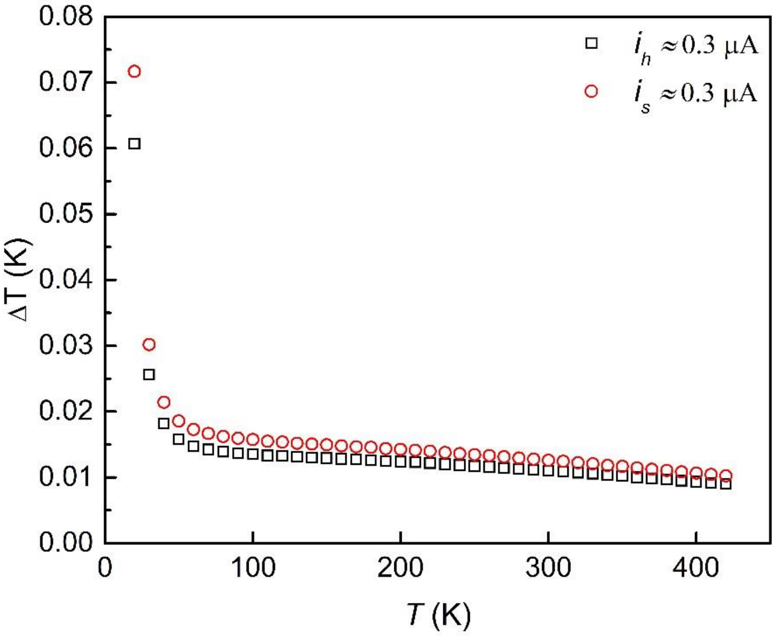

Figure 2.11 Temperature rise of both the heating and sensing membranes in 4-point scheme.

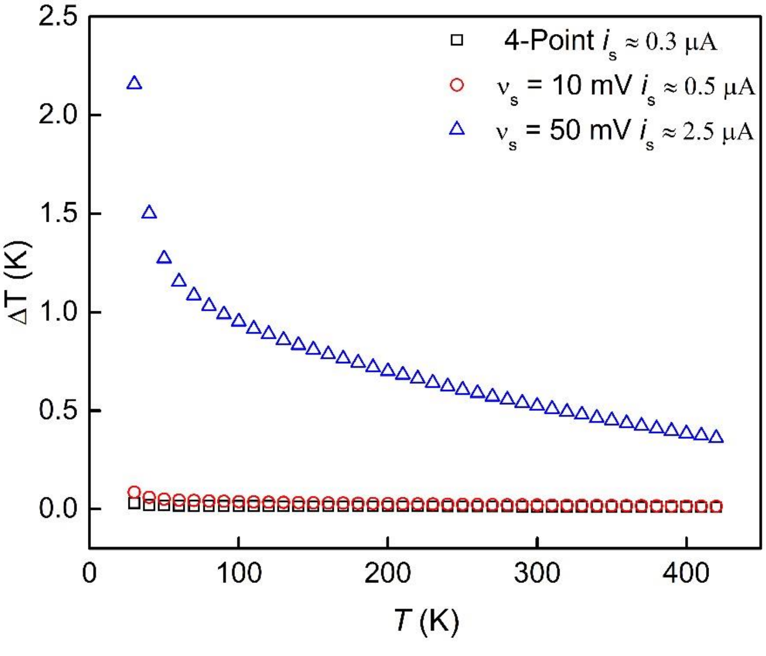

Figure 2.12 Temperature rise due to different applied AC bridge driving voltage in Wheatstone bridge scheme.

The unbalanced temperature rise would alter the overall heat that will be conducted through the suspended sample. However, to estimate whether the measurement would be affected, we need to consider whether the AC heating will lead to any sensible change of the resistance,

$$\left[\Delta T_h(I)\right]_{measured} = \left[\Delta T_h(I)\right]_{total} - \Delta T_{h,AC} \tag{2.25}$$

$$\left[\Delta T_s(I)\right]_{measured} = \left[\Delta T_s(I)\right]_{total} - \Delta T_{s,AC} \tag{2.26}$$

$[\Delta T_h(I)]_{measured} = (R_h(I)-R_h(0))/dR_h/dT$ and $[\Delta T_s(I)]_{measured} = (R_s(I)-R_s(0))/dR_{s,eff}/dT$ stand for the measured temperature rises from the heating side and the sensing side under a DC heating current I, respectively. $[\Delta T_h(I)]_{total}$ and $[\Delta T_s(I)]_{total}$ are the total temperature rise of the heating and sensing side from both the DC heating current I and the AC sensing currents, respectively. $\Delta T_{h,AC}$ and $\Delta T_{s,AC}$ represent the temperature rise of the heating and sensing side with no applied DC heating current, respectively, which come from the AC sensing currents. During the measurement, at one set temperature point, the AC sensing currents are held constant. As such, the temperature rise from the AC is ideally a constant, and $\Delta T_{h,AC}$ and $\Delta T_{s,AC}$ remain unchanged and the unbalanced temperature rises from the AC heating barely pose any effect on the measured temperature rises. In data processing, the G_s was acquired by linearly fitting the DC Joule heating to $[\Delta T_h(I)]_{measured}$ - $[\Delta T_s(I)]_{measured}$. As long as the base temperature rise caused by the AC heating is small (<5 K), and the crucial quantities, G_b and G_s, still stay within the linear regime, the temperature rise measured will only be marginally affected. As such, the measured temperature difference is still solely induced by DC heating, which remains identical to the scenarios assuming negligible AC heating, exactly the same as the 4-point method.

In summary, the unbalanced AC heating will not lead to significant errors in the measured thermal conductance if carefully controlled to be small compared to the global ambient temperature (Zheng et al. 2013). In this case, the measured temperature rise is solely due to DC heating, stemming from heat transfer from the heating side to the sensing side. The errors will be insignificant due to the following reasons: 1) the AC sensing currents will be presenting during the whole process of the measurement, creating a constant temperature rise on both heating and sensing sides, which will not be captured by the sensing side lock-in amplifier; 2) the thermal conductance is derived by linearly fitting the heating current of DC to the ΔT_h-ΔT_s, which remains unchanged even if the true ΔT_h-ΔT_s is shifted; 3) because of the applied sensing side bridge scheme, the sensing side heating caused temperature rise is present in both the measurement and reference membranes, thus the sensing side AC current induced signal drift is balanced out.

2.5.2 Evaluation of the effect of radiation shields

There are two assumptions in the suspended microheater based thermal-bridge measurement scheme, that is, 1) the temperatures of the two membranes are uniform, which are denoted as T_h and T_s; 2) negligible radiation heat transfer. The first assumption is valid as discussed earlier. Moore et al. studied the validity of second assumption using a finite element analysis software ANSYS, revealing that the assumption could be undermined by the non-negligible radiation heat loss from the membranes and long supporting beams to the surroundings, which could result in a temperature difference up to tens of kelvin in currently used cryostats at 800 K (Moore & Shi 2011). According to their model, the radiation heat loss could lead to nonlinear temperature profiles in the long supporting beams, when the sample stage temperature is considerably higher or lower than the surrounding temperature. Although the nonlinearity alone does not necessarily cause incorrect measurement, it could cause errors in the measured temperature coefficient of resistance (TCR) of the micro-thermometer, and the errors eventually propagate into the extracted thermal conductance of the beams and samples. They claimed that the significant radiation loss could be largely nullified by addition of a radiation shield directly mounted onto the sample holder, which would ideally share the same temperature as the sample holder. In this case, the suspended membranes will also be approximately at the same base temperature as the sample holder. The addition of the extra radiation shield, as a standard practice, is exercised by several groups (Lee et al. 2016, Moore & Shi 2011, Zheng et al. 2013). However, they only studied the effects of the inner radiation shield by simulation, no experimental data thus far has been published to demonstrate the effects. In this section, a comparison of the measurement results acquired in both cases, with and without the extra inner radiation shield, on a silicon nanoribbon sample will be discussed. The two cases will be separately termed as single radiation shield, meaning that only one radiation shield is mounted between the sample and vacuum chamber shroud; and dual radiation shields, which includes a second (inner) radiation shield mounted directly on the sample holder, as illustrated in **Figure 2.13**.

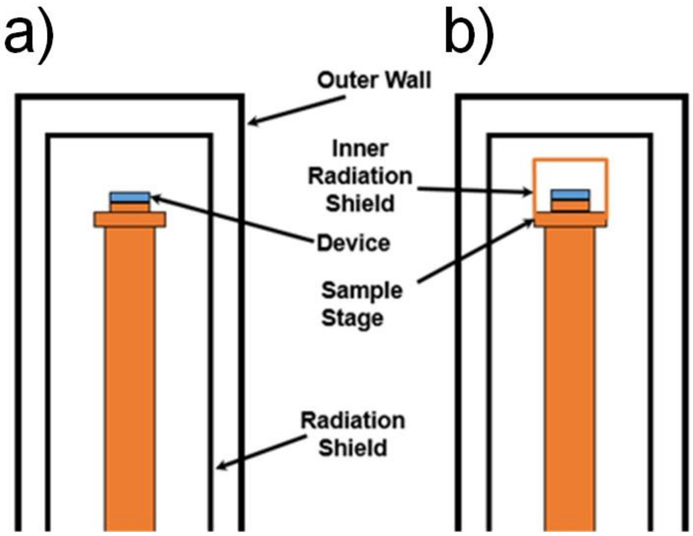

Figure 2.13 Illustration of the locations of the radiation shields with respect to the measurement device. (a) Single radiation shield, in which the radiation shield is mounted onto the base of the coldhead, which could render a temperature difference of tens of kelvins between the set and actual temperature of the sample holder at 800 K (Moore & Shi 2011). (b) Dual radiation shields, in which one extra inner radiation shield is mounted on the sample holder, and renders the sample temperature very close to the set sample holder temperature.

Figure 2.14 shows the measured thermal conductance of the sample and the supporting beams using dual radiation shield and single radiation shield schemes. The measured sample thermal conductance using dual radiation shield overlaps with the single shield case very well below 130 K and is higher for the dual radiation shield case as the temperature goes beyond 140 K with larger difference at higher temperature. The maximum difference seen at 420 K is ~30%, and the difference is anticipated to continuously increase if the measurement range extends to higher temperatures. The large difference renders it difficult to precisely understand the phonon transport physics.

Further analysis shows that this difference mainly comes from the errors in evaluating the TCRs of the micro-thermometers. The obtained resistance-temperature (R-T) curves are shown in **Figure 2.14(c)** for both cases, with the dual radiation shield curve yielding a higher resistance at higher temperatures. This seemingly insignificant resistance shift, however, leads to significant change in the fitted TCRs, as shown in **Figure 2.14(d)**. The difference could be as large as 25% for 420 K and the error eventually propagates to the measured thermal conductance, and ultimately, the extracted thermal conductivity.

The important consequence of the radiation heat transfer comes from the non-negligible temperature difference between the suspended membranes and surrounding environment. The suspended membranes and supporting beams have large SVRs, which makes them sensitive to radiation heat loss if there is a large temperature difference between these structures and the environment. In our heat transfer model of the experimental setup, all dissipated Joule heat is conducted to the substrate through the supporting beams. The chamber is in a high vacuum with an absolute pressure on the order of 10^{-6} mbar, reducing the convection through residue air to a negligible level. In fact, Zheng et al. demonstrated that the background thermal conductance only increased marginally after increasing the vacuum level from 10^{-6} mbar to 10^{-4} mbar (Zheng et al. 2013), indicating the minor contribution from convection. However, without the second radiation shield mounted on the sample holder, the suspended structures could exchange heat with the cold surroundings through thermal radiation, which could lead to non-negligible effects on the resistance of the PRT and alter the obtained TCR.

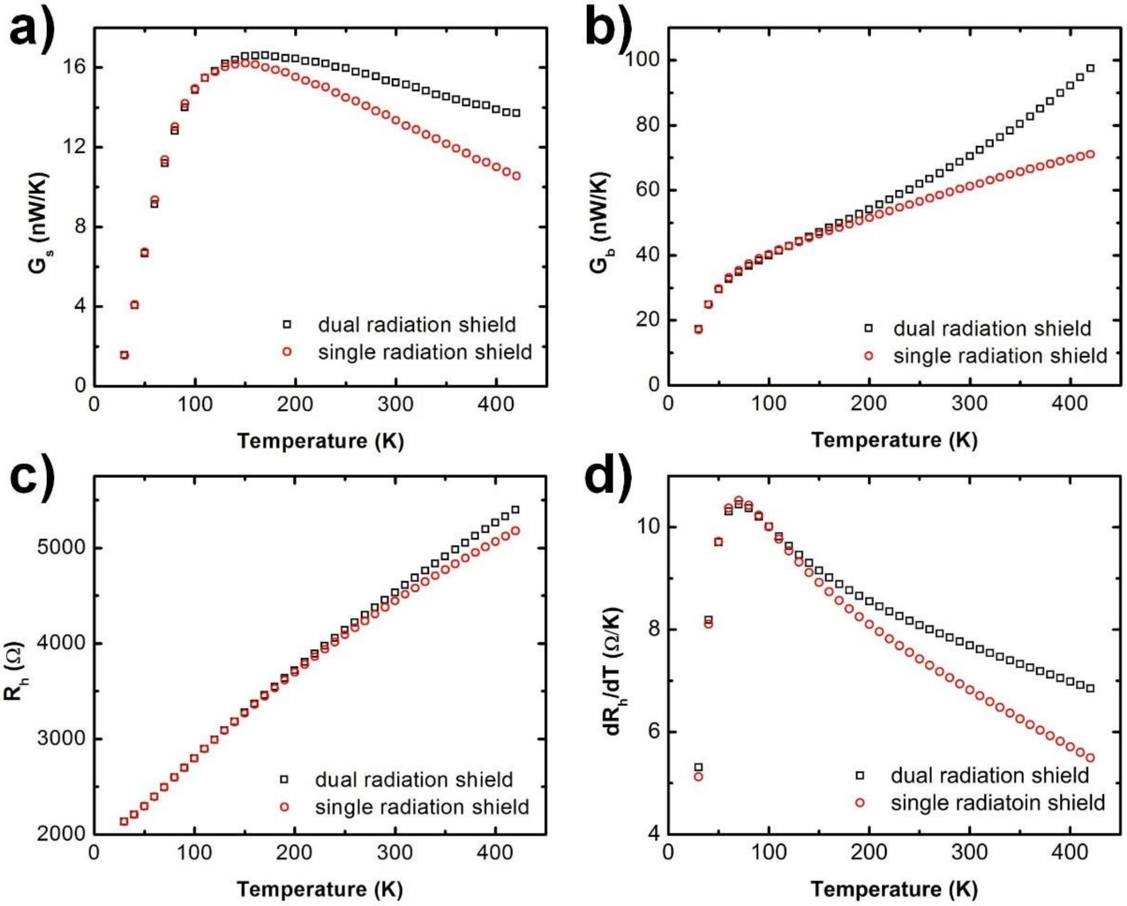

Figure 2.14 Comparison of measured quantities using single and dual radiation shield set-ups (Yang et al. 2016). (a) Thermal conductance of the silicon nanoribbon, (b) Thermal conductance of the supporting beams, (c) Resistance of heating side PRT, and (d) dR_h/dT.

As indicated in **Figure 2.14(d)**, dR_h/dT acquired for the single radiation shield case is underestimated, which will result in a higher temperature rise. According to Equation (2.3), the higher temperature rise will lead to a lower G_b, as indicated in **Figure 2.14(b)**. This seems counter-intuitive since additional radiation loss would help to transfer more heat from the membrane to the surroundings. Indeed, the heat loss is increased due to the larger temperature difference between the membranes and the environment. However, the thermal conductance acquired is a result of a differential measurement, that is, the change of the PRTs' resistance when heating current ramps from zero to I_{max}. In fact, ignoring the radiation heat transfer in conduction analysis only lead to marginal difference in the derived thermal conductance. However, the acquired different dR_h/dT could lead to a significant overestimation of the temperature rise and eventually yield a lower extracted conductivity.

It is worth noting that Moore et al.'s simulation did not take into account the temperature dependence of the thermal properties when the device, especially the suspended structure, is under a different temperature from the supposed base temperature T_0. As evidenced in **Figure 2.14(a)**, the thermal conductance versus temperature curve drops more significantly in single shield case than the dual shield scheme. The difference would only grow larger as measured temperature goes higher since the radiative heat transfer magnitude increases with temperature to the fourth power following the Stefan-Boltzmann's law. The discussion here highlights the necessity of adding an additional radiation shield and calls for extreme care in reducing radiative heat transfer in temperature sensitive measurements.

With the second radiation shield mounted on the sample holder, the temperature difference between the device and its environment is much smaller, which could remove the effects of the erroneous TCR to ensure the correctness of the assumptions. Such double shield practice is kept as a protocol and exercised in the results presented in the following chapters.

2.5.3 Background Heat Transfer

Background thermal transport between the two side-by-side suspended membranes is inevitable in the measurement based on the suspended microdevice, which mainly comes from radiative heat transfer. When the temperature difference between the two membranes is controlled to be small (ΔT_h-ΔT_s<5 K), this component is usually negligible, especially for samples with relatively large thermal conductance. However, when dealing with samples with very small thermal conductance (G_s) that is on the same order of magnitude as the background thermal conductance G_{bg}, the background heat transfer has to be taken into account.

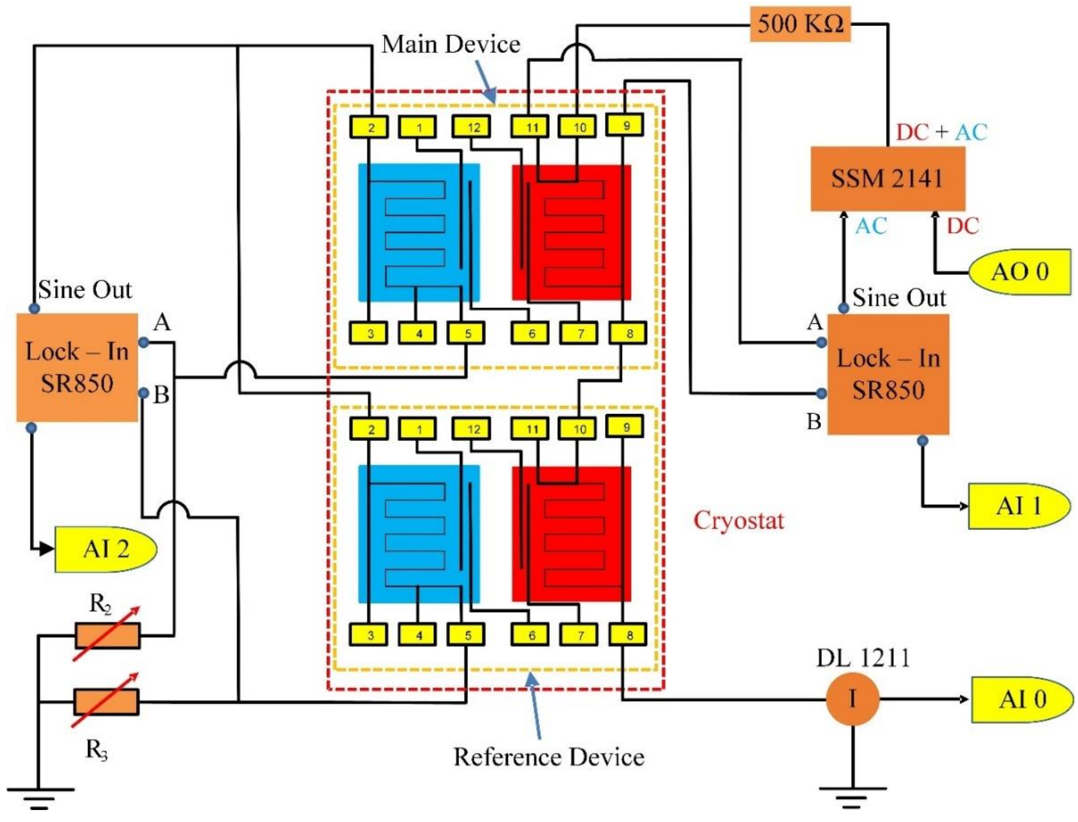

Figure 2.15 Measurement setup for background signal rejection method. The heating current passes through the heating PRT of the measurement and reference devices simultaneously, creating

roughly the same temperature rise, which ultimately are balanced out in the Wheatstone bridge method.

In the traditional 4-point *I-V* measurement, Pettes et al. measured the G_{bg} of an empty device and then subtracted the component from the measured sample thermal conductance G_s (Pettes 2011). The development of the Wheatstone bridge method offers a more direct way to reject the background signal by coupling a bare device to the circuit and applying heating simultaneously (Zheng et al. 2013). **Figure 2.15** shows the measurement setup for background signal rejection scheme. The sensing side circuit comprises of the measurement device, reference device in the cryostat, and two additional resistors in ambient environment. To reject the background signal, the heating side of the reference device must also be coupled into the DC heating circuit. The underlying assumption is that the background thermal conductance induced temperature rise, ΔT_{bg}, is the same for both devices, which will be canceled out, causing marginal change in the output bridge voltage. Therefore, the bridge voltage output, Δv_g, only carries the resistance change from the heat conducted through the nanowire sample.

In addition to the in-situ rejection, to eliminate the background thermal conductance from the measured ones, we could also use the same device having no nanowire bridging the heating and sensing membranes, to measure the background thermal conductance. Since the devices were fabricated from the same batch, sharing nominally identical structures and dimensions, it is reasonable to assume that all devices with the same gap distance have approximately the same G_{bg}. The measured G_{bg} data were fitted to a 4th order polynomial function and used as the G_{bg} that was subsequently subtracted from measured thermal conductance of the samples. The two approaches essentially yield the same results within the experimental uncertainty. Note that this is feasible only with the improved measurement sensitivity that can accurately capture the background heat transfer information.

2.6 Uncertainty Analysis

Because of the complex analysis procedure and large quantities of data involved, it is difficult to conduct an analytical evaluation of the uncertainty taking into account all the error sources. Consequently, a Monte Carlo simulation method, which does not require rigorous derivation, is adopted for the uncertainty analysis of the electrical measurements.

2.6.1 Monte Carlo Method (MCM) for thermal conductance measurements

Figure 2.16 presents a flowchart that shows the procedure involved in performing an uncertainty analysis for our thermal conductance measurement data by the Monte Carlo Method (MCM). The methodology is applicable for Data Reduction Equations that involve multiple variables (Coleman & Steele 2009). As shown in the flowchart, first the assumed true values of each variable in the results are input, including experimentally measured quantities and measurement quantities, which would be the X_{best} values that we have for each variable. Then estimates of the random standard uncertainty σ for each variable are also input. An appropriate probability distribution function is assumed for each error source. The random errors assumed come from a Gaussian distribution and the systematic error distributions are chosen based on the user's judgment for the flowchart in **Figure 2.16**. The individual error values are then added to the true values of the variables to obtain synthetic "measured" values. Using these measured values, the result is calculated through data processing. This process corresponds to running the virtual test or simulation once.

Then, the sampling process is repeated M times to obtain a distribution for the possible result values. The primary goal of this iteration process is to estimate a converged value for the standard deviation, σ_{G_s}, of this distribution. An appropriate value for M is determined by periodically calculating σ_{G_s} during the MCM process and stopping the process when a converged value of σ_{G_s} is obtained. Perfectly converged value of σ_{G_s} is not necessarily required to have a reasonable estimation. Once σ_{G_s} is converged to within 1-5%, then the value of σ_{G_s} is a good approximation of the combined standard uncertainty of the results. Assuming that the central limit theorem applies, the expanded uncertainty for the result at a 95% level of confidence is $U_{Gs} = 2\sigma_{G_s}$ (Coleman & Steele 2009).

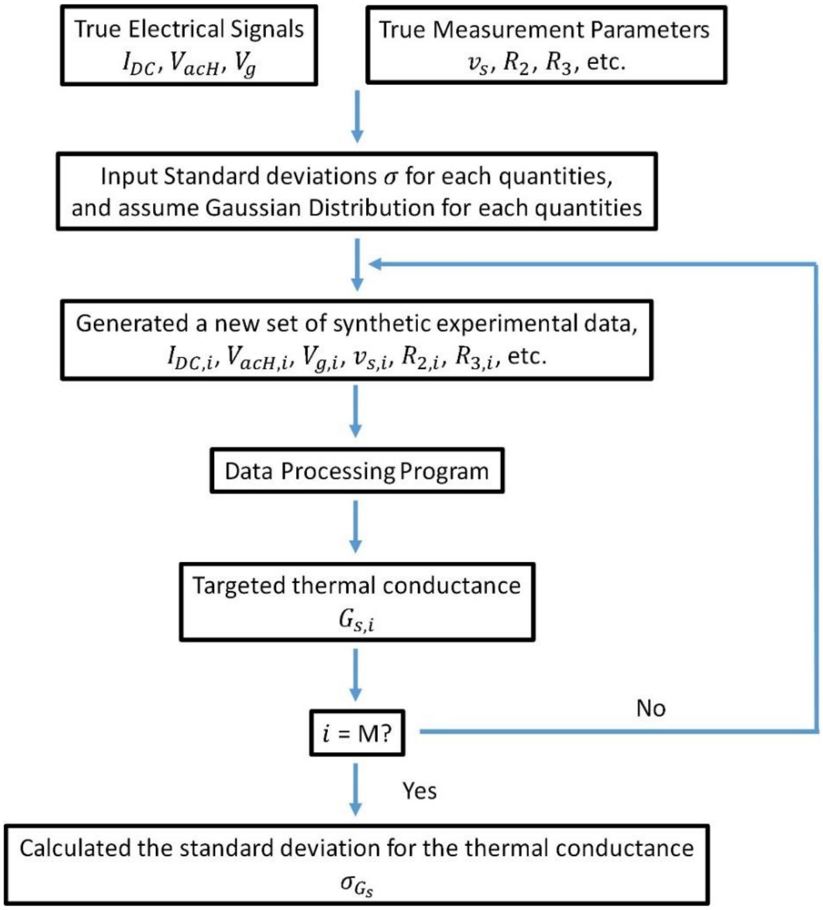

Figure 2.16 Schematic flowchart of MCM for uncertainty analysis for our thermal conductance measurements (Coleman & Steele 2009).

2.6.2 True values of variables

In the electrical measurements, we derive the thermal conductance by following quantities, i.e., the heating current, I_{DC}, the ac voltage difference on the heating coil, v_{acH}, and the AC voltage output on the sensing bridge circuit, v_{g}, the sine output of lock-in amplifier of the heating side, v_{sineH}, and that of sensing side, v_{sineS}, etc. So the assumed true values of variables needed to be input are the values of I_{DC}, v_{acH}, v_{g}, v_{sineH}, v_{sineS}, etc.

For the sine output, v_{sineH} and v_{sineS}, we can simply use the value set in lock-in as the true value. For the resistances of the 505 KΩ resistor, the measured resistance is considered as the true value.

Both v_{acH} and v_{g} are parabolic functions of the applied DC current, I_{DC}, following $v_{\mathrm{acH}} = \mathrm{a_H} + \mathrm{b_H} I_{\mathrm{DC}}^2$, $v_{\mathrm{g}} = \mathrm{a_g} + \mathrm{b_g} I_{\mathrm{DC}}^2$, respectively. The four coefficients in these equations are calculated/fitted during the experimental data processing using Igor Pro 4.0 and are used to calculate the true values of v_{acH} and v_{g} at a given I_{DC}.

2.6.3 Random and systematic uncertainty analysis of variables

All the error sources in the setup are shown in **Figure 2.17** denoted by a red ellipse. The ellipse across leg 9 and leg 10 denotes the error of R_{tot}, which is the electrical resistance between pad 8 and 11. The error of the cryostat is the error of the base temperature of the device in the cryostat. Detailed analysis of these error sources is given as follows.

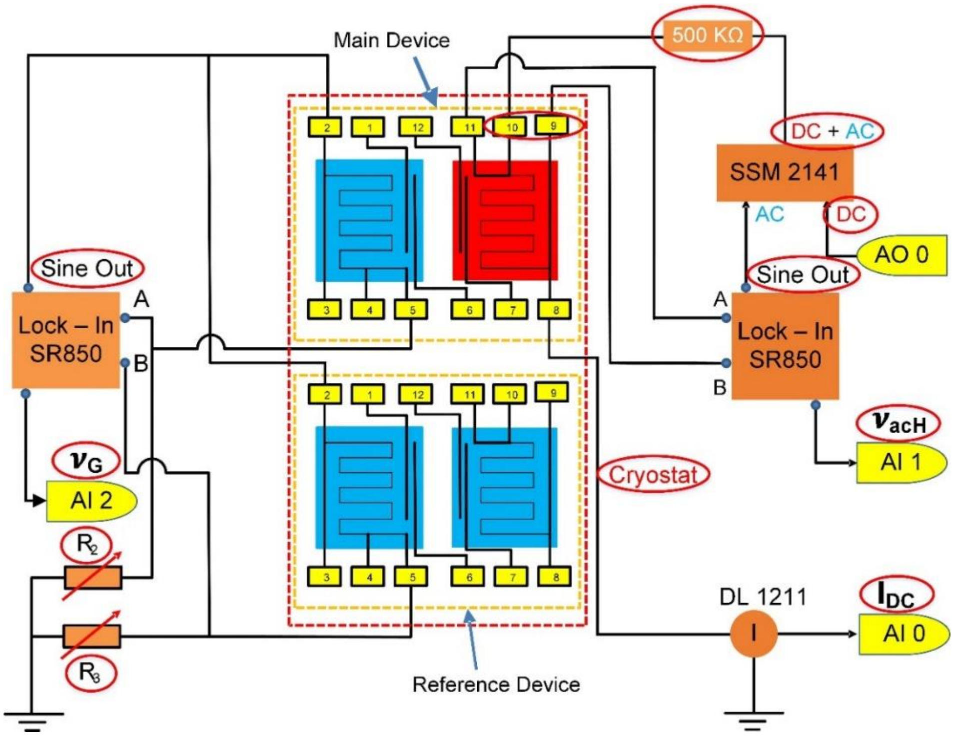

Figure 2.17 Error sources in the electrical measurement setup.

Error of v_{acH} and v_g

In order to measure the random uncertainty of v_{acH} and v_g, the DC input of SSM2141 is set as 0.0 V. At 300 K, the data acquisition program used in the thermal measurement is run and 594 points are recorded in a total time of 2.5 hrs. The parameters of the lock-in amplifiers are the same as we used in thermal measurements: 50 for the heating side expand, 5 mV for the heating side sensitivity, 20 μV or 50 μV for the sensing side sensitivity, and offsets are selected so that the output of the lock-in amplifiers are about 1 V. The gain of the current preamplifier is 10^5 V/A, which is also the gain used in real measurements.

When the sensitivity of sensing side is set as 20 μV, the standard deviations obtained are 0.0040 V and 0.0019 V for v_{acH} and v_g, respectively, which correspond to 0.008 V and 0.0038 V random uncertainties for v_{acH} and v_g. The standard deviation and uncertainty of v_g for sensitivity of 50 μV are 0.00085 V and 0.0017 V, respectively, which are approximately 0.4 time of the values for 20 μV. The random uncertainties of v_{acH} and v_{g} we obtained include the contribution of errors from the lock-in amplifiers, SSM2141, DAQ hardware and the resistance changes resulting from cryostat base temperature fluctuation. The error of lock-in amplifier is composed of four parts: one is the error induced by the circuit inside the lock-in amplifier, the second is the error in expand, the third is the error in the offset, and the fourth is the random error of sine output.

In order to measure the zero offsets of v_{acH} and v_{g}, a BNC T connector is used to connect the input A to the input B of the lock-in amplifier. Because the signal of input A equals to that of input B, the ideal output should be zero. Thus, the average of the outputs we measured can be considered as the zero offsets of v_{acH} and v_{g}. The zero offset values we got are 0.00333 V and 0.01 V for v_{acH} and v_{g}, respectively.

The zero offsets of v_{acH} and v_{g} given by the measurement include the contribution from the lock-in amplifier and DAQ hardwares.

Error of I_{DC}

The random uncertainty and zero offset of I_{DC} were measured simultaneously with the random uncertainty measurement of v_{acH} and v_{g}. The gain of the current preamplifier is 10^5 V/A. The standard deviation is 0.0001 V. Thus, the random uncertainty of I_{DC} is about 0.0002 V. The average of the data points is considered as the zero offset of I_{DC} and is -0.0022 V. The random uncertainty of I_{DC} includes the contributions from the current preamplifier, the DAQ hardware, the SSM2141, and the cryostat. The zero offset of I_{DC} are considered in the data processing process.

Error of temperature

There are two error sources for base temperature, which should be discussed separately. First, the temperature of the position where the thermocouple is mounted, T_{b}, and the temperature of the device, T_d, as shown in **Figure 2.18**, could be slightly different. The error of T_b depends on the sensor used. In our system, it is a DT-670B silicon diode thermometer, monitored by a Cryo-con 32 temperature controller. The accuracy of this kind of configuration is not presented in the manual of Cryo-con 32 temperature controller. Here we assume that the accuracy of our control system is approximately the same as that of a system with a silicon diode sensor followed by a Cryo-con 32 temperature controller, which is ±32 mK at room temperature as given in the manual. Thus, the systematic uncertainty of the T_b is taken as B_{Tb}=32 mK.

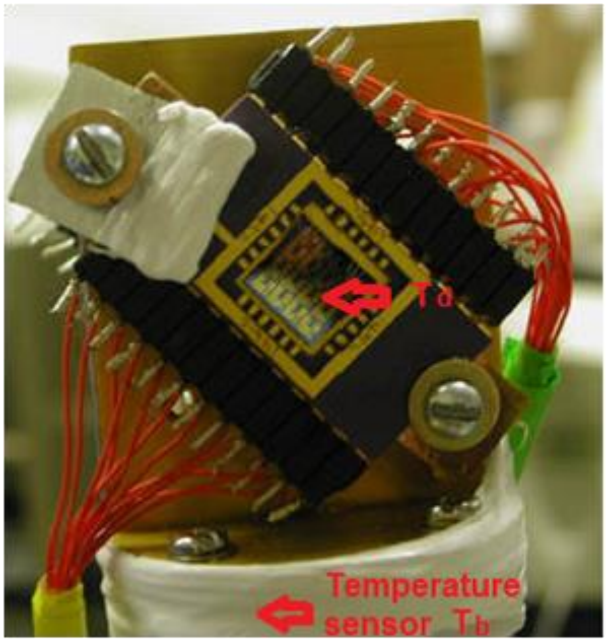

Figure 2.18 A photo showing a device mounted on the sample holder with locations of the temperature T_d and T_b marked.

The random uncertainty can be determined from the data read from the temperature controller. After an equilibration period of 40 mins, the accuracy of the reading is ±2 mK. Thus, the random uncertainty of the T_b is P_{Tb} = 4 mK and the total uncertainty of sensor temperature $U_{Tb} = \sqrt{B_{Tb}^2 + P_{Tb}^2}$ =33 mK. According to the calibration conducted by Juekuan Yang (Southeast

University), the difference between T_b and T_d is around 0.5 K, when double layers of radiation shields are mounted.

From the log file created by the DAQ program, we know that one sweep cycle takes about 20 minutes. In our measurements, we sweep 1 cycle at each temperature point. The time needed for taking data is about 20 minutes, roughly corresponds to half a cycle of the temperature fluctuation. So the contribution of the variation of T_b and T_d to the uncertainty of the measurement has been considered in the random errors of I_{DC}, v_{acH}, and v_{acS} and does not need to be considered separately.

The only important factor that remains unconsidered here is the systematic error of T_b, which is 500 mK, as described above. The difference could be corrected by incorporating another sensor of higher accuracy directly taped onto the DIP. However, the offset is much lower than the temperature rise required to perform the measurement and can be considered as an error in the baseline temperature. As such, we neglect the temperature offset in the uncertainty analysis.

Error of the sine output of the lock-in amplifier

As given in the manual of the SR 850 lock-in amplifier, the systematic error of the sine output is 0.2%. As mentioned earlier, the contribution of the random uncertainties of the sine output has been considered in the random uncertainties of v_{acH} and v_S.

Error of the electrical resistance

The error of the electrical resistance of four resistors in the circuit need to be considered: the resistance of R_2, R_3, the resistance of the 500 KΩ resistor, and the resistance between pad 8 and pad 11 ($R_{totH}=R_{coilH}+2R_{LH}$) at 300 K. All of these resistances are measured by a Triplett 4404 digital multimeter. Generally, the accuracy of digital multimeter is (0.1%+1) to (0.7%+1). We conservatively use B_R=1%.

2.6.4 Overall uncertainty

We obtain the thermal conductance of the sample (G_s) from the electrical measurements. The measurement uncertainty is estimated by the Monte Carlo simulation as described in the previous sections. In order to get the thermal conductivity of the sample (κ_s), which is related to the thermal conductance G_s as:

$$\kappa_s = G_s \frac{L}{A}, \tag{2.27}$$

where L is the length of the sample suspended between the heat source and heat sink, and A is the cross-sectional area of the sample. Both L and A are determined through advanced microscopy tools such as SEM, TEM, or AFM. If U_L and U_A represent the uncertainties of the measured value of L and A at a 95% level of confidence, then the overall uncertainty of thermal conductivity U_κ can be calculated following the standard approach of uncertainty propagation as (Coleman and Steele, 2009):

$$U_\kappa^2 = (\frac{\partial \kappa}{\partial G_s})^2 U_{G_s}^2 + (\frac{\partial \kappa}{\partial L})^2 U_L^2 + (\frac{\partial \kappa}{\partial A})^2 U_A^2 . \tag{2.28}$$

Dividing both sides of Equation (2.28) by κ^2, we get the overall uncertainty of measured thermal conductivity as

$$(\frac{U_\kappa}{\kappa})^2 = (\frac{U_{G_s}}{G_s})^2 + (\frac{U_L}{L})^2 + (\frac{U_A}{A})^2 . \tag{2.29}$$

For thermal conductivity measurement for nanowires of diameter D, the expression could be written as

$$(\frac{U_\kappa}{\kappa})^2 = (\frac{U_{G_s}}{G_s})^2 + (\frac{U_L}{L})^2 + 4(\frac{U_D}{D})^2 . \qquad (2.30)$$

For thermal conductivity measurement presented in this dissertation, majority of the uncertainty comes from the geometrical dimension characterization. For example, for a 53 nm PE nanofiber at 300 K, the thermal conductivity is measured to be 9.07 W/m-K, whose uncertainty is 12.13 percent, or 1.1 W/m-K. Table 2.1 lists the uncertainty for each component of the Equation (2.29), showing that most of the uncertainty originating from the cross-sectional area characterization.

Table 2.1 Composition of the uncertainty for a 53 nm PE nanofiber at 300 K

	Thermal Conductivity K_s (W/m-K)	Thermal Conductance G_s (nW/K)	Length L (µm)	Cross Sectional Area A (nm^2)
Measured Value (X)	9.07	2.84	6.96	2181.28
Uncertainty (U_X)	1.11	0.0979	0.2	238.34
U_X/X (%)	12.24	3.447	2.87	11.385

2.7 Summary

In this chapter, we discussed in details the experimental measurement approach including the experimental setup, sample preparation, data analysis, and uncertainty analysis. The effects of an additional radiation shield mounted on the sample holder, excessive AC heating effects, and background heat transfer through radiation are also thoroughly analyzed. With the improvement of the experimental setup, the measurement is now significantly more precise and sensitive. In particular, the common mode rejection scheme realized through the introduction of the Whitestone bridge circuit on the sensing side with the assistance of a reference device eliminate the effects a major noise source of baseline temperature fluctuation, which extends the lower limit of the thermal conductance measurement to the order of 10 pW/K.

3. Thermal Conductivity of Individual Electrospun Polymer Nanofibers

Electrospun nanofibers and nanofibrous mats have been extensively tested as scaffolds for cell culture, light sources, waveguides, transistors, gas sensors, zeptomole scale reactors, fuel cell proton exchange membranes, templates for nanopatterning, as well as filters to trap minute particles without significantly impeding air flow (Bhardwaj & Kundu 2010, Liang et al. 2007, Liu et al. 2015). To date, most electrospun nanofibers are made of polymers, one of the most dominant categories of materials in modern civilization, with innumerable applications in industry and everyday life. As the small fiber size and high surface area of electrospun mats are attractive for many applications, systems for electrospinning at a commercial scale (e.g. Nanospider^{TM} by Elmarco and Nanospinner416 by Inovenso) are already available. A wide range of products containing electrospun nanofibers are currently for sale, illustrating the scalability of the manufacturing process.

Electrospinning can produce well-aligned polymer nanofiber arrays with ordered molecular chains inside each fiber, pointing to the possibility of large-scale manufacturing of nanofibers with high thermal conductivity. However, there are only very limited studies on the thermal conductivity of individual electrospun nanofibers. A recent study showed that the thermal conductivity of single Nylon-11 electrospun fibers could be as high as 1.6 W/m-K, nearly one order of magnitude higher than the typical Nylon-11 bulk value of around 0.2 W/m-K (Zhong et al. 2014). However, all the electrospun nanofibers studied in the above-mentioned report were produced with a relatively low voltage of 6-7 kV, with no attempt made to push the limit of the thermal conductivity by tuning the processing conditions. One more study on electrospun polystyrene nanofibers shows that the measured thermal conductivity of individual polystyrene nanofibers fabricated at 7-10 kV could have a thermal conductivity ranging from 6.6 and 14.4 W/m-K, a significant increase from the typical bulk values for polystyrene (Canetta & Narayanaswamy 2013). The increased thermal conductivity of electrospun nanofibers has been attributed to the aligned molecular chains resulted from the high strain rates within the electrospinning jets.

In this chapter, we report on measurements of the thermal conductivity of electrospun PE nanofibers prepared under different electric fields to explore the effects of electric field intensity on the molecular alignment and resulted thermal conductivity. Micro-Raman characterization was conducted on individual nanofibers to identify their structures and to establish the relation between structure and thermal conductivity. We choose to study PE nanofibers because of their simple molecular structure, and the promising results obtained from ultra-drawn PE nanofibers (Li et al. 2014, Shen et al. 2010). We also showed that electrospinning of other material systems, such as polyvinylidene fluoride (PVDF) and Nylon-6 also see significant enhancement of thermal conductivity compared to their bulk counterparts. A fast-production of nanofibers using direct tip-drawing method also proves to be an effective approach to produce chain-aligned nanofibers with enhanced thermal conductivity.

3.1 Electrospinning of Polyethylene Nanofibers

Electrospinning has become a widely used technique to form nanofibers from a variety of materials with diameters ranging from tens of nanometers to a few microns (Li & Xia 2004, Li et al. 2003a). In a typical electrospinning process, a solution of polymer molecules dissolved in solvent is supplied to the tip of a sharp conductor, such as a syringe needle. A high voltage is applied between the conductor and a grounded collector. Under the influence of the strong electric field, the polymer solution forms a cone (often called a Taylor cone), from which a jet is accelerated towards the grounded collector. This jet is a strong elongational flow and becomes thinner as it approaches the collector. Due to the very large surface-area-to-volume ratio of the jet, the solvent evaporates quickly, leaving a solid fiber that is deposited on the collecting surface. It is worth noting that a "whipping" instability often results in a jet path that is longer than the tip-collector distance and causes the fiber deposition to move chaotically over the collector. This could lead to a significant variation in the structure and property of the nanofibers from a single deposition.

To electrospin PE, we first dissolved ultrahigh molecular weight PE powder (molecular weight $3\sim6\times10^6$) in p-xylene and cyclohexanone mixture solution (all materials from Sigma-Aldrich, Inc.). P-xylene is a well-known solvent for PE. However, the electrical conductivity of p-xylene is very low, with a value of ~3 pS/m. In addition, the dielectric constant of p-xylene is only about 2.4. As such, to boost the electrical conductivity and dielectric constant of the solution, cyclohexanone was added to p-xylene at a 1:1 weight ratio. To prepare the solution, the solvent mixture was first heated to 120°C and then 0.1 wt% of PE powder was added. The PE solution was stirred at 120°C until the powder was completely dissolved, and then the solution was poured into a glass syringe that was preheated to 120^{o}C. The glass syringe was placed on a syringe pump with a 20-gauge metal needle attached to the end. To keep the temperature of the PE solution at ~120°C, an infrared quartz radiant heater (Optimus HT-511) was placed on one lateral side of the syringe and needle, as shown in the schematic of the set-up in **Figure 3.1(a)**. The syringe pump was set to generate a constant flow rate of 200 μl/min.

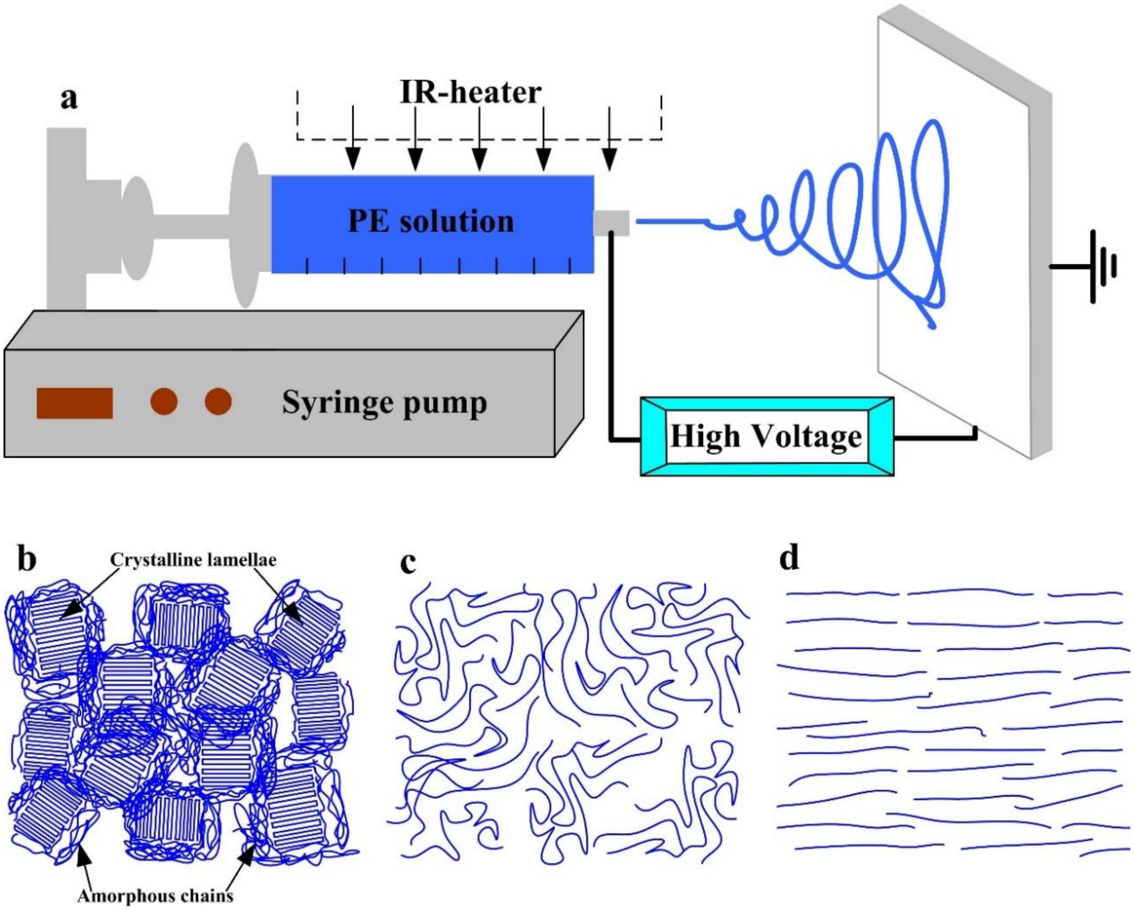

Figure 3.1 Electrospinning of PE nanofibers. a. Schematic of PE electrospinning at elevated temperature using an infrared heating system. b-d. A schematic model of structural changes of the PE molecules at each fabrication step. (b) PE powder with crystalline lamellae and amorphous regions in solid state. (c) Extended PE molecule chains dissolved in the solvent with random orientations. (d) During the electrospinning process, the PE molecule chains get aligned.

It is well known that in the PE powder, some PE molecular chains are folded locally in the form of small crystallites, usually termed as "lamellae" (Li et al. 2014), while other molecular chains are randomly distributed (**Figure 3.1(b)**). When the PE powder completely dissolved in the solvent, both lamellae and entangled molecular chains dissolved in a random distribution (**Figure 3.1(c)**). During the electrospinning process, the random molecular chains will be aligned in an ordered fashion as shown in **Figure 3.1(d)**. The electrospinning deposition was performed at a wide scope of voltages ranging from 9 kV to 52 kV, with a fixed distance of 150 mm between the tip of the spinneret and the collector. The fibers were collected on small pieces of silicon wafers for examination by Raman and on PDMS membranes for transfer to thermal conductivity measurement devices. The high voltage was supplied by an EMCO DX250 DC-DC converter. Even though the manufacturer specified voltage limit is up to only 25 kV, we successfully extracted up to 52 kV, as measured with a BK precision high voltage digital multimeter probe (BK PR-28A).

3.2 Structural and Thermal Characterization of the Nanofibers

The as-spun fibers were collected by a piece of PDMS, as shown in **Figure 3.2(b)**. Using the home-built micromanipulator as described in chapter 2, individual nanofiber was cut by the sharp tip and then transferred to bridge the two suspended membranes for following thermal measurement starting from 320 K to 100 K. Post the thermal measurement, the geometrical information of the measured fiber was extracted using SEM (**Figure 3.2(c)** and **(d)**).

No contact treatment was done to minimize the contact thermal resistance between the fiber and the suspended membranes. The electron beam used in Pt-C contact deposition were found to pose a negative impact on the suspended segment of the polymer fiber (Zhong et al. 2014). Thus, the reported results represent a lower bound for the true thermal conductivity. It is worth noting that for all samples, the contact length between the nanofiber and the suspended membranes is quite long, and the nanofibers stick well to the suspended membrane. These facts, together with that the measured thermal conductivity is still relatively low, which corresponds to a relatively large fiber thermal resistance, suggest that the contribution from the contact thermal resistance is small compared with the resistance of the fiber itself. In the study of Zhong et al. study (Zhong et al. 2014), they have proven that the contact thermal resistance was an insignificant portion of the total measured resistance. We have further evaluated the thermal contact resistance with their theoretical model, which showed that the contact resistance contributed less than 5% of the total measured thermal resistance.

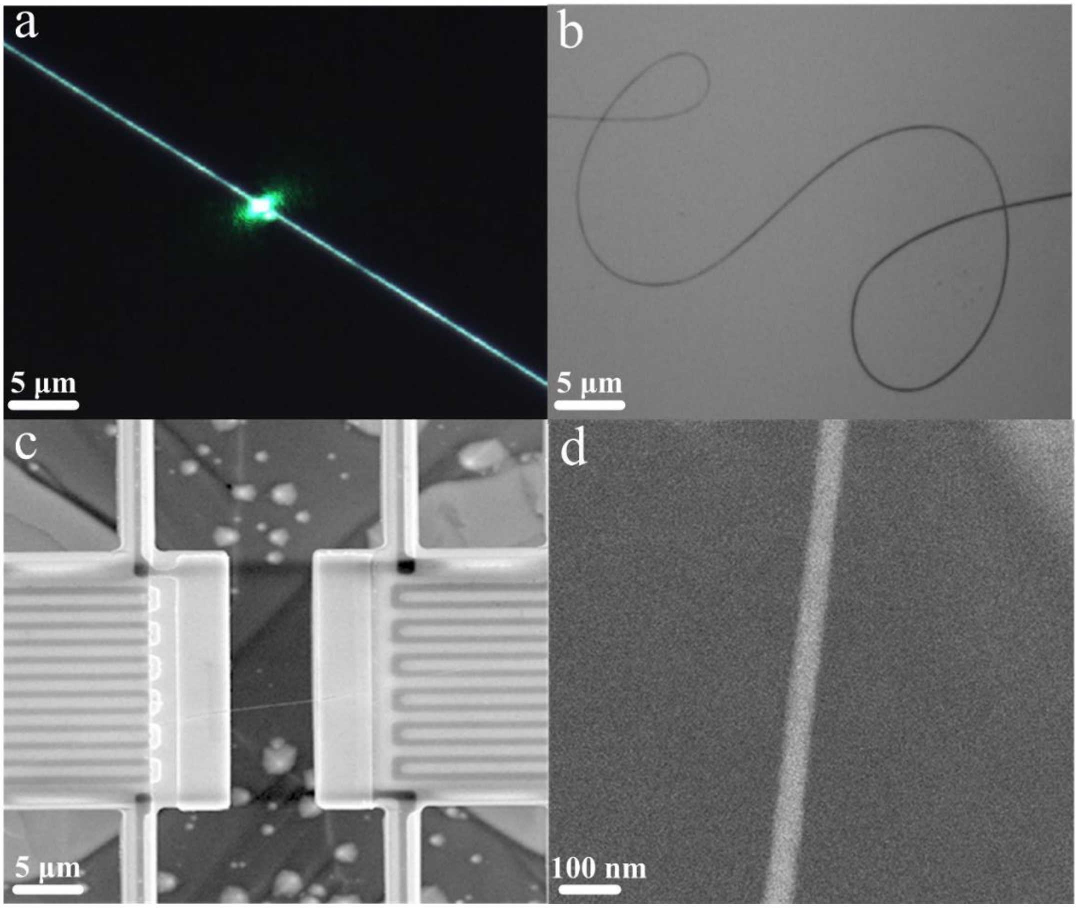

Figure 3.2 Morphology of PE nanofibers. (a) An optical image of a laser spot focused on a PE nanofiber for Raman measurement. (b) A single PE nanofiber collected on PDMS membrane. (c) An SEM micrograph of a single nanofiber suspended between two adjacent SiN_x membranes. (d) A high magnification SEM micrograph of a PE nanofiber of 56 nm diameter.

Structural characterization techniques such as X-ray diffraction (XRD) and infrared spectroscopy are usually used to study electrospun nanofibers; however, these measurements are typically performed on large bundles in order to achieve acceptable signal-to-noise ratios. Raman spectroscopy offers many advantages for the study of individual fibers, as it provides molecular level information about conformation, interactions, and crystallinity, yet only requires a small sample volume. Over the past two decades, Raman spectroscopy has been widely used to characterize PE and the corresponding vibrational modes of the Raman bands are well documented (Sato et al. 2002, Wang et al. 1982, 1991). More recently, Bellan and Craighead proposed using micro-Raman to characterize the molecular orientation within single nylon-6 electrospun nanofibers (Bellan & Craighead 2008). The internal normal modes between 1000-1600 cm^{-1} are commonly used to study morphological structure and can be divided in three vibrational regimes: the C-C stretching between 1000 and 1200 cm^{-1}, which are sensitive to molecular orientation, stress and conformation; the $-CH_2-$ twisting vibrations around 1295 cm^{-1}, which can be used as an internal standard; and the $-CH_2-$ bending modes between 1400 and 1470 cm^{-1}, which are sensitive to chain packing (the 1416 cm^{-1} band is assigned to orthorhombic crystallinity). The detailed assignment of bands in the Raman spectrum of PE is given in Table 3.1.

Table 3.1 Band assignments for Raman spectra of PE

Band (cm^{-1})	Assignment	Feature
1060	Asymmetric C–C stretching	crystalline, anisotropic
1080	C–C stretching	amorphous
1130	symmetric C–C stretching	crystalline, anisotropic
1166	CH_2 rocking	crystalline
1295	CH_2 twisting	crystalline, anisotropic
1360	CH_3 wagging	amorphous
1415	CH_2 bending	crystalline
1436	CH_2 bending	anisotropic
1459	CH_2 bending	anisotropic

To characterize the molecular orientation of PE, a semi-quantitative approach was utilized based on the ratio of the 1130 cm^{-1} and 1060 cm^{-1} Raman bands. These two bands have different vibrational symmetries. The 1130 cm^{-1} Raman band is thought to arise from the C-C symmetric stretching of the all-trans PE chain segments while the 1060 cm^{-1} band is due to the two degenerated C-C antisymmetric stretching. If the molecules are oriented in a preferred direction, the 1130 cm^{-1} band has been reported to become stronger with respect to the 1060 cm^{-1} band. For the purpose of microstructural characterization, it is necessary to first verify that during the characterization process with micro-Raman spectroscopy, heating from the laser would not significantly alter the structure of the nanofiber sample.

Figure 3.3 shows three Raman spectra taken at the same position of two nanofibers electrospun at different voltages with a laser power of 10 mW. Each spectrum was accumulated for 1 minute (Note that to further minimize the damage from the Raman characterization, a laser power of 0.01 mW was used during the alignment process).

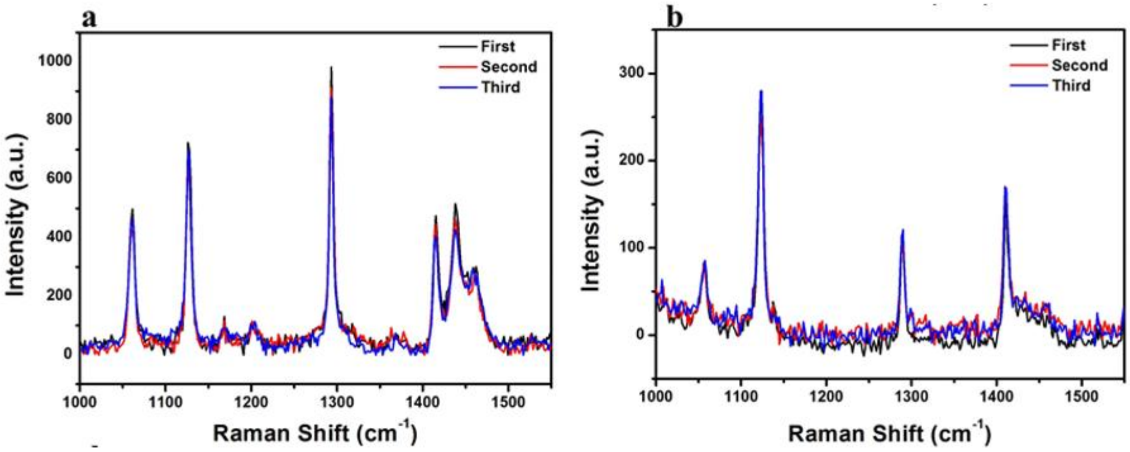

Figure 3.3 Raman spectra acquired at the same position on two PE nanofibers fabricated at different voltage. (a) The fiber was electrospun at 15 kV. (b) The fiber was electrospun at 40 kV. These three Raman spectra essentially overlap, suggesting negligible damage due to the incident laser light.

These three Raman spectra essentially overlap with each other, suggesting marginal microstructural alteration while undergoing Raman characterization. We subsequently used this technique to characterize the ultra-high molecular weight PE powder and nanofibers prepared at various voltages (see **Figure 3.5**). The Raman spectra for fibers fabricated at higher electrospinning voltages, which are very different from the PE power as shown in **Figure 3.5**, further indicate that the laser power in the Raman characterization will not drastically alter the structure of the fiber because otherwise all spectra should be similar to that of the PE powder.

3.3 Thermal conductivity of electrospun PE nanofibers

3.3.1 Enhanced thermal conductivity with electrospinning voltage

Figure 3.4(a) shows the room temperature thermal conductivity of electrospun PE nanofibers at different electrospinning voltages. As mentioned previously, the whipping instability typically seen in an electrospinning jet can lead to variations in the deposited fibers during a given electrospinning process. As such, the measured thermal conductivities for fibers fabricated under the same electrospinning voltage can vary significantly. However, despite this variation, there is a clear trend of enhanced thermal conductivity as the electrospinning voltage increases. In fact, even at a relatively low voltage of 9 kV, the thermal conductivity of the measured PE nanofiber is about 0.8 W/m-K, about two folds of the bulk value for high density PE (0.4 W/m-K).

It is widely accepted that stretching crystalline polymer films and fibers can modify the crystalline structure or induce crystal transition in their structure. During the electrospinning process, the PE molecular chains experience a strong elongational force, which gives rise to PE fibers with a high degree of molecular orientation and a better crystallinity. In general, the higher the applied electrospinning voltage is, the stronger the elongational force will be, and thus, fibers will be composed of more aligned molecules and of higher crystallinity. Therefore, it is reasonable to observe higher thermal conductivity values as the electrospinning voltage is increased. In fact, the highest thermal conductivity measured at each electrospinning voltage increases almost linearly with the fabrication voltage.

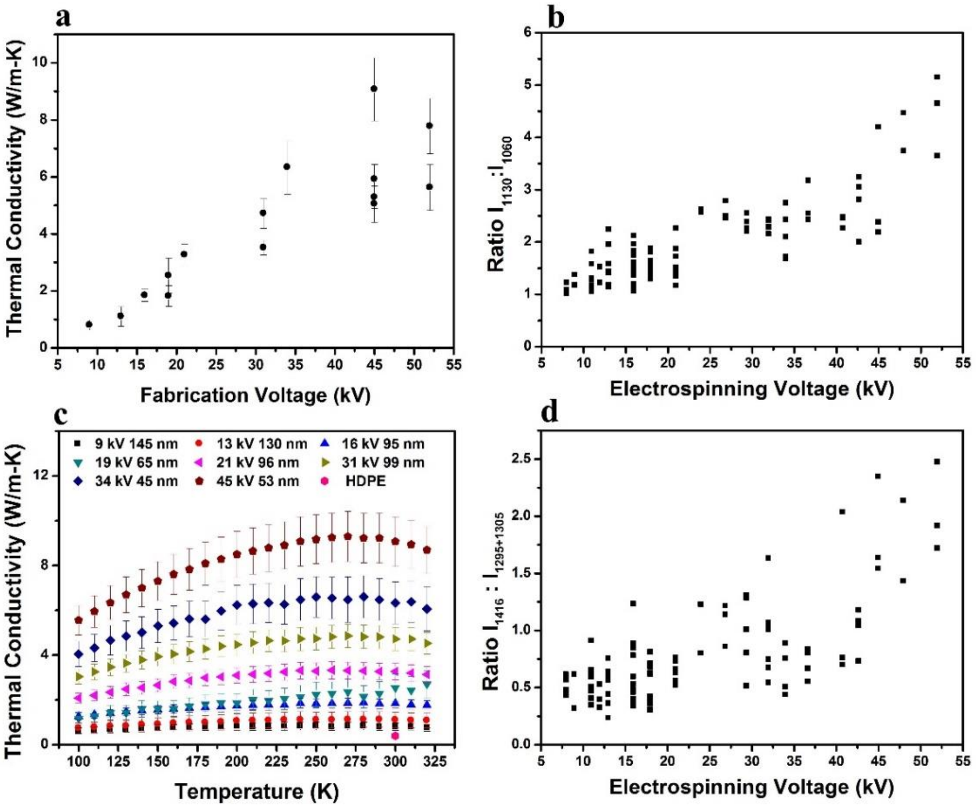

Figure 3.4 Thermal conductivity and structural characterization of PE nanofibers. (a) Room-temperature thermal conductivities of the PE nanofibers, which increases as the electrospinning voltage gets larger. (b) The intensity ratio of the 1130 and 1060 cm^{-1} bands, which can be used as a qualitative description of the molecular orientation in PE. This ratio increases with the electrospinning voltage, indicating a better molecular orientation. (c) Temperature dependence of thermal conductivity of electrospun fibers. The uncertainty of the measured data mainly comes from the fiber dimension characterization. (d) The fraction of orthorhombic phase is proportional to the band area ratio $I_{1416}/I_{1295}+I_{1305}$. As the electrospinning voltage increased, the fraction of orthorhombic phase increased (Ma et al. 2015b).

The highest thermal conductivity we measured is 9.3 W/m-K, which is obtained with an electrospinning voltage of 45 kV. Even though it is expected that higher thermal conductivity could be achieved at 52 kV, the highest value measured is only 7.8 W/m-K from the two fibers prepared with 52 kV, which could be due to a few reasons. First, due to the limitations of our instrumentation, 52 kV was the highest voltage we could achieve, with problems such as strong arcing occurring at this voltage. Secondly, there is a trade-off between the stronger electrical field and shorter flight time in the electrospinning process. O. Ero-Phillips et al. found that there exists an optimum voltage to achieve the highest degree of crystallinity in electrospun Poly (L-lactic acid) (PLLA) (Ero-Phillips et al. 2012). At electrospinning voltages higher or lower than the optimum voltage, the degree of crystallinity would drop to a lower level. This is because while a higher electrospinning voltage exerts a stronger stretching force, the flight time is shorter, thus leaving less time for crystalline structure formation. No matter what the reason is, it is worth exploring how to optimize the fabrication set-up to extend the applied electrospinning voltage to higher values and observe whether even larger values of thermal conductivity can be achieved.

The Raman spectroscopy further verified that the thermal conductivity enhancement is indeed due to the structural change. As shown in **Figure 3.4(b)**, as the electrospinning voltage increases, the intensity ratio of the 1130 cm^{-1} and 1060 cm^{-1} bands becomes significantly larger, indicating that the molecular chains in the fibers are better aligned. To further investigate molecular orientation in the PE nanofibers, we measured the Raman spectra on multiple samples prepared at different voltages. **Figure 3.4(b)** shows the correlation between the 1130/1060 band intensity ratio and the electrospinning voltage. This ratio for ultra-high molecular weight PE powders is about 1.16. For nanofibers fabricated with relatively low electrospinning voltages, this ratio is close to the powder value. As the voltage gets larger, there is a clear increasing trend for the obtained 1130/1060 ratio, suggesting that the PE chains experience a stronger elongational force at higher electrospinning voltage, which results in fibers with a higher degree of molecular orientation.

To further observe the temperature dependence of the PE nanofibers, **Figure 3.4(c)** shows the thermal conductivity of PE fibers fabricated from 9 kV to 45 kV at temperatures ranging from 100 to 320 K. Note that the thermal conductivity of the nanofiber sample with the highest measured values at each electrospinning voltage was plotted in **Figure 3.4(c)**. These data suggest that while the thermal conductivity for fibers prepared at low voltages remains nearly the same or only increases marginally with temperature in the whole temperature range, the thermal conductivity of fibers prepared at higher electrospinning voltages increases clearly from 100 K to 250-270 K. Beyond 250-270 K, the thermal conductivity starts to drop as temperature increases further, which is a signature of phonon UmKlapp scattering (Wang et al. 2013, Zhong et al. 2014). The different temperature dependence indicates that as the electrospinning voltage increases, the crystallinity level increases, leading to UmKlapp scattering, which is a signature of phonon transport in crystalline materials (Kittel 2004).

3.3.2 Raman characterization of molecular orientation and crystallinity

The crystalline phase of PE is primarily orthorhombic, although it has been suggested that monoclinic structures coexist under certain conditions, including uniaxial deformation (Bellan & Craighead 2008, Sato et al. 2002). The band at 1416 cm^{-1} has been unanimously assigned to the orthorhombic crystalline phase while attribution of other bands exclusively to the amorphous or crystalline phase is still a matter of debate. According to the Raman spectra of PE nanofibers (**Figure 3.5**), it is clear that the 1416 cm^{-1} band, or the orthorhombic crystallinity, becomes stronger as the voltage increases.

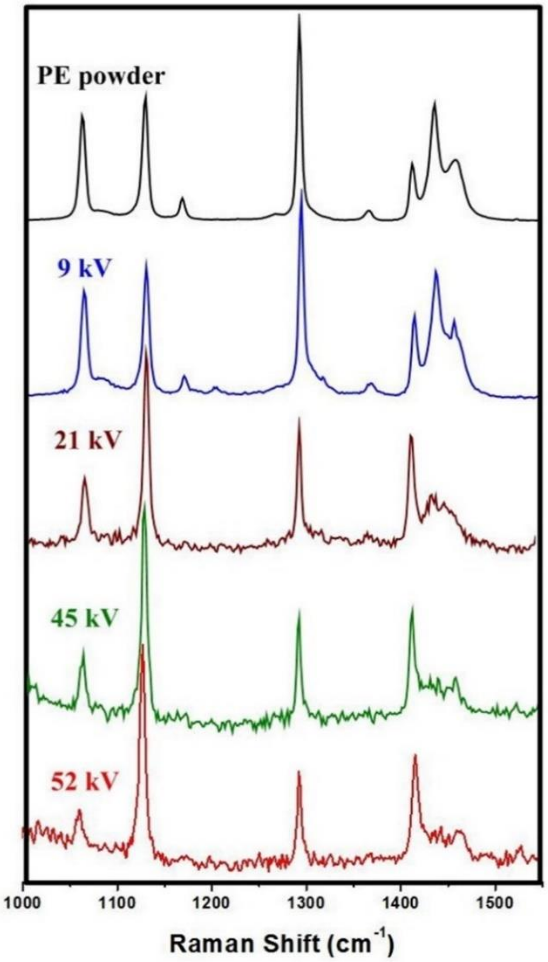

Figure 3.5 Raman spectra of PE powder and PE nanofibers prepared at different voltages. As the electrospinning voltage increases, the band at 1130 cm^{-1} enhances while the band at 1060 cm^{-1} decreases. The intensity ratio of the 1130 and 1060 cm^{-1} bands is an indicator of the molecular orientation in PE. Additionally, the band at 1416 cm^{-1} (assigned to orthorhombic crystallinity) becomes stronger as the electrospinning voltage increases.

To more quantitatively determine the fraction of the orthorhombic crystalline phase, amorphous phase, and intermediate phase, we utilize the curve fitting algorithm provided in the LapSpec software package. Following Strobl and Hagedorn (Strobl & Hagedorn 1978), the orthorhombic crystallinities can be calculated according the band areas ratio of $I_{1416}/I_{1295+1305}$:

$$\%\text{orthorhombic crystallinity} = (I_{1416}/I_{1295+1305})\times(100/0.45), \quad (3.1)$$

where I_{1416} is the areas underneath the Raman bands at 1416 cm^{-1}, $I_{1295+1305}$ is the area underneath the internal standard band group. Note that this formula could only be used to calculate the Raman crystallinity of isotropic sample. For highly oriented systems, Lagaron et al. suggested that the influence of the molecular orientation should be fully removed or the Strobl and Hagedorn formula cannot be directly applied (Lagaron et al. 1999). They provided a modified formula with a correction factor, *K*, for additional orientation effects.

$$\%\text{orthorhombic crystallinity} = (I_{1416}/I_{1295+1305})\times(100/0.45)\times K. \tag{3.2}$$

As shown in **Figure 3.4(d)**, the band area ratio $I_{1416}/I_{1295+1305}$ increases with the electrospinning voltage, suggesting that the PE nanofibers produced at higher voltages have a larger volume fraction of the orthorhombic crystalline phase. The band area ratio displays a wide distribution for any given voltage, which is again because of the ‘whipping instability’ in the fiber deposition process. However, even with significant variations, the trend can still be clearly seen.

One more observation is that with higher electrospinning voltage, the factor-group split bands of the orthorhombic band (1440 cm^{-1} and 1460 cm^{-1}) decreases (**Figure 3.5**). In fact, at 52 kV, the 1416 cm^{-1} factor-group split band almost disappears. Lagaron et al. have observed that the presence of monoclinic or triclinic structures would influence the 1416 cm^{-1} factor-group splitting bands (Lagaron et al. 1999). They claimed that the spectral changes are due to not only the presence of the monoclinic phase but also the creation of an ill-defined orthorhombic crystalline structure with dislocations and disrupted crystals formed by the cold-drawing process, as a result of molecules being pulled through the crystals.

While we observed a clear dependence of the thermal conductivity on the electrospinning voltage, we did not find a relation between the thermal conductivity and diameter (**Figure 3.6(a)**). In the study of Zhong et al. (Zhong et al. 2014), the thermal conductivities of electrospun Nylon-

11 fibers prepared at relatively low voltages (6-7 kV) show a size dependence with higher thermal conductivities for smaller fibers, which is possibly due to better chain alignment in smaller fibers. One difference in their study is that their fibers span a large diameter range and all fibers are prepared with a relatively low and consistent electrospinning voltage, where the ‘whipping instability’ might not be as strong. In our case, however, the fibers are of relatively smaller diameters and fabricated at higher voltage range. The higher voltage leads to stronger ‘whipping instability’, and hence large variations in the actual electric field that the jet experiences during the fabrication process, which likely eliminate any dependence on the fiber diameter.

3.3.3 Temperature dependence of the thermal conductivity

In **Figure 3.6(b)**, we compare our thermal conductivity data with other published data for PE including a commercial high crystalline PE nanofiber (Dyneema and Spectra 900) and bulk thermal conductivity of PE (Wang et al. 2013). The selected electrospun fiber, fabricated at 45 kV, demonstrated a peak value of 9.3 W/m-K around 270 K, and then the thermal conductivity drops with temperature and reaches a value of 8.7 W/m-K at 320 K. The peak temperature is, however, much higher than that of the commercial high modulus PE fiber, which has a broad peak centering at ~100 K. The difference in the peak temperature suggests that the crystallinity level of the electrospun fiber is still lower than the Dyneema and Spectra 900 fiber, with abundant amorphous phases and strong inter-chain scattering at low temperatures. However, the anharmonicity in three-phonon scattering processes is strong enough to show its signature at a higher temperature.

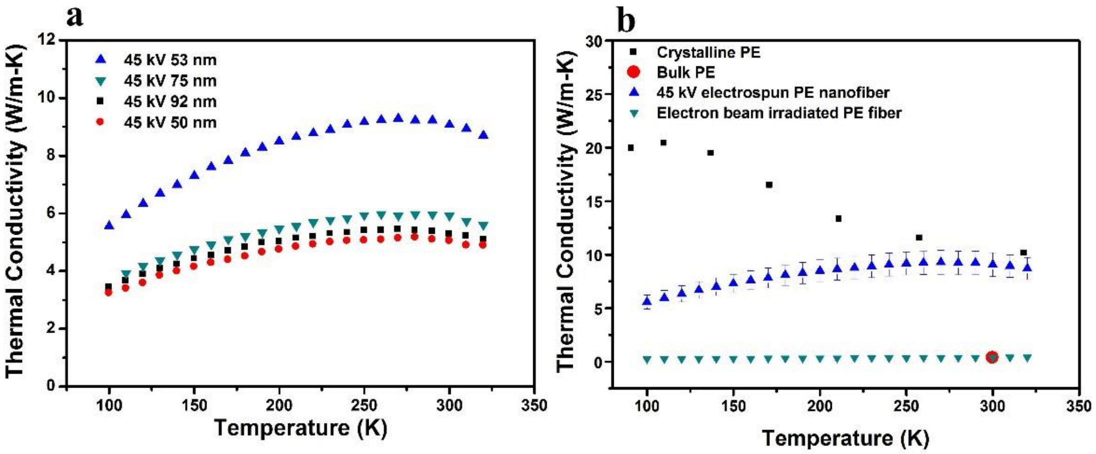

Figure 3.6 Thermal conductivity of PE nanofibers electrospun at 45 kV and comparison with others. (a) The thermal conductivity of four PE nanofibers of different diameter electrospun at the same voltage (45 kV). (b) Comparison of our thermal conductivity data with prior studies of PE (Wang et al. 2013).

3.3.4 Effects of electron beam irradiation

One interesting effect we found during the measurements is that annealing, caused by an electron beam, could drastically alter the nanofiber structure and its thermal conductivity. **Figure 3.7(c)** plots the thermal conductivity of the same fiber after it was exposed to the electron beam during SEM examination, which indicates that the thermal conductivity drops to that of bulk amorphous PE. There is no discernable peak in the measured thermal conductivity after the SEM, either.

To further clarify the electron beam annealing effects, we prepared additional samples and compared the measured thermal conductivity before and after SEM examination. We found that the electron beam could indeed lead to significant morphological change. **Figure 3.7(a)** and **3.7(b)** show the length of the same fiber sample prepared with a 45 kV electrospinning voltage at the beginning and the end of an SEM imaging process of ~1 min with an acceleration voltage of 5 kV, which indicates that the gap between the two suspended membranes shrinks from 6.6 μm to 5.8

μm. Note that this observation also suggests that the fiber adheres to the suspended membranes well and the interaction force is strong enough to prevent sliding of the fiber with respect to the membranes; instead, the fiber pulls the two membranes to each other. As to the thermal conductivity of the fiber prior to and after the SEM imaging, the value changes dramatically, dropping from a room temperature value of ~5 W/m-K to 0.4 W/m-K, as shown in **Figure 3.7(c)**. In order to accurately measure the diameter of the fiber, multiple micrographs were taken quickly to monitor the dimension change during the SEM imaging. We assume that the volume of the suspended segment does not change and the original diameter was calculated using the formula $d_{original} = \sqrt{d_{final}^2 \times l_{final} / l_{original}}$. Here $d_{original}$ and $l_{original}$ are the initial diameter and length of the fiber prior to the SEM imaging and d_{final} and l_{final} are the diameter and length of the fiber post the SEM imaging.

As mentioned before, larger 1130/1060 band intensity ratio for PE fibers deposited at higher voltages corresponds to better aligned molecular chains, and larger $I_{1416}/I_{1295+1305}$ band area ratio indicates a higher orthorhombic crystallinity level. **Figure 3.7(d)** shows the difference in Raman spectra of the same PE fiber prepared at 30 kV before and after the SEM imaging. Before the SEM operation, the 1130/1060 ratio was 1.87, while after the SEM process it dropped to 0.49, even smaller than the corresponding value of PE powder (1.16). In addition, prior to the SEM imaging, the intensity of the orthorhombic band at 1416 cm^{-1} was very strong but it almost disappeared after the SEM. All these data suggest that the focused electron beam remarkably altered the degree of orientation of the PE fiber and reduced the fraction of the orthorhombic crystallinity, leading to much lower thermal conductivity.

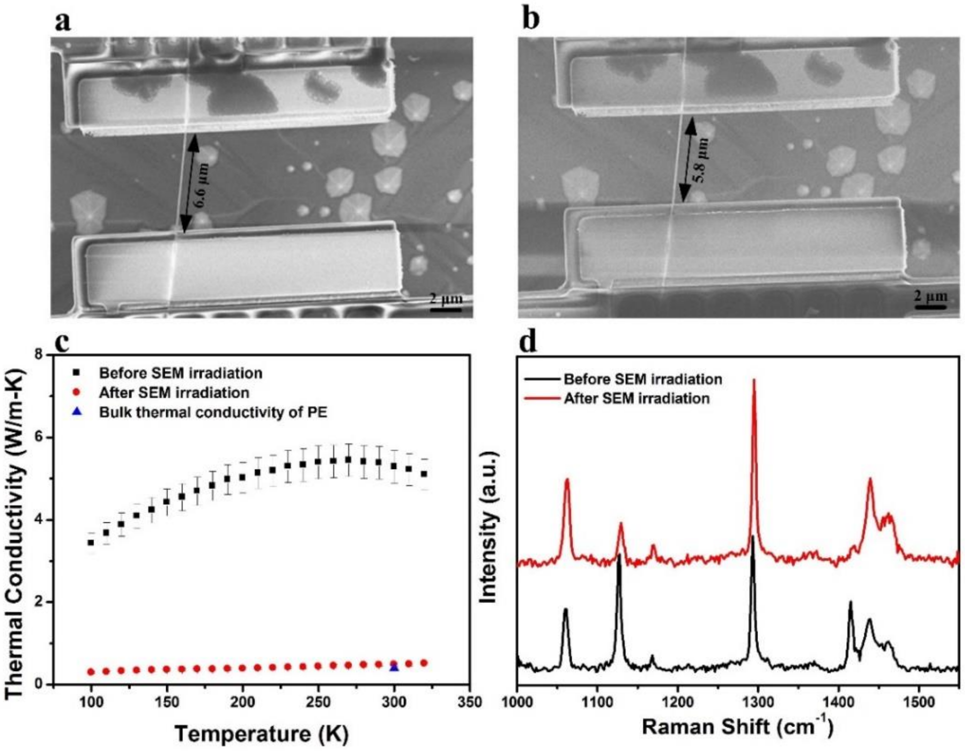

Figure 3.7 The effects of electron beam irradiation. (a) An SEM micrograph of the initial fiber. (b) An SEM micrograph of the irradiated fiber. It is clear that the length of the PE fiber has decreased after electron beam irradiation. (c) Thermal conductivity of an individual nanofiber before and after SEM characterization. The electron bombardment and associated temperature effects likely cause local microstructural alteration to the nanofiber, resulting in a reduction of thermal conductivity. (d) Micro-Raman spectra of the same PE nanofiber before and after SEM irradiation, its structure has been changed after the SEM irradiation. After the SEM irradiation, the intensity of the 1060 cm^{-1} and 1130 cm^{-1} bands switched and the orthorhombic band (1416 cm^{-1}) almost disappeared.

3.3.5 Trapped solvent during electrospinning

In the electrospinning process, we found that the solvent could be trapped inside the fiber at relatively high solution flow rates. **Figure 3.8(a)** shows the Raman spectra of PE nanofibers electrospun at various voltages with an 18 G needle and a 500 μl/min solution volume flow rate (Note that this is different from what we used for the preparation of fiber samples in thermal conductivity measurements, where conditions were tuned to minimize solvent residues in the fiber).

It can be seen that the Raman spectra of the PE nanofibers prepared with a low voltage have essentially the same peaks as those of the PE powder, while the intensity of the solvent peaks becomes stronger as the electrospinning voltage increases. This suggests that at higher voltage, the jet flies faster, leaving less time for the solvent to evaporate. Consequently, with increased electrospinning voltage, it becomes easier for solvent to be trapped inside the fiber. However, it was found that after storing the deposited fibers in a vacuum of 10^{-3} mbar overnight, the Raman peaks corresponding to the solvent disappeared, suggesting storing in vacuum could effectively remove the residual solvent (**Figure 3.8(b)**). This also guarantees that no complication from the solvent exists in our measurements because it is conducted under a much higher vacuum ($<2\times10^{-6}$ mbar).

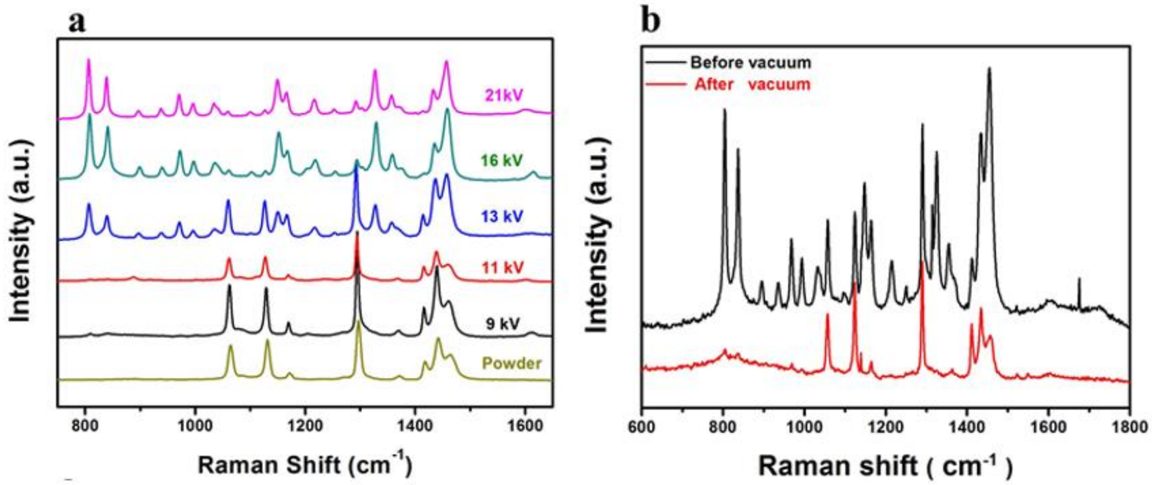

Figure 3.8 Raman spectra of PE nanofibers with solvent trapped inside. (a) Raman spectra of PE fibers electrospun at various voltages with 18 G needle and 500 μl/min solution flow rate. As the voltage increases, more solvent appears to be trapped in the fibers. (b) Raman spectra of a PE fiber before and after overnight storage under vacuum. It is clear that the peaks due to trapped solvent disappear after this overnight process.

3.3.6 Thermal conductivity of other electrospun polymer systems

Given the significant enhancement of thermal conductivity obtained for PE nanofibers, we attempted to measure the thermal conductivity of other polymer systems as well, such as nylon-6, PVDF and PEO nanofibers at an electrospinning voltage of 30 kV. Although no systematic fabrication and measurements were conducted yet, and only several samples went through careful characterization, all of the electrospun fibers show thermal conductivity enhancements as have been seen in electrospun PE nanofibers, an improvement attributed to the strong elongational force exercised during the electrospinning process, as shown in **Figure 3.9**. The results suggest the potential of applying electrospinning technique to other polymer systems to improve their thermal transport properties for practical applications.

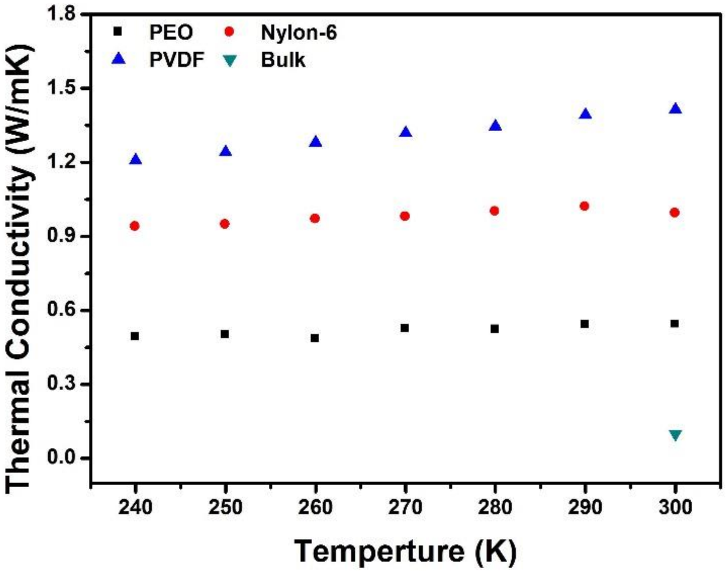

Figure 3.9 Thermal conductivity of PEO, Nylon-6, and PVDF electrospun nanofibers fabricated at 30 kV (Ma et al. 2015a). The bulk value is 0.2 W/m-K, which is approximately the same as that of the three polymers in comparison.

3.4 Post-deposition Mechanically Stretched PE Nanofibers

Compared to the highest thermal conductivity of 9.3 W/m-K we achieved with electrospun PE nanofibers, there have been reports on much higher value of 40 W/m-K (Kanamoto et al. 1988, Wang et al. 1991a) for ultradrawn PE microfibers/films achieved with a draw ratio up to ~500. More recently, Shen et al. using an AFM tip to apply an ultra-draw scheme and achieved a remarkable thermal conductivity of up to 104 W/m-K and an astonishing Young's modulus on the order of 300 GPa (Li et al. 2014, Shen et al. 2010). To explore whether post-deposition drawing can further enhance the thermal conductivity of PE nanofibers, we stretched the PDMS pieces on which the PE nanofibers were collected using a custom-built stage. The stage allows one to rotate a knob to control the stretch rate and speed. At this moment, this mechanical stretching was only performed at room temperature rather than in a temperature controlled environment.

Contrary to our expectation, the measured thermal conductivity is lower than the selected as-spun counterpart, shown in **Figure 3.10**. Although the variation could be partly attributed to the "whipping instability" during the electrospinning process, careful examination of the stretched fibers revealed that the stretching at room temperature introduced defects into the fibers.

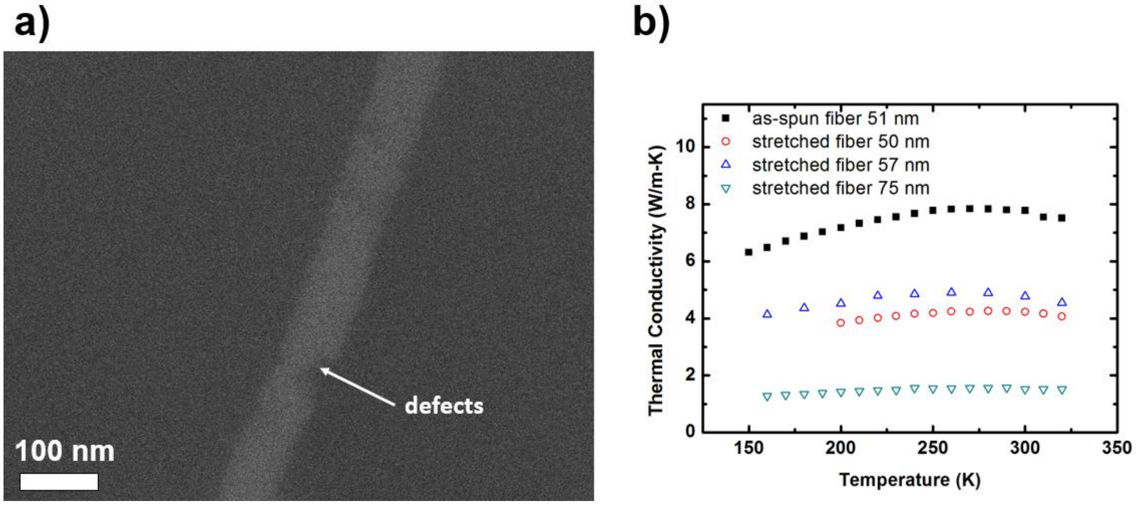

Figure 3.10 Mechanically stretched electrospun fibers fabricated at 50 kV. (a) A high magnification image showing the voids and defects created during the stretching process. (b) The thermal conductivity of three stretched PE nanofibers, fabricated at 50 kV compared to an as-spun fiber of similar dimension.

The decreased rather than enhanced thermal conductivity could arise from the following two reasons. First, in contrast to an elevated temperature environment typically applied during drawing process (Choy & Leung 1983, Choy et al. 1999), our current scheme is conducted at room temperature, which induce defects that reduce thermal conductivity. In addition, the stretch rate is not well controlled such that the molecular chains do not have adequate time to rearrange, leading to formation of defects and void. Naraghi et al. demonstrated that at high strain rate structural damage such as nanopores and deep surface ripples will form in the electrospun polyacrylonitrile nanofibers (Naraghi et al. 2007). These factors called for extra attention and an optimized stretching scheme to further optimize the structure of electrospun PE nanofibers.

3.5 Tip Drawn PE Nanofibers

In addition to electrospinning, we also tried a solution-drawing method to fabricate nanofibers with aligned molecular orientation (Nain et al. 2006). The fabrication process is illustrated in **Figure 3.11**, in which we first dissolved high molecular weight PE powder (molecular weight $3{\sim}6\times10^6$) in p-xylene solvent (all materials from Sigma-Aldrich, Inc.). The boiling temperature of P-xylene solvent is about 411 K while the dissolution temperature for PE powder is about 393 K. The PE solution was stirred at 393 K for an hour until the powder completely dissolved and the temperature was kept around 393 K during the nanofiber drawing process. A 28 G metal syringe needle was inserted into the PE solution and drew out from the solution quickly. During the drawing process, the solvent evaporated and a PE nanofiber extended between the needle tip and the solution. The fibers were transferred to a piece of PDMS for following transfer. During the drawing process, it is likely that the molecular chains get aligned and result in nanofibers with ordered molecular chains.

Following the same scheme as the sample preparation process for electrospun nanofibers, the solution-drawn nanofibers were cut and transferred for thermal conductivity measurements. The measured thermal conductivity is shown in **Figure 3.12** and the highest attained value from a 40 nm PE nanofiber is 9 W/m-K at 260 K. The thermal conductivity for selected fibers peaked at 260~290 K, and then start to drop when temperature further increases. The trend is the same as that of electrospun fibers, suggesting that this simple fabrication technique could achieve a similar level of molecular chain alignment and enhanced crystallinity as the electrospinning technique.

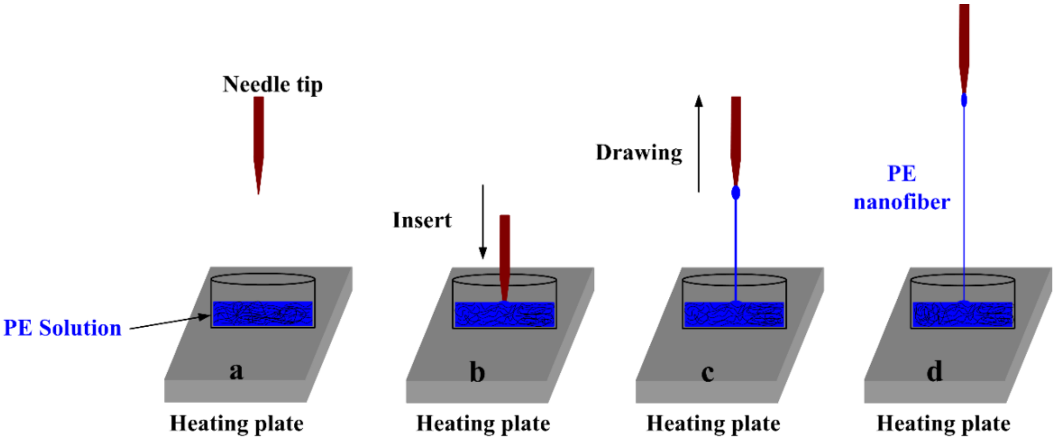

Figure 3.11 Schematic diagram showing the steps of using solution drawing method to prepare PE nanofibers. (a) The PE powder is dissolved in P-xylene solvent. (b) A syringe needle is inserted in the PE solution. (c) The needle is drawn out from the solution. (d) A PE nanofiber is extended between the tip of the needle and the solution.

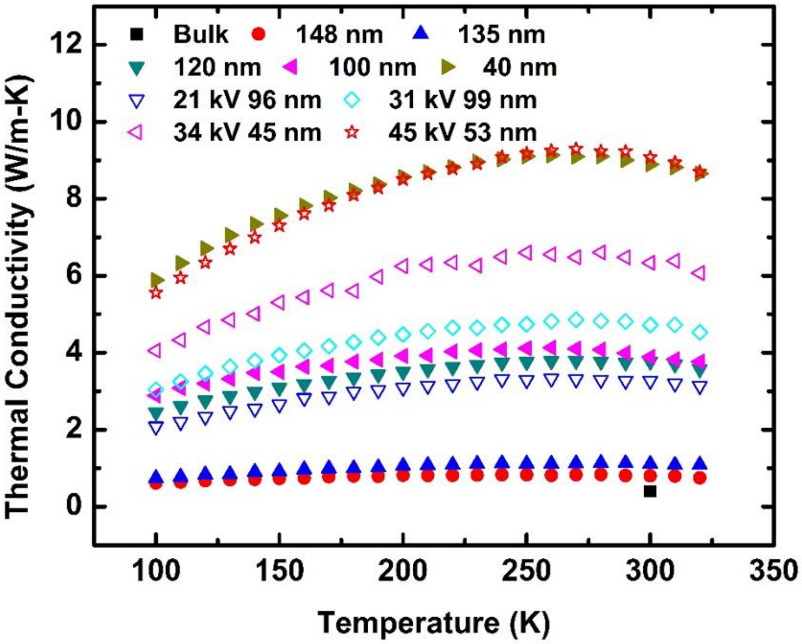

Figure 3.12 Measured thermal conductivity of the PE nanofibers prepared with solution-drawing in comparison to electrospun nanofibers (Hollow symbols). The highest thermal conductivity of the solution-drawn PE nanofiber is comparable to that of the electrospun PE nanofiber fabricated at 45 kV. The voltages and the diameters in the label indicate the electrospinning fabrication condition and the corresponding dimension for the electrospun fibers (Ma et al. 2016).

3.6 Summary

In this chapter, we explore the relation among the electrospinning voltage, resulted nanofiber structure, and the corresponding thermal conductivity. Results show that electrospun PE nanofibers exhibit thermal conductivities that can be significantly higher than corresponding bulk values (~0.4 W/m-K), with the highest value obtained as 9.3 W/m-K. This thermal conductivity enhancement is due to the higher degree of molecular orientation and enhanced level of crystallinity, as evidenced by the micro-Raman spectroscopy characterization. A general trend of higher thermal conductivity with larger electrospinning voltage was observed; however, it is also found that the thermal conductivity for fibers prepared with the same voltage could vary significantly, due to the ‘whipping instability’ in the electrospinning process. Due to the limitations of our current instrumentation, the maximum electrospinning voltage achieved was 52 kV. With an electrospinning system that can operate at higher voltages, we believe the thermal conductivity may be further enhanced. Given that electrospinning is a quick and low cost method to produce nanofibers with enhanced thermal conductivity, this study points to the potential of using electrospun polymer nanofibers as materials with good thermal transport properties. A quick and efficient tip drawing method, free of high voltages used in electrospinning was developed and implemented to achieve similar level of thermal conductivity enhancement, which was also due to the enhanced crystallinity and more ordered molecular chains.

4. Thermal Conductivity of Individual Boron Carbide Nanowires

Boron carbides, a class of ceramic materials with complex atomic structures and a wide range of carbon concentrations (Domnich et al. 2011), have been extensively used as abrasives, armour components, and neutron capture materials (Caruso et al. 2006). One promising application of boron carbides is for high-temperature thermoelectric power generation, owing to their chemical stability and desirable figures-of-merit (Bouchacourt & Thevenot 1985). However, because of the enormous challenges associated with synthesizing high quality single-crystalline boron carbides, almost all bulk samples are prepared by melting or hot-pressing, leading to polycrystalline samples with non-uniform grain sizes and numerous defects (Gunjishima et al. 2001, Werheit et al. 2004). As such, the measured properties are quite scattered, yielding limited understanding of the underlying transport physics (Nishi et al. 2002).

Through extensive measurements of more than fifty single-crystalline boron carbide nanowires, we show how carbon concentration, diameter, and planar defects modulate the wire thermal conductivity. In particular, nanowires with defect-free and defective kinks show interesting kink effects on thermal transport. Given the recent success of synthesizing kinked nanowires in a controlled manner (Chen et al. 2017, Pevzner et al. 2012, Tian et al. 2009), the observation of pronounced kink thermal resistance and interesting effects of defects in the kink provide novel mechanisms for tuning the thermal conductivity of nanostructures.

One important feature of boron carbides is their low stacking fault energy (75 mJ/m^2) (Ashbee 1971), which can easily lead to planar faults. Such faults have been commonly observed in bulk boron carbides, regardless of the synthesis method (Balakrishnarajan et al. 2007). The effects of stacking faults, including twin planes, on transport properties have been a topic of interest recently

(Takemoto et al. 2014, Wan et al. 2012, Zhan et al. 2014). However, compared with the extensive studies of how stacking faults affect electrical transport, their effects on thermal transport are not well explored. Such information is, however, extremely valuable for engineering low thermal conductivity materials.

Boron carbide nanowires were synthesized in an low pressure chemical vapor deposition (LPCVD) system as described previously (Guan et al. 2012). Individual boron carbide nanowires were then picked up with the help of an in-house built micromanipulator described in chapter 2 and transferred to a copper grid for TEM studies (Guan et al. 2014). The TEM characterization indicates both transverse stacking faults (TFs) and axial stacking faults (AFs) inside these nanowires.

In this chapter, we discuss experimental characterization of the structure and thermal conductivity of single crystalline boron carbide nanowires with different structures and compositions. Detailed structural and compositional characterizations were performed on each sample. The effects of different parameters, including diameter, carbon concentration, and especially twin planes and kinks are explored, which present a comprehensive picture of how these factors affect thermal transport in boron carbide nanowires and provide important physical insights into tuning the thermal transport properties of nanowires.

4.1 Structure and Properties of Bulk Boron Carbides

The boron carbides investigated in this chapter have a common rhombohedral lattice with eight twelve-atom icosahedra located at the corners and a three-atom chain along the longest body diagonal within the rhombohedron. These boron carbides are referred as B_4C-type. Its typical lattice is illustrated in **Figure 4.1**, where blue and red spheres represent boron (B) and carbon (C) atoms, respectively. In this example, the icosahedron is made of twelve boron atoms (i.e., the so-called B_{12} icosahedron) and the three-atom chain is consisted of C-B-C (Emin 1988, Werheit & Kuhlmann 2011). Each icosahedron is connected with six other icosahedra through direct covalent bonds. The three-atom chain occupies the inter-icosahedral spaces along the longest diagonal direction and the atoms at the end of the chain form direct bonds with three icosahedra (Domnich et al. 2011).

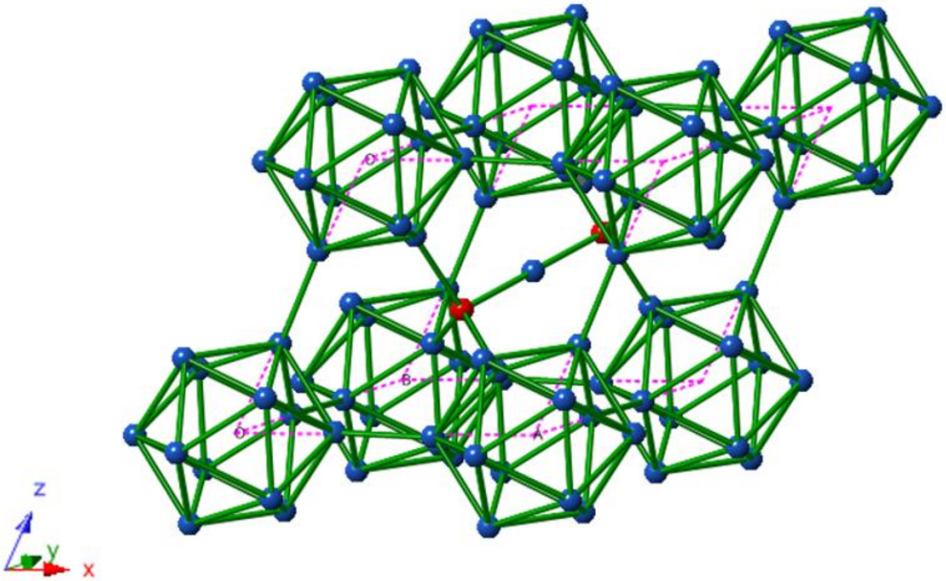

Figure 4.1 The common primitive rhombohedral lattice of boron carbide. Within the unit cell, eight icosahedra take the eight corners, with a three-atom chain along the longest body diagonal (Emin 1988, Werheit & Kuhlmann 2011). Blue and red spheres represent boron and carbon atoms, respectively.

Although all B_4C-type boron carbides share the above common rhombohedral lattice, the carbon concentration can vary significantly among different crystals. Thus, boron carbides are considered as compositional-disordered materials. Their carbon concentrations vary from 8.8 at. %C in $B_{\sim 10.4}C$ (i.e., boron-rich end) to 18.8 at. %C in $B_{\sim 4.3}C$ (i.e., carbon-rich end) (Werheit & Shalamberidze 2012). For boron carbides with lower carbon concentrations (< 13.3 at. %), the

$B_{11}C$ icosahedra and C-B-B (or sometimes B-☐-B, where ☐ represents a vacancy) three-atom chains exist (Werheit & Shalamberidze 2012). As carbon concentration increases, the carbon atoms progressively replace the boron atoms in the lattice. The replacements could happen in the polar sites of the icosahedra and the three-atom chain (An et al. 2014). For example, the $B_{11}C$ icosahedra would become B_{12}, and the C-B-B three-atom chain would take C-B-C structure. The large variation of carbon concentration within the homogeneity range leads to the presence of highly concentrated intrinsic structural defects in boron carbides. Such defects, in the form of incomplete occupation of specific sites or of antisite defects, could greatly influence relevant transport properties (Schmechel & Werheit 1999, Werheit 2009). It has also been shown that as the carbon concentration increases, these structural defects can reduce (Emin 1988, Tallant et al. 1989).

Transport properties, including electrical and thermal conductivities and Seebeck coefficient of bulk boron carbides, have been studied (Aselage et al. 1993, 2001; Emin 2006, Wood et al. 1985). So far, research has been focused on electrical conductivity to understand the charge transport mechanism, whereas studies on thermal properties are limited. Most of transport property measurements were performed on polycrystalline specimens prepared by melting or hot-pressing (Cai et al. 1999, Liu 2001). The variation of carbon content between grains and the existence of grain boundaries/impurities/other defects led to inevitable discrepancies among experimental results, rendering correlation between experimental data and theoretical predictions difficult.

Contradictory to the theoretically predicted metallic nature, experimental measurements revealed that boron carbides are semiconductors with the electrical conductivity increasing with temperature (**Figure 4.2(a)**). To explain this unexpected electrical character, there are two main models of charge transport proposed: the bipolaron model by Emin (Aselage et al. 2001) and the defects-based model by Werheit (Schmechel & Werheit 2000). Emin hypothesizes that high density bipolarons promoted by high electron deficiencies in the valence bands of idealized boron carbide (B_4C=$B_{11}C$(C-B-C)) are responsible for electrical transport in boron carbides (Howard et al. 1987). However, Werheit formulates his theory on the fact that there are well defined defects in the form of incomplete occupations of specific sites or of antisite defects in boron-rich solids (Schmechel & Werheit 1999, Werheit 2009). Based on a band structure constructed from optical spectroscopy and electrical conductivity measurements, he proposes that high density intrinsic structural defects can compensate the calculated valence electron deficiency by generating dislocated valence states in the band gap. The charge transport is due to hopping processes that happen within these partially filled gap states, superimposed by a certain contribution from free holes. More experimental data from well-characterized single-crystalline samples will help to clarify the charge transport mechanisms in boron carbides.

The reported Seebeck coefficients of boron carbides are very large, as high as 300 μV/K (**Figure 4.2(b)**) (Aselage et al. 2001, Emin 1998). However, the dependence of Seebeck coefficient on planar defects, carbon concentration, and temperature is not clear yet. For example, Aselage et al. suggested that planar defects such as twin boundaries could enhance the Seebeck coefficient of boron carbides (Aselage et al. 1987). This is based on their observation that the obtained Seebeck coefficient from defect-free boron carbides was only 10-20 μV/K, whereas that of the hot-pressed boron carbides with extensive twins was in the range of 100-200 μV/K. On the contrary, Gunjishima et al. reported that the Seebeck coefficients of defect-free single crystalline boron carbides prepared with a floating zone method was 240-260 μV/K (Gunjishima et al. 2001). Therefore, it remained unclear whether planar defects can affect the Seebeck coefficient of boron carbides or not.

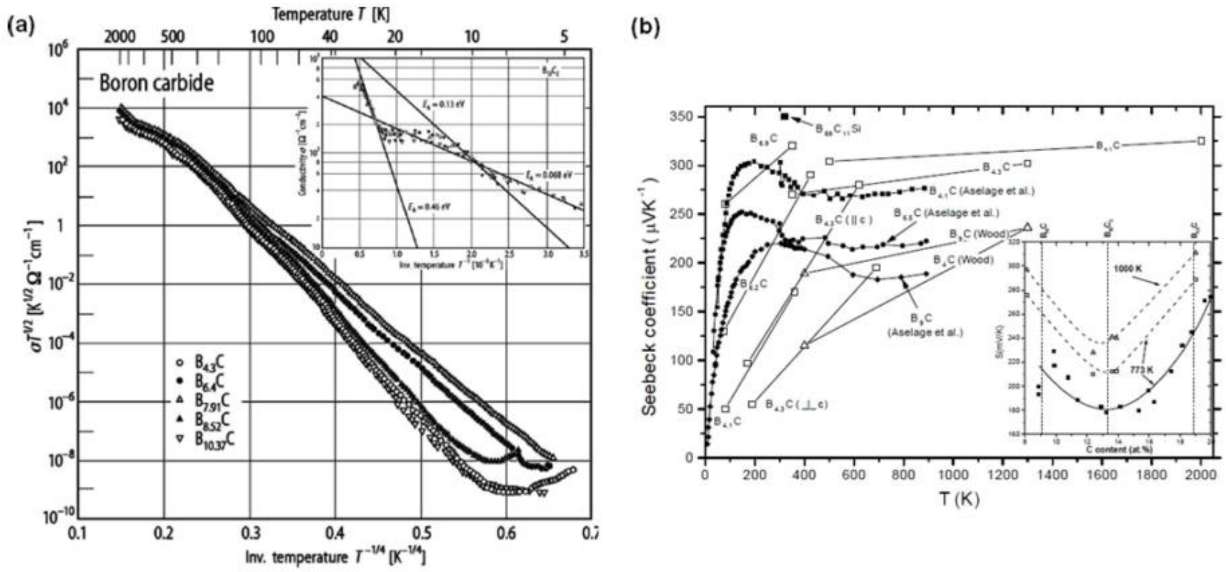

Figure 4.2 (a) Electrical conductivity of some boron carbides. The electrical conductivity increases with temperature, indicating the semiconducting nature of boron carbides. (b) Seebeck coefficient of some boron carbides. Both electrical conductivity and Seebeck coefficients are dependent on carbon content (Werheit 2006).

4.2 Growth of Straight and Kinked Boron Carbide Nanowires

The crystal structure of boron carbides can be viewed as a rhombohedral distortion of the cubic close packing (ccp) of icosahedra. The {001} planes of the rhombohedral cell are considered as the close-packed planes in the ccp arrangement. Taking the (001) plane as an example, it should be stacked in a …ABCABC… sequence to form a crystal. If this normal stacking sequence is disturbed, planar defects such as stacking faults and twin boundaries would form. Due to the low stacking fault energy (75 mJ/m^2) (Ashbee 1971), planar defects are commonly observed in bulk boron carbides and boron carbide nanostructures (Anselmi-Tamburini et al. 2005, Mackinnon et al. 1986). For our as-synthesized boron carbide nanowires, two types of straight nanowires are identified based on the geometric relation between the preferred growth direction of a nanowire and planar defects (Guan et al. 2012, 2014). They are transverse faults (TF) nanowires with the preferred growth direction normal to planar defects, and axial faults (AF) nanowires with the preferred growth direction parallel with planar defects. The stacking fault density can be accurately determined for AF nanowires. **Figure 4.3(a&b)** show typical HRTEM images and diffraction patterns for TF and AF nanowires. **Figure 4.3(e)** illustrates the preferred growth directions of TF and AF nanowires in a rhombohedral unit cell of boron carbides, which are determined to be $[\overline{0.292}\ \overline{0.292}\ 1]$ and [100], respectively, according to the crystallographic characteristics (Guan et al. 2014).

Boron carbide nanowires were grown following the vapor-liquid-solid (VLS) mechanism (Guan et al. 2012), in which a single nucleation event per layer initiates at the nanowire-catalyst interface. The nature (i.e., composition, crystal structure, and shape) of the catalyst determines whether TF or AF nanowires will be formed. Our studies showed that the catalysts on TF nanowires are generally semi-circle and the catalyst-nanowire interface is flat, indicating the layer-by-layer epitaxy growth. We believe that the formation of transverse faults is due to (1) the shape variation of catalysts caused by perturbations of temperature and pressure during synthesis (as illustrated in the inset of the left panel of **Figure 4.4**), and (2) the low stacking fault energy of boron carbides.

The synthesis also gave rise to formation of kinked boron carbide nanowires. During the growth of kinked nanowires, the catalyst migrates and plays more important roles. **Figure 4.4** illustrates how a kinked nanowire with two TF segments (i.e., kinked TF-TF nanowire) is formed. During the first stage (Stage 1), a TF segment is grown as described above. Then during the second stage (Stage 2), due to some large perturbations, the catalyst starts to migrate, gradually wets the right side of the nanowire, and leads to the turn of the nanowire. During the final stage (Stage 3), after the catalyst is fully migrated to another facet, the normal layer-by-layer epitaxy growth resumes and leads to another TF straight segment. As illustrated in **Figure 4.4**, the kink region is defect-free, which is observed for majority of kinked TF-TF nanowires we studied.

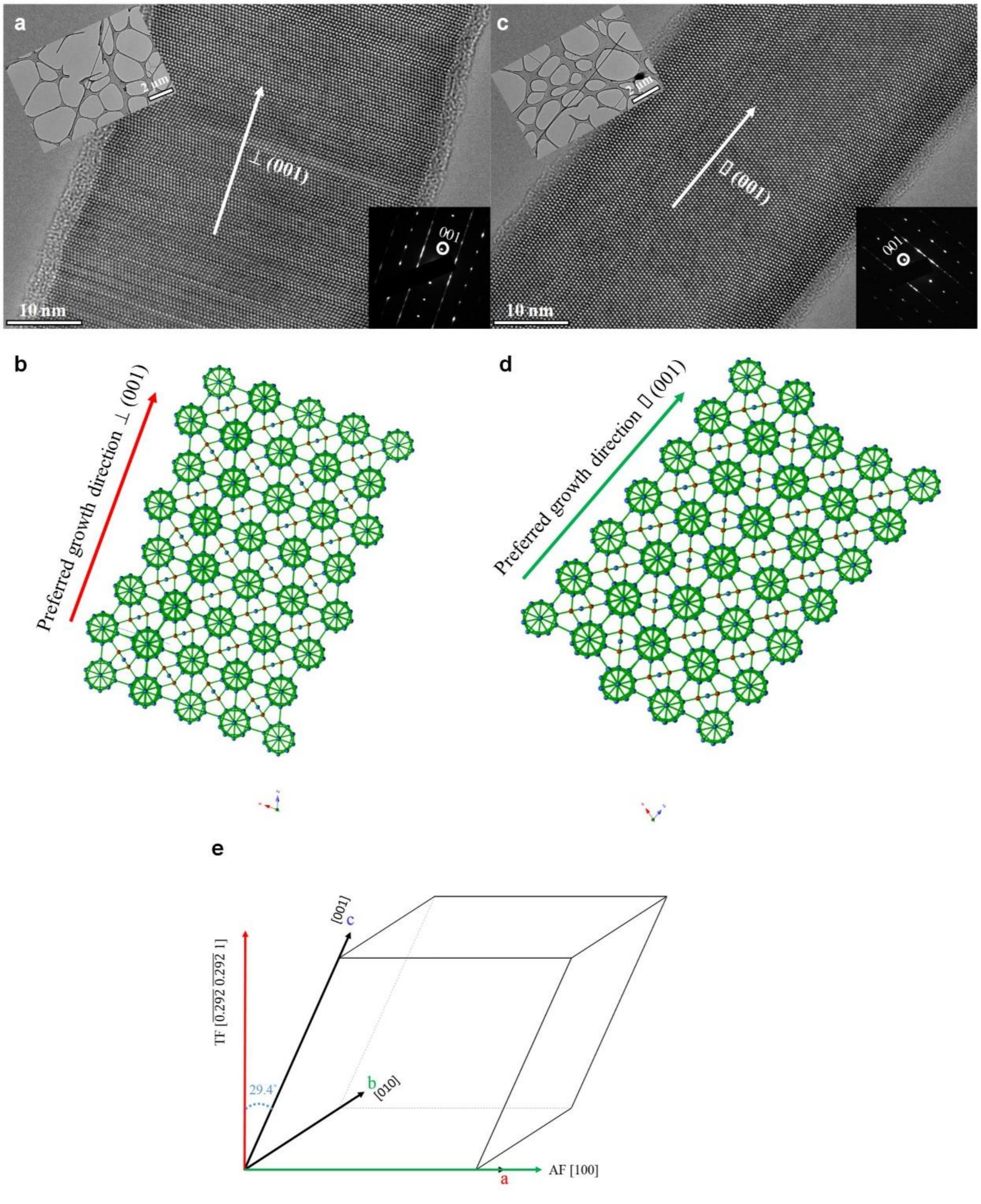

Figure 4.3 Growth of straight boron carbide nanowires. (a-d) HRTEM images and simulated models showing the preferred growth direction of a nanowire is either perpendicular to or parallel with the fault plane (001) for TF (a&c) and AF (b&d) boron carbide nanowires. The TEM image of the whole nanowire and the diffraction pattern are presented in the inset of a&b; (e) Illustration

of a boron carbide rhombohedral unit cell with the preferred growth directions of TF (red arrow, [ ]) and AF (green arrow, [100]) nanowires indicated.

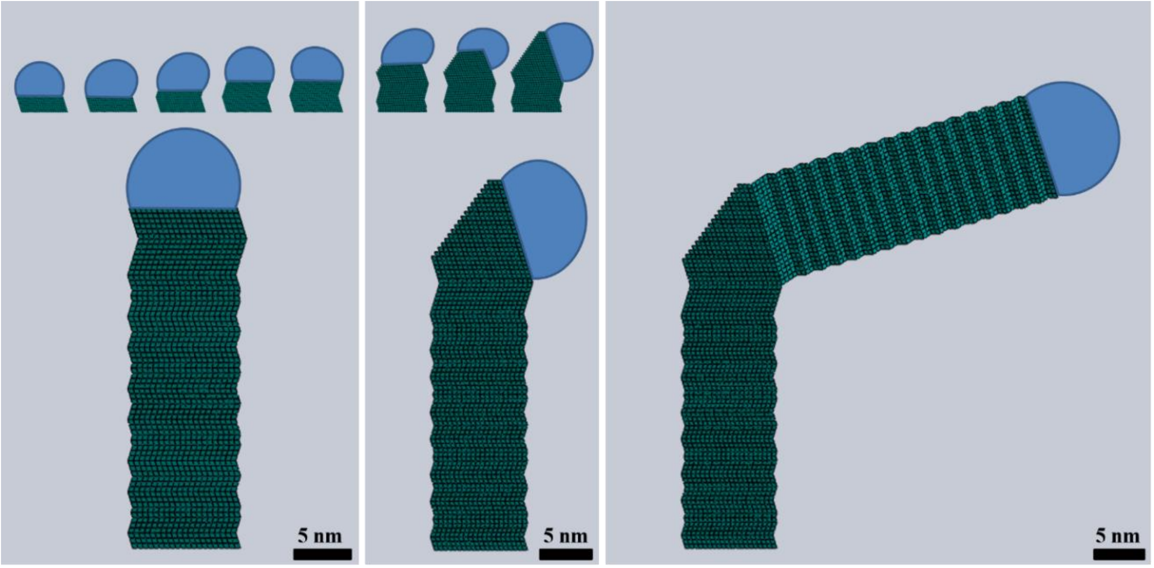

Stage 1 Stage 2 Stage 3

Figure 4.4 Growth of the kink. Illustration of the growth of a kinked TF-TF boron carbide nanowire in three stages.

Occasionally, for some kinked TF-TF nanowires, low density of defects was observed in the kink region. A typical example is shown in **Figure 4.5**. For this kinked TF-TF nanowire, the HRTEM image shows the stacking faults (indicated by the green line in the blue dashed line box) and dislocations (within the bright yellow circle) in the kink region. A comparison of the Fourier power spectra obtained from the defect-free area (red dashed line box) and defective area (blue dashed line box) further confirms the localized existence of stacking faults. As clearly seen from the diffraction pattern in the red solid box, the diffraction spots are well separated and distinctive, while streak lines are shown in the diffraction pattern in the blue solid line box. These defects in kink would lead to enhanced phonon scattering.

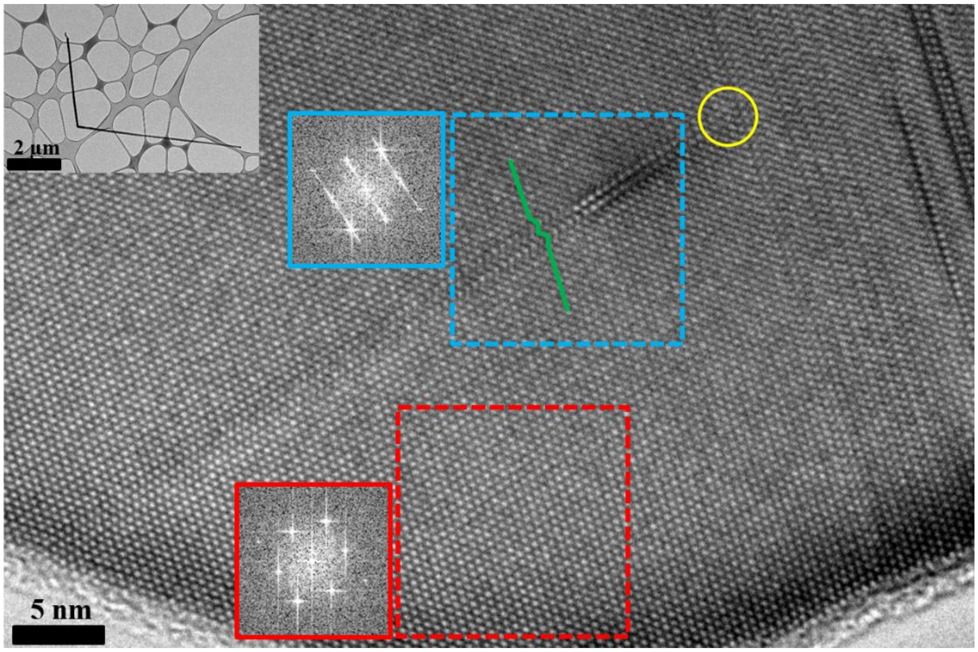

Figure 4.5 Microstructure of the kink region of a kinked TF-TF nanowire. An HRTEM image of the kink shows the existence of stacking faults (indicated by the green line) and dislocations (within the bright yellow circle). The Fourier power spectra of the defective region and the defect-free region are highlighted in the blue and red solid line squares.

4.3 Thermal Conductivity of Straight Boron Carbide Nanowires

For all measured nanowires, the contacts between the nanowire and the suspended membranes were treated with EBID of Pt to minimize the contact thermal resistance, as shown in the inset of **Figure 4.6**. Since boron carbides have significant Seebeck effects (Werheit et al. 2009), we have verified that the Pt deposition could reduce the contact thermal resistance to a negligible level through measuring the Seebeck coefficients from different sets of electrodes (Mavrokefalos et al. 2007). This method essentially uses the nanowire as a differential thermocouple to determine the temperature drops at the contacts. The Seebeck voltages were measured between both the two inner electrodes (2&3) and the two outer electrodes (1&4), which would otherwise share different temperatures if the contact thermal resistance was not reduced to a negligible level. **Figure 4.6** clearly shows that the Seebeck coefficients measured from the two sets of electrodes overlap with each other, suggesting negligible contact thermal resistance.

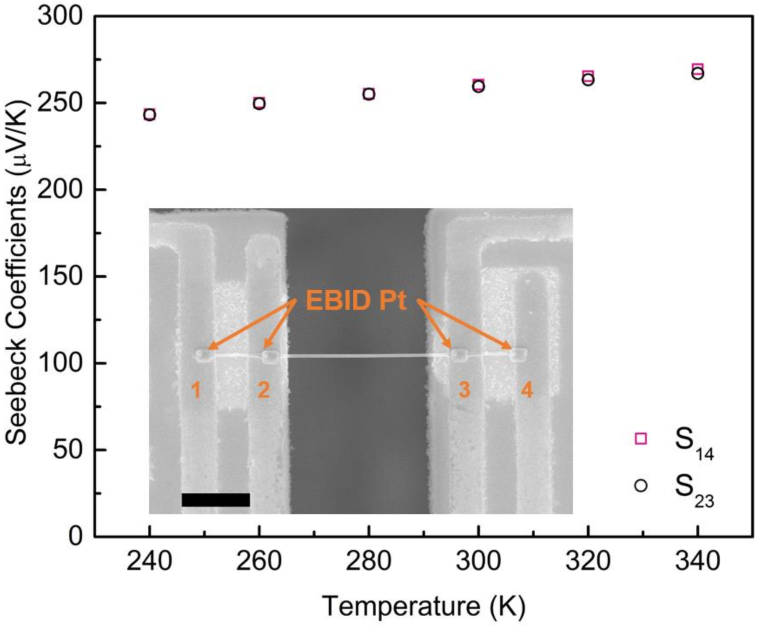

Figure 4.6 Contact thermal resistance characterization. The inset is an SEM image showing a straight boron carbide nanowire bridging the two suspended side-by-side membranes with all four contacts bonded with EBID Pt deposits. The scale bar in the inset is 2 μm.

4.3.1 Straight Boron Carbide Nanowires

Since our boron carbide nanowires have complex structure and compositions, we first confirm that for nanowires of the same structure and composition, the measured thermal conductivities are identical. **Figure 4.7** plots the thermal conductivity of three straight wires all of ~50 nm diameter, ~14% carbon and with TFs. The data for these three wires essentially overlap with each other, indicating that the parameters considered include all major factors important for thermal transport in these nanowires.

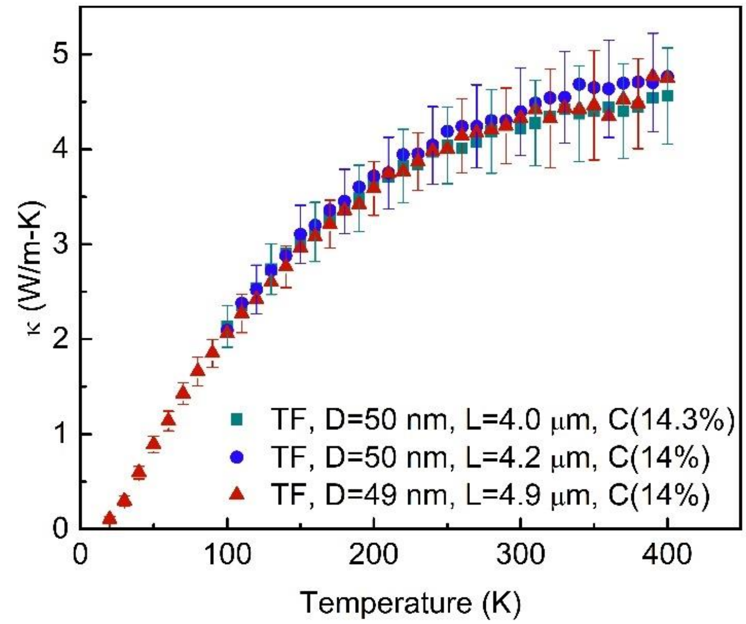

Figure 4.7 Thermal conductivity of three different TF boron carbide nanowires that share similar diameter (~50 nm) and carbon concentration (~14%).

Next, we examine the effects of carbon concentration, wire diameter, and stacking fault orientation on thermal transport in these nanowires. **Figure 4.8** plots the room temperature (300 K) thermal conductivity values of twenty-one straight boron carbide nanowires, of both axial and transverse stacking faults, versus the carbon concentration and wire diameter. It can be clearly seen that there exists a general trend of higher thermal conductivity for nanowires of higher carbon concentration and larger diameter.

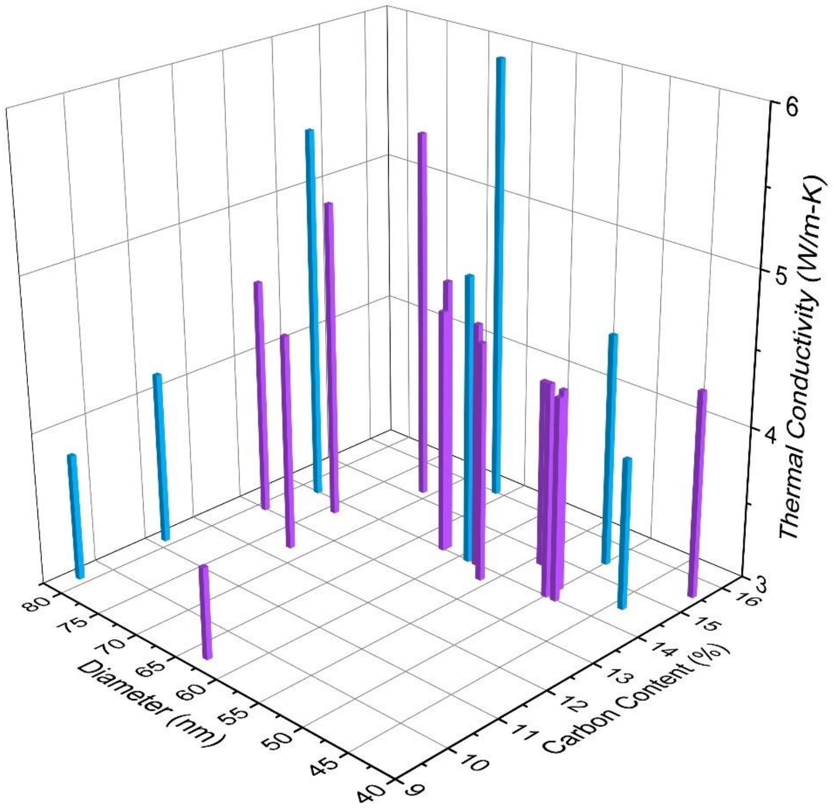

Figure 4.8 3D bar graph of the room temperature thermal conductivity of twenty-one straight boron carbide nanowires, including both AF (cyan) and TF (purple) ones, plotted against diameter and carbon concentration.

Even though the available data are quite scattered, the thermal conductivity of bulk polycrystalline boron carbides shows a general trend of enhanced value as the carbon concentration increases (Medwick et al. 1994, Wood et al. 1985). This trend is clear for both measured single crystalline nanowires with AFs and TFs, as shown in **Figure 4.8 and 4.9**. In **Figure 4.9 (a)&(b)**, two sets of nanowires with AFs and TFs, respectively, are shown versus their carbon concentrations. Note that the diameters of these nanowires are not similar to each other, but the strategy we select these subsets of samples is that nanowires with higher concentrations have diameters similar to or smaller than those with lower carbon concentrations. This way, any effects from phonon-boundary scattering at the nanowire surface will only counter the trend of carbon concentration. As such, the actual thermal conductivity increase with ascending carbon concentration should only be larger.

The dependence of boron carbide thermal conductivity on carbon concentration has been attributed to the more ordered molecular structure and reduced structural defects as the carbon concentration increases (Emin et al. 1987, Medwick et al. 1994, Wood et al. 1985). Boron carbides have a rhombohedral lattice with eight 12-atom icosahedra locate at the corners and one 3-atom chain occupies the longest diagonal of the rhombohedron. The carbon atoms can replace one boron atom in the icosahedra or reside on the 3-atom chain. The three-atom chains, mostly consisting of C-B-C at high carbon concentration, are generally stronger than the intra-icosahedral bonding (Xie et al. 2016), and thus, facilitate thermal transport. Additionally, these three-atom chains tend to be more ordered (Suri et al. 2010), which favors thermal transport as well. In contrast, for boron carbides with low carbon concentrations, the three-atom chains can be replaced with weaker/less ordered bonding such as C-B-B or B-☐-B (Emin et al. 1987). The uncertainty of these replacements results in the formation of local disorders, which lower the thermal conductivity. As such, the more ordered crystalline structure and reduced structural defects with increasing carbon contents are responsible for the enhanced thermal transport properties since the dominant energy carriers, phonons, are very sensitive to the quality of the crystalline structure.

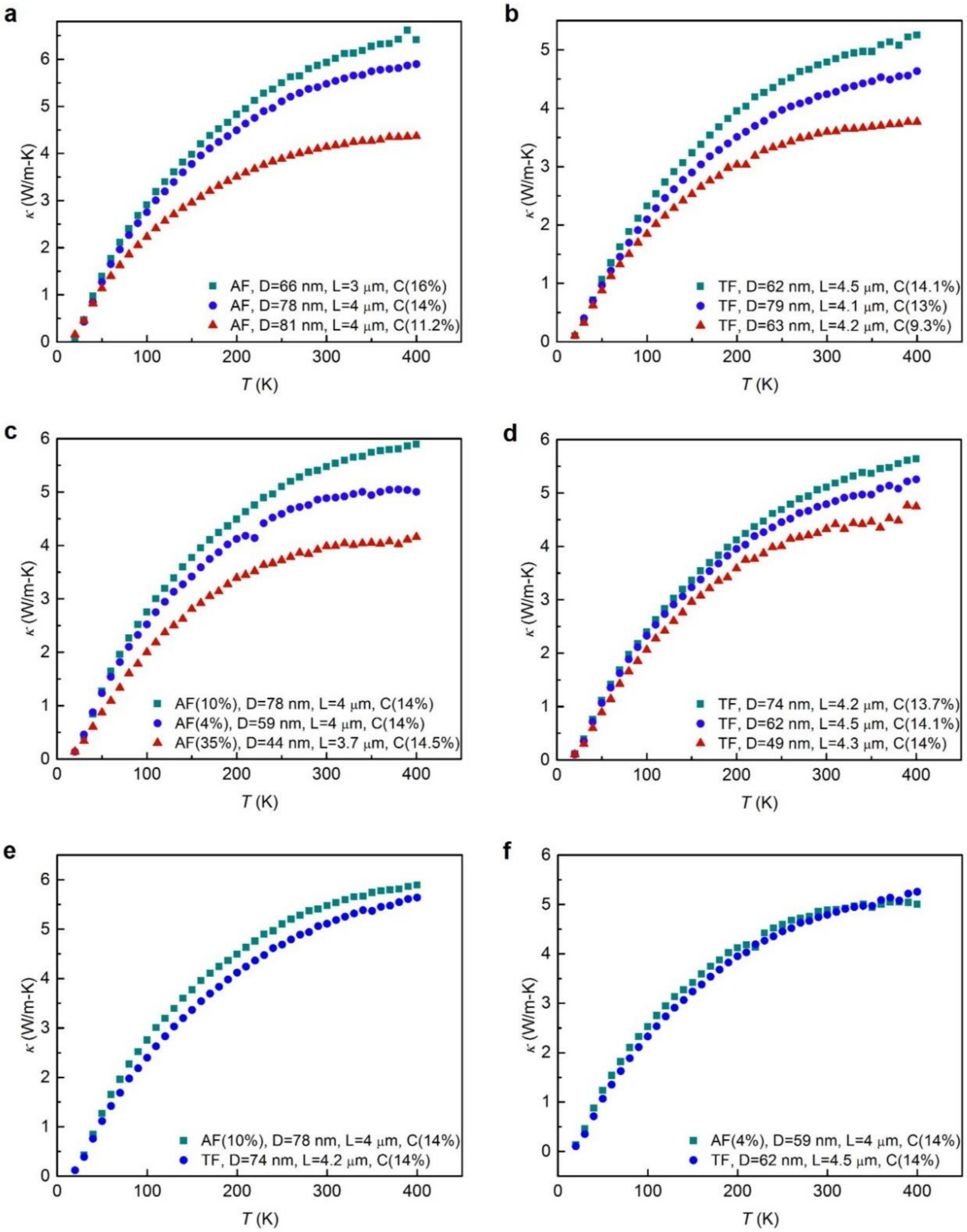

Figure 4.9 The effects of carbon concentration, nanowire diameter, and stacking fault orientation/density on the thermal conductivity of boron carbide nanowires. Carbon concentration dependence for nanowires of both (a) AFs and (b) TFs in the temperature range from 20 to 400 K. Diameter dependence in nanowires of (c) AFs and (d) TFs in the temperature range between 20 and 400 K. (e-f) Comparison of the thermal conductivity between two groups of AF and TF nanowires of similar carbon concentration and diameter.

For nanowires of similar carbon concentrations, the thermal conductivity is higher for larger diameter wire, as can be seen from **Figure 4.8** and more data in **Figure 4.9(c&d)** for the thermal conductivity over the whole measurement temperature range. This observation suggests that phonon-boundary scattering also plays an important role in determining the thermal conductivity of these nanowires. Enhanced boundary scattering in smaller diameter wires helps to reduce the effective phonon mean free path, which leads to suppressed thermal conductivity.

In contrast to carbon concentration and wire diameter, no strong dependence of the wire thermal conductivity on staking fault orientation and/or density can be observed. In fact, a 78 nm AF wire has a higher fault density (10%) than a 59 nm AF wire (4%), yet the thermal conductivity of the larger wire is higher (**Figure 4.9(c)**), which suggests that planar defects do not play a major role in determining the thermal conductivity. In addition, AF and TF nanowires of similar carbon concentration and diameter have approximately the same thermal conductivity (**Figure 4.9(e&f)**), indicating a marginal effect of the fault orientation. These observations are consistent with the report (Porter et al. 2016) that while there could be a big difference between silicon nanowires with and without planar defects, the thermal conductivity reduction becomes marginal as fault density increases beyond 0.088 nm^{-1}. For our wires, the fault density ranges from 0.087 nm^{-1} to 0.982 nm^{-1}, so it is reasonable that no strong dependence on the fault density is observed. In fact, since the average distance between neighboring defects is only a few nanometers, if the defects are important for the phonons that are responsible for thermal transport in these nanowires, the effective phonon mean free path should only be a few of nanometers and no clear diameter dependence should be observed.

If we regard the planar stacking fault as an interface with both sides of the same material, then the more significant effects of surface boundary can be explained as discussed in a recent opinion paper (Li & McGaughey 2015). At nanowire surface, all phonons will be scattered or reflected and this process is nearly diffuse, while at the stacking faults, a large portion of phonons will be transmitted specularly, which does not pose resistance to thermal transport. Another fact is that the highest measured temperature is 400 K in this report, far smaller than the Debye temperature for boron carbides (~1467 K for $B_{13}C_2$) (Medwick et al. 1994), which means that high frequency phonon bands are still not well populated. The dominant heat carriers in the studied temperature range are still lower frequency acoustic phonon modes, and these phonons are not vulnerable to disturbance incurred by the stacking faults.

It is worth noting that stacking faults have been widely thought to be able to reduce thermal conductivity significantly, which has been demonstrated in various materials systems (Shin et al. 2014, Takemoto et al. 2014, Thompson et al. 2016, Wan et al. 2012). For example, Wan et al. (Wan et al. 2012) have shown that nanoscale stacking faults could induce lower thermal conductivity in metal sulfides superlattices; and Takemoto et al. (Takemoto et al. 2014) have demonstrated that introducing stacking faults in ZnO can lead to reduced thermal conductivity for better thermoelectric performance. Interestingly, Zhan et al. (Zhan et al. 2014) found that while various types of stacking faults could significantly reduce the thermal conductivity of silicon nanowires, their results also indicated that increasing the stacking fault density only led to marginal drop in the derived thermal conductivity.

4.3.2 Kinked Boron Carbide Nanowires

With a good understanding of the effects of carbon concentration, wire diameter, and stacking fault for straight boron carbide nanowires, next, we examine the effects of kinks on thermal transport in these nanowires. The total suspended lengths of all nanowires are around 4 µm, ranging from 3.1 μm to 4.8 μm. **Figure 4.10** plots four groups of data that all show significantly reduced thermal conductivity for kinked nanowires, which are 15-36% lower at room temperature for different pairs of samples. This level of thermal conductivity reduction corresponds to a remarkable kink resistance. In fact, the 36% reduction in **Figure 4.10(d)** indicates that the kink poses a thermal resistance that is ~30 times of a straight wire segment with a length equivalent to that of the kink center-line (~80 nm). Note that the smaller reduction is due to the higher carbon concentration, larger diameter, or longer suspended length of the kinked wires. Importantly, detailed TEM studies have shown that the kinked regions in these samples are all single-crystalline and defect-free as shown in **Figure 4.10(e&f)** for two measured samples. Therefore, the reduced thermal conductivity cannot be attributed to low structural quality at the kinks; and it is indeed the kinked morphology, rather than other factors, poses remarkable thermal resistance.

Even though there are variations with the sample carbon concentration, the kink resistance demonstrates a general trend of higher resistance for larger diameter wires (**Figure 4.11(a)**). A possible reason for this is the more pronounced kink resistance as the boundary scattering from the wire surface weakens. The kink resistance for unit cross-sectional area also shows an increasing trend versus the wire diameter. The resistance for unit area lies in the range of $1.59\text{-}5.20\times10^{-7}$ m^2-K/W, as plotted in **Figure 4.11(b)**, which converts to an interfacial thermal conductance (ITC) of 1.92-6.26 MW/m^2-K. This resistance is remarkable; in fact, the ITC is even lower than the values for most metal-dielectric interfaces, such as Au/Si, Pb/Si, Bi/Si, Pb/diamond, and Bi/diamond, which utilized high mismatch of their Debye temperatures to achieve an ITC as low as 8.5 MW/m^2-K. Note that typical phonon-mediated interfaces between dissimilar materials have an ITC lying in the range of 8.5-700 MW/m^2-K (Costescu et al. 2003, Dechaumphai et al. 2014, Lyeo & Cahill 2006, Stoner & Maris 1993).

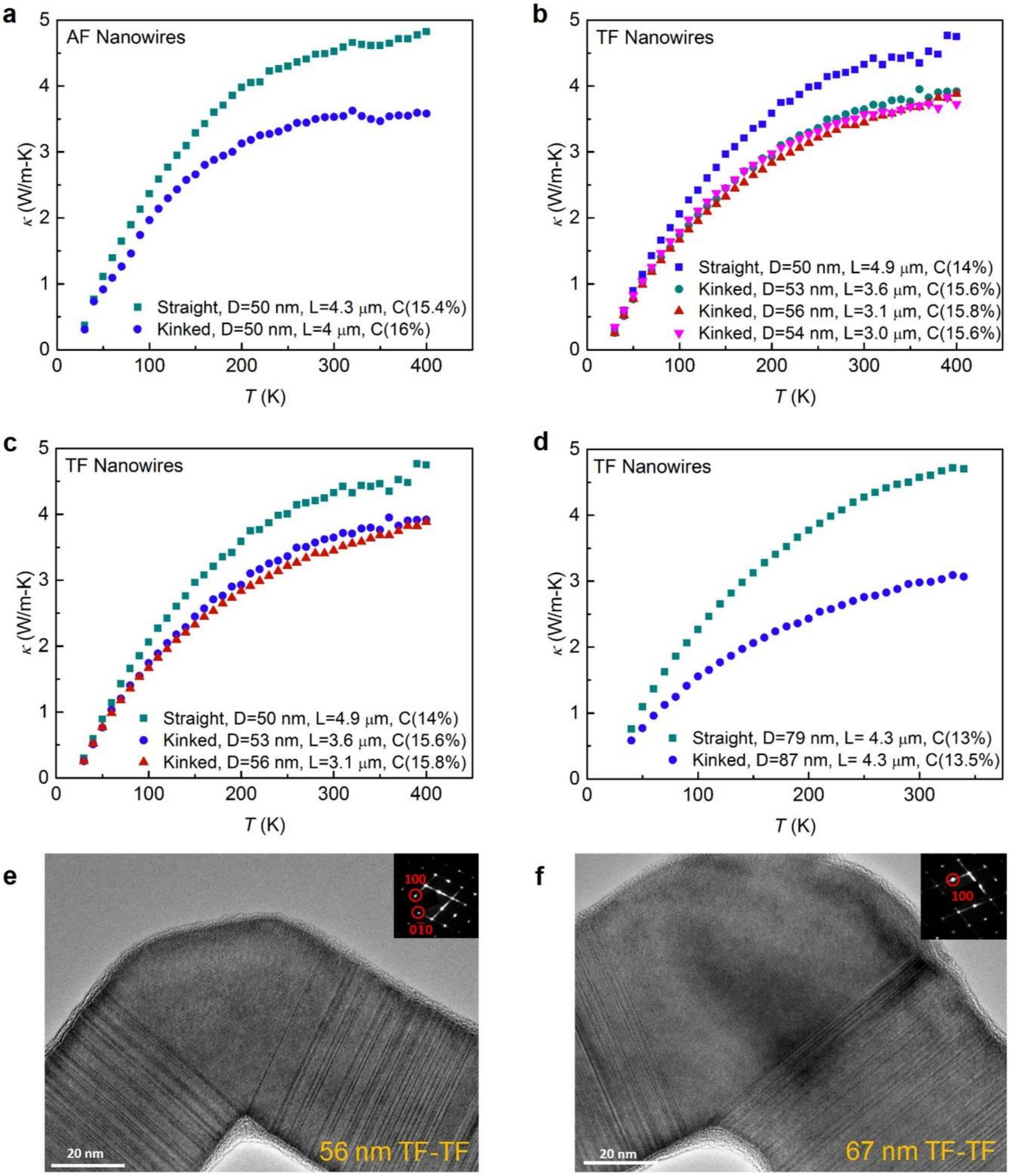

Figure 4.10 Reduction of thermal conductivity in kinked boron carbide nanowires. (a-d) Thermal conductivities of different pairs of kinked and straight nanowires. (e-f) TEM images show single crystalline kinked regions of two measured TF nanowires, indicating defect-free kinks.

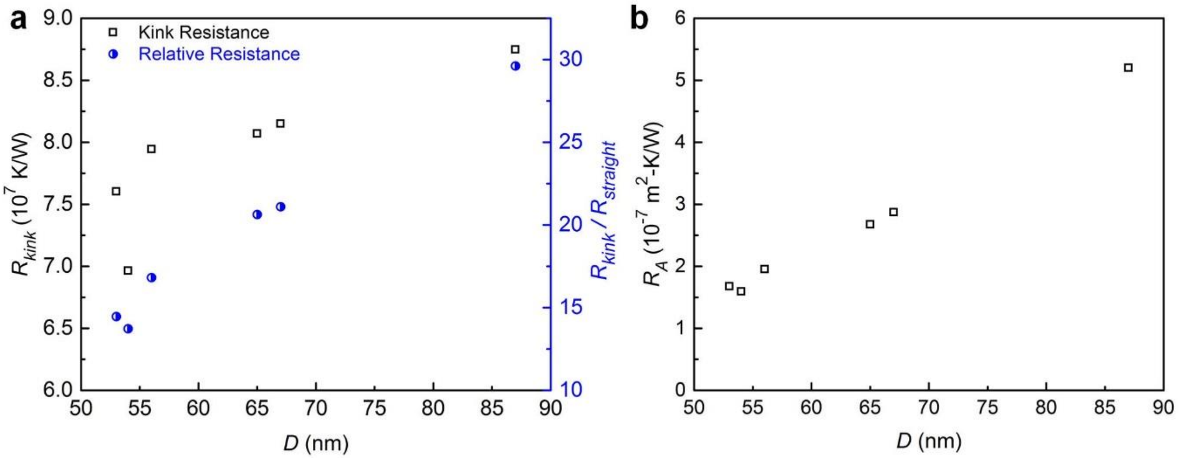

Figure 4.11 Thermal resistance of the kink at room temperature. (a) Absolute and relative kink thermal resistance versus wire diameter. The normalized kinked resistance shows the ratio of kink resistance to that of a straight wire segment of equivalent length. (b) Kink resistance for unit cross-sectional area.

The pronounced kink resistance is truly unexpected, as previous reports have shown that bending carbon nanotubes (Chang et al. 2007) or backscattering from sawtooth nanowire boundaries (Moore et al. 2008) does not or only poses limited resistance to thermal transport. More importantly, the observation is not consistent with the prediction based on the common picture of phonon transport in nanowires, which treats phonons as isotropically propagating particles that experience diffuse scattering at wire surface (Maldovan 2011, Mingo et al. 2003, Sellan et al. 2010). In fact, this picture could lead to a slightly lower thermal resistance at the kink, as discussed later.

In addition to defect-free kinks, we found some nanowires with kinks that have clear structural defects (**Figure 4.12(b&c)**), which are oriented in parallel to the stacking faults orientation in one of the legs. Intriguingly, measurements of three such nanowires all indicate that their thermal conductivities are actually higher than that of comparable nanowires with defect-free kinks, even though the value is still lower than that of straight wires of comparable structure and composition

(**Figure 4.12(a)**). It is well-known that defects can scatter phonons and pose resistance to their transport (Klemens 1960, Murphy et al. 2014). Therefore, the observation here is counter-intuitive and falls into a regime where defects actually assist phonon transport.

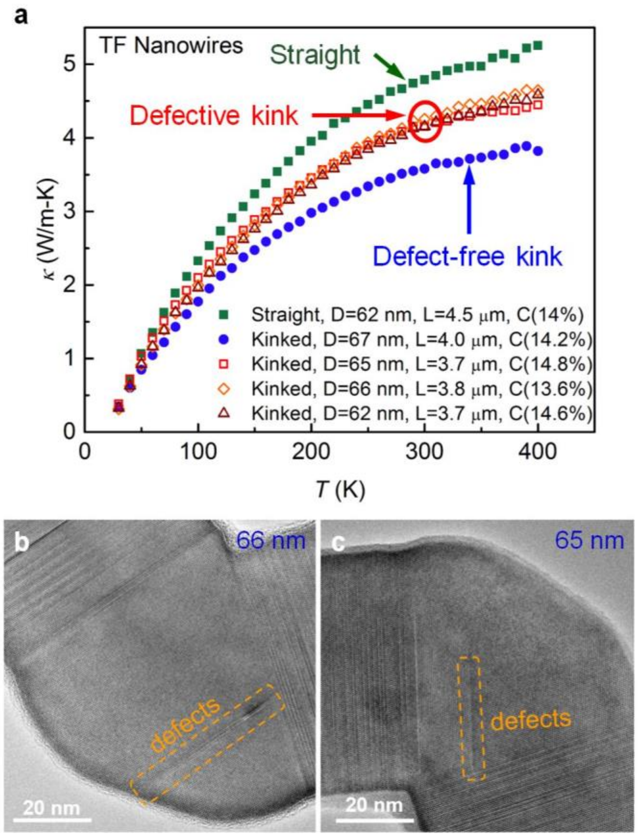

Figure 4.12 Defects assist phonon transport across the kink. (a) Thermal conductivity of boron carbide nanowires that are straight, with defect-free kinks and with defective kinks, respectively. (b-c) TEM images show the defects in the kinks of kinked boron carbide nanowires.

While we have not seen any experimental studies of kink effects on thermal transport through nanowires, Jiang et al. recently reported a MD study on kinked silicon nanowires (Jiang et al. 2013a). Their results showed that for a wire of 1.1 nm in diameter with two 9.5 nm long legs on each side of a kink, the kink could reduce the thermal conductivity by ~20% at 300 K. They attributed the reduction to a 'pinching' effect that originates from the fact that atoms in the two sides of the kink could vibrate in orthogonal directions for the same phonon mode. As such, phonons have to make mode conversions to transmit through the kink. Note that when using thermal conductivity reduction to measure the kink effect, the kink resistance is weighted by the total wire length. As such, comparing the 20% reduction from a kink of 1.1 nm in a 19 nm long wire (MD results) with the 36% reduction from a kink of ~80 nm in a 4.3 μm long wire (**Figure 4.10(d)**), our experimental data presents a kink resistance that is ~7 times more pronounced than the MD prediction if we normalize the kink resistance with respect to the resistance of a corresponding straight wire segment of equivalent length.

4.4 Phonon Focusing in Boron Carbides

To explain these puzzling observations, we first summarize several understandings from our results with straight nanowires since the phonon properties of boron carbides are not readily available. First, the intrinsic phonon mean free path (MFP) should be much larger than the wire diameter since we see diameter dependence for nanowires with similar carbon concentrations. This is very reasonable because the measurement temperature range is much lower than the Debye temperature (~1501 K for $B_{5.6}C$) (McClellan et al. 2001); and therefore, the excited phonons are of relatively long wavelengths, which normally correspond to longer MFPs. Additionally, the complex crystal structures and planar defects can effectively scatter short wavelength phonons, which renders longer wavelength phonons more important in thermal transport.

Another important fact is that the dependence of the thermal conductivity on wire diameter is weaker than that of silicon wires, as shown in **Figure 4.13** (Li et al. 2003b). Since the measured thermal conductivity increases monotonically with temperature, the weaker diameter dependence should not come from Umklapp scattering. Instead, it is more reasonable to attribute the less pronounced diameter dependence to the highly anisotropic elastic moduli of boron carbides (ranging from 64 to 522 GPa) (McClellan et al. 2001). Elastic anisotropy is closely correlated with phonon focusing, resulting in crystallographic direction-dependent phonon transport (McCurdy 1974). which can have important effects on thermal transport through nanostructures (Yang et al. 2014).

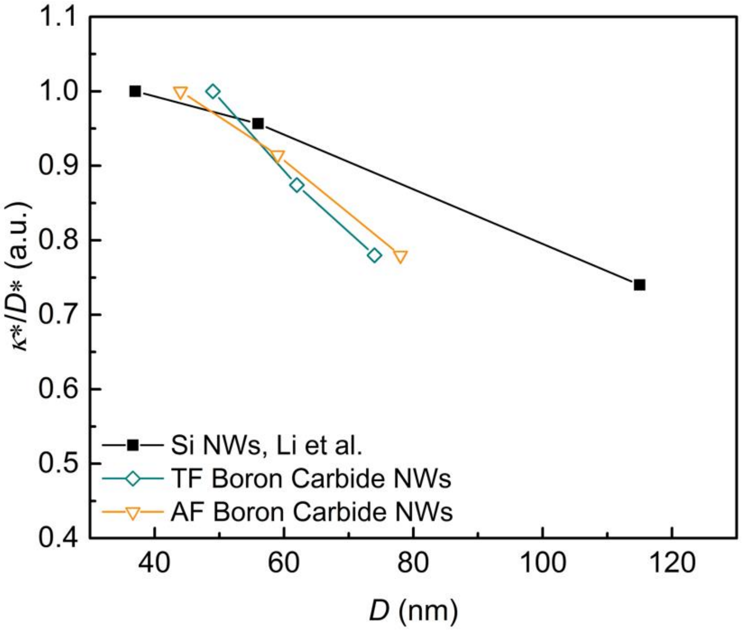

Figure 4.13 Diameter dependence of the thermal conductivity at 300 K for boron carbide nanowires in comparison to that of Si nanowires (Li et al. 2003b).

One important factor contributing to the directional dependence of thermal conductivity is phonon focusing, which can be visualized with the low frequency acoustic iso-energy surface. Wei et al. (Wei et al. 2016) has shown that the low frequency phonon properties can be derived from either lattice dynamics method or elastic constants-based continuous mechanics method. Here, we use the latter method (Hurley & Wolfe 1985, Wolfe 1998) to calculate the acoustic iso-energy surface of bulk B_4C, using the elastic constants calculated by Taylor et al. (Taylor et al. 2012). Importantly, although the calculation is based on B_4C, the results are applicable to boron carbides with lower carbon concentration, as the elastic constants and the level of elastic anisotropy do not vary much with the carbon concentration (McClellan et al. 2001, Taylor et al. 2012).

The B_4C structure belongs to the $R\bar{3}$m space group. Thus, there are in total six independent elastic constant components (Nye 1985). The general Hooke's law between stress tensor σ_{ij} and strain tensor ϵ_{ij} for this crystal is,

$$\begin{bmatrix} \sigma_{xx} \\ \sigma_{yy} \\ \sigma_{zz} \\ \sigma_{yz} \\ \sigma_{zx} \\ \sigma_{xy} \end{bmatrix} = \begin{bmatrix} C_{11} & C_{12} & C_{13} & C_{14} & 0 & 0 \\ C_{12} & C_{11} & C_{23} & C_{24} & 0 & 0 \\ C_{13} & C_{23} & C_{33} & 0 & 0 & 0 \\ C_{14} & C_{24} & 0 & C_{44} & 0 & 0 \\ 0 & 0 & 0 & 0 & C_{44} & C_{56} \\ 0 & 0 & 0 & 0 & C_{56} & C_{66} \end{bmatrix} \times \begin{bmatrix} \varepsilon_{xx} \\ \varepsilon_{yy} \\ \varepsilon_{zz} \\ \varepsilon_{yz} \\ \varepsilon_{zx} \\ \varepsilon_{xy} \end{bmatrix}, \tag{4.1}$$

where C_{11}, C_{12}, C_{13}, C_{14}, C_{33}, and C_{44} are independent elastic elements, and C_{23}=C_{13}, C_{24}=-C_{14}, C_{56}=C_{14}, and C_{66}=(C_{11}-C_{12})/2.

For any control volume in solid, Newton's second law is written as,

$$\begin{cases} \rho \dfrac{\partial^2 U}{\partial t^2} = \dfrac{\partial \sigma_{xx}}{\partial x} + \dfrac{\partial \sigma_{zx}}{\partial z} + \dfrac{\partial \sigma_{xy}}{\partial y} \\ \rho \dfrac{\partial^2 V}{\partial t^2} = \dfrac{\partial \sigma_{yy}}{\partial y} + \dfrac{\partial \sigma_{yz}}{\partial z} + \dfrac{\partial \sigma_{xy}}{\partial x} \\ \rho \dfrac{\partial^2 W}{\partial t^2} = \dfrac{\partial \sigma_{zz}}{\partial z} + \dfrac{\partial \sigma_{yz}}{\partial y} + \dfrac{\partial \sigma_{zx}}{\partial x} \end{cases}, \tag{4.2}$$

Inserting Equation (4.1) to (4.2), and assuming the plane-wave displacement solution,

$$\begin{cases} U = U_0 e^{-i(\omega t - \vec{q}\cdot\vec{r})} \\ V = V_0 e^{-i(\omega t - \vec{q}\cdot\vec{r})} \\ W = W_0 e^{-i(\omega t - \vec{q}\cdot\vec{r})} \end{cases}, \tag{4.3}$$

we can obtain the Christoffel's equation of crystal with $R\bar{3}m$ symmetry as,

$$\begin{bmatrix} C_{11}\cdot k_x^2+C_{66}k_y^2+C_{44}k_z^2+2C_{56}\cdot k_y k_z & (C_{12}+C_{66})k_x k_y+(C_{14}+C_{56})k_x k_z & (C_{14}+C_{56})k_x k_y+(C_{13}+C_{44})k_x k_z \\ (C_{12}+C_{66})k_x k_y+(C_{14}+C_{56})k_x k_z & C_{11}\cdot k_y^2+C_{66}k_x^2+C_{44}k_z^2+2C_{24}\cdot k_y k_z & C_{24}\cdot k_y^2+C_{56}k_x^2+(C_{23}+C_{44})k_y k_z \\ (C_{14}+C_{56})k_x k_y+(C_{13}+C_{44})k_x k_z & C_{56}k_x^2+C_{24}k_y^2+(C_{23}+C_{44})k_y k_z & C_{44}k_x^2+C_{44}k_y^2+C_{33}\cdot k_z^2 \end{bmatrix} \begin{bmatrix} U_0 \\ V_0 \\ W_0 \end{bmatrix} = \rho\omega^2 \begin{bmatrix} U_0 \\ V_0 \\ W_0 \end{bmatrix} , \quad (4.4)$$

where k_x, k_y, and k_z are the wavevector components, ω is the phonon angular frequency, and ρ is the density of boron carbide. From Equation (4.4), we know that $\rho\omega^2$ is the eigenvalue of the left matrix. The phonon frequency can be calculated for any specific wavevector.

Following the above procedure, the 3D acoustic iso-energy surfaces were calculated for boron carbides and shown in **Figure 4.14**. It indicates that all three branches of phonons are focused along certain directions. For example, the LA phonons are focused along the X, Y, and Z axes.

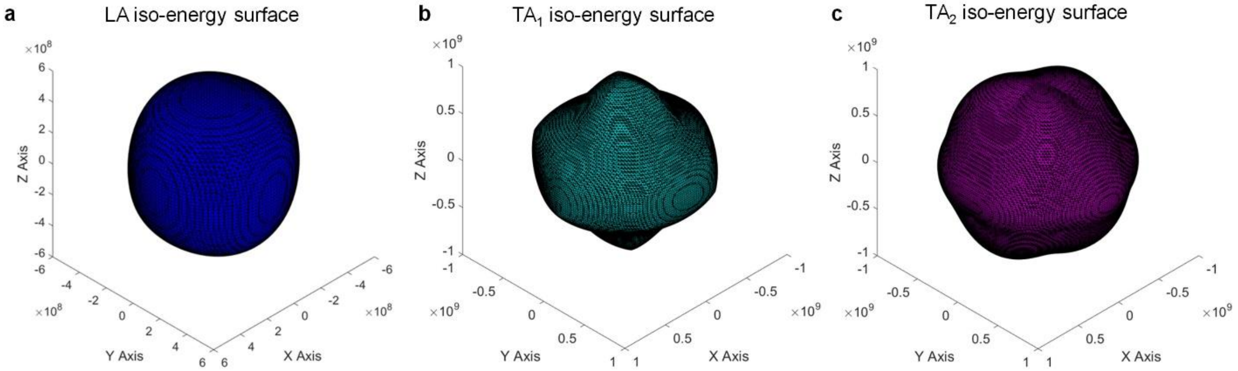

Figure 4.14 Calculated 3-D acoustic iso-energy surfaces for boron carbides. (a) longitudinal acoustic (LA) phonons; (b) fast transverse acoustic (TA_1) phonons; (c) slow transverse acoustic (TA_2) phonons.

When studying the rhombohedral lattice, a non-primitive hexagonal unit cell is commonly used (McClellan et al. 2001, Taylor et al. 2012). **Figure 4.15** shows the relation between the primitive rhombohedral cell (light blue dashed lines) and the non-primitive hexagonal cell (black dashed lines). It is clear that the [111] rhombohedral direction corresponds to the [001] hexagonal direction. For the tensor analysis, such as the aforementioned calculation of iso-energy surfaces, a new set of orthogonal axes is needed. We selected the X, Y, and Z axes following the conventions discussed in Nye's book (Nye 1985) and *Standards on Piezoelectric Crystals* (Brainerd et al. 1949). As shown in **Figure 4.15**, none of the X, Y and Z axes coincide with the growth directions of our AF and TF nanowires. Thus, the phonon focusing effects along the axial directions of AF and TF nanowires are not readily available. To show phonon focusing in AF and TF nanowires, we derived a conversion matrix to transform the rhombohedral coordinate to the orthogonal coordinate, and intersect the iso-energy surfaces with the planes corresponding to orthogonal directions containing the growth directions of AF and TF nanowires. The attained iso-energy surface intersections on AF-O-TF, ⊥-O-TF, and ⊥-O-AF planes are shown in **Figure 4.16**. Note that the AF-O-⊥ plane is the basal plane of boron carbides in the primitive rhombohedral lattice and the TF direction is perpendicular to this basal plane.

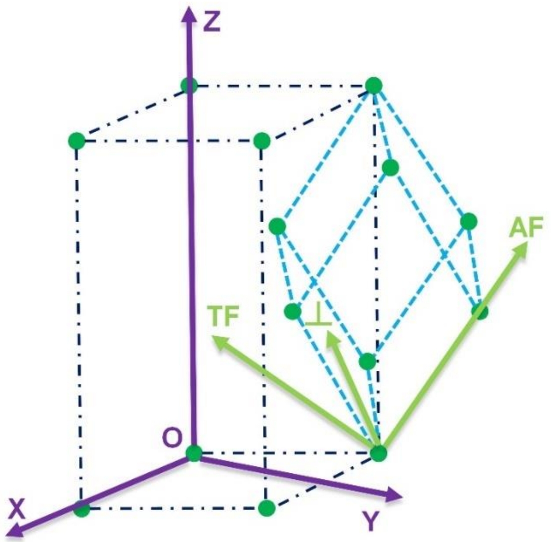

Figure 4.15 Main axes in the primitive rhombohedral cell and non-primitive hexagonal cell. The rhombohedral unit cell is drawn with light blue dashed lines, and the hexagonal one with black dashed lines. The orthogonal X, Y, and Z directions are indicated by the purple solid lines and the AF, ⊥, and TF directions are shown with green color.

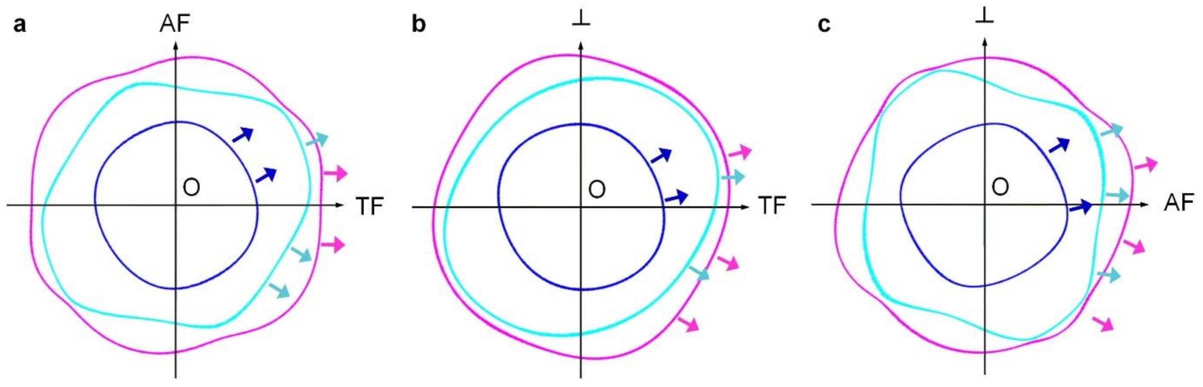

Figure 4.16 The intersections of acoustic iso-energy surfaces for boron carbide with three orthogonal planes by solving the Christoffel's Equation. (a) AF-O-TF plane; (b) ⊥-O-TF plane; and (c) ⊥-O-AF plane. The axes are the wavevectors, and the specified frequency is 1 THz. Solid lines with different colors represent different phonon branches: longitudinal acoustic (LA) phonons (blue, innermost), fast transverse acoustic (TA_1) phonons (cyan) and slow transverse acoustic (TA_2) phonons (magenta, outermost).

The phonons focused along the AF and TF directions are of interest, as these phonons travel along the nanowire growth direction and experience less boundary scattering. As such, they could make more contributions to thermal transport than the phonons travelling in other directions. For example, a significant portion of TA_2 phonons are focused along the TF directions in the AF-O-TF plane. For the TA_1 and LA phonons, although they are not focused perfectly along the TF direction, a significant portion of these phonons are focused to travel within a small angle from the TF direction. In ⊥-O-AF plane, majority of TA_1 phonons are focused along the AF direction, and a considerable portion of TA_2 and LA phonons prefer to travel within a small angle from the AF direction.

4.5 Monte Carlo Simulation of Phonon Transport in Kinks

Armed with these understandings, we explore the kink resistance through a ray tracing-based MC simulation of phonon transport through an ‘L” shaped kink of 80 nm side length, which is compared with the case for a straight wire segment of 80 nm long, equivalent to the center-line length of the kink. In the simulation, we assume that phonons can only propagate within a certain angle (focus angle) from the axial directions as shown in the insets of **Figure 4.17**. Moreover, we consider phonon reflection from the wire surface as diffuse within the allowable propagation angle but neglect three-phonon scattering, which is reasonable if the intrinsic MFPs are much larger than the wire diameter. Under this condition, 200,000 phonons, which represent the total amount of heat transfer, are emitted from a random location at the entrance with a direction randomly distributed within a focus cone and forced to transmit through the kink and the straight wire segment, respectively. The total travel distance of all phonons is calculated, which represents the resistance if the speed of sound is taken as a constant. Note that to enforce the fixed amount of heat transfer of 200,000 phonons, if a phonon comes back to the inlet, it is reflected back into the simulation domain but phonons are allowed to leave the exit.

Figure 4.17 plots the calculated resistance of the kink and the straight segment, both normalized to the resistance of the straight segment under the fully diffuse condition, i.e., a focus angle of 90°. For fully diffuse transport, the resistance of the kink is actually less than that of the straight segment. However, as the focus angle reduces, the resistance of the straight wire segment drops because of diminishing phonon-boundary scattering. In contrast, for the kink, its resistance increases rapidly as the focus angle reduces, which is a direct result of back reflection of phonons to the inlet. These opposite trends of the resistance clearly show how back reflection of focused phonons can lead to a remarkable kink resistance in boron carbide nanowires.

Figure 4.17 indicates that at a focus angle of 30° (corresponding to a focus cone with an apex angle of 60°), the kink has a resistance that is ~7.4 times of the corresponding straight wire segment, which is still much less than the ~30 times from the experiment. This is because by allowing all phonons reaching the kink exit to leave the simulation domain, we neglect the resistance associated with mode conversion. The phonons leaving the kink are not focused along the axial direction of the downstream leg and still need to undergo mode conversion to become phonons focused along the axial direction in that leg, which pose additional resistance as discussed in Jiang et al. (Jiang et al. 2013a).

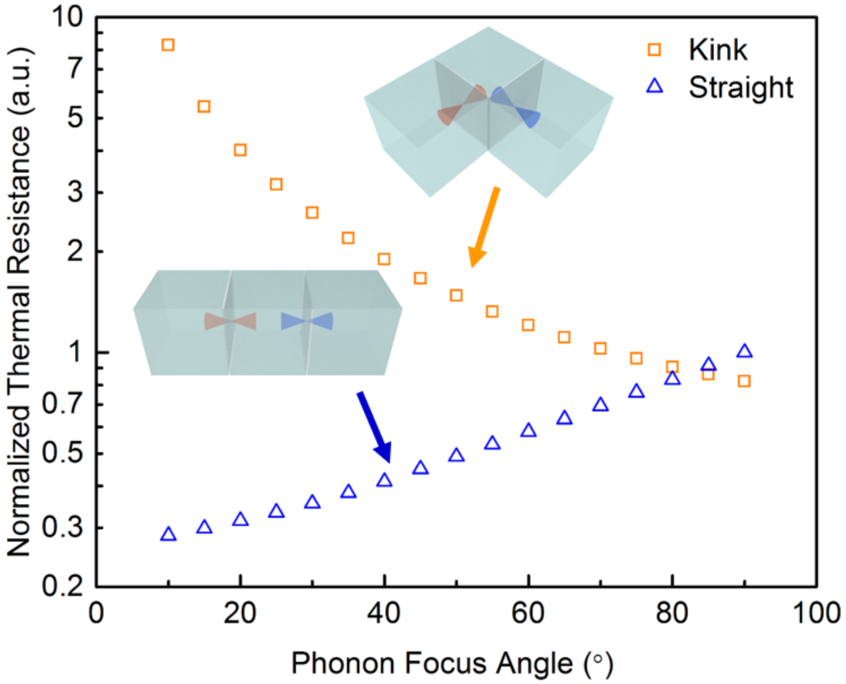

Figure 4.17 Comparison of the normalized thermal resistance between the kink and straight wire segment. The insets illustrate the MC simulation domain and the phonon focusing effects with the head-to-head cones.

The above analysis suggests that for highly focused phonons to enter the opposite leg of a kink, they have to undergo scattering to make the turn. As such, more scattering events in the kink will help to change the phonon propagation direction and reduce the kink resistance. This hypothesis is strongly supported by our observation from the wires with defective kinks, which have a smaller resistance than defect-free kinks (Zhang et al. 2017).

4.6 Thermoelectric Figure of Merits (ZTs) of Boron Carbide Nanowires

The ZT of boron carbides has been long projected to be able to achieve unity at high temperature (Bouchacourt & Thevenot 1981, Thévenot 1990). However, the bulk thermoelectric property currently suffers significant variation due to different sample preparation methods. We sought to characterize the thermoelectric property of individual single crystalline boron carbide nanowires using the suspended micro-thermometry elaborated in Chapter 2. The boron carbide nanowires feature around 2 nm oxide-rich amorphous coating layer, which will pose great electrical resistances and disable electrical measurements. Therefore, prior to EBID Pt-C depositions, the boron carbide nanowires underwent electron-beam assisted local XeF_2 etching at the contacts (Utke et al. 2008), which took away the oxide layer and enable subsequent thermoelectric property measurements. More samples need to be done to dissect the impact of carbon content, diameter and stacking faults/orientation on thermoelectric transport of boron carbide nanowires. Such knowledge will be valuable to understand the transport property of boron carbides and develop a durable method to improve its thermoelectric property.

Figure 4.18(a) presents the ZT measured from two boron carbide nanowires as a function of temperature. The value increases dramatically with temperature. In fact, another order of magnitude enhancement could be anticipated when the temperature increases beyond 1000 K. Comparing our current acquired data with previous bulk data reveals that the measured ZT is considerably higher than that for hot-pressed samples. If the enhancement continues up to higher temperature up to 1000 K, we expect to achieve a ZT larger than 1. The comparison shows that, compared to hot-pressed samples, boron carbide nanowires possess better thermoelectric property. The enhancement mainly originates from the suppressed thermal conductivity and absence of grain boundaries.

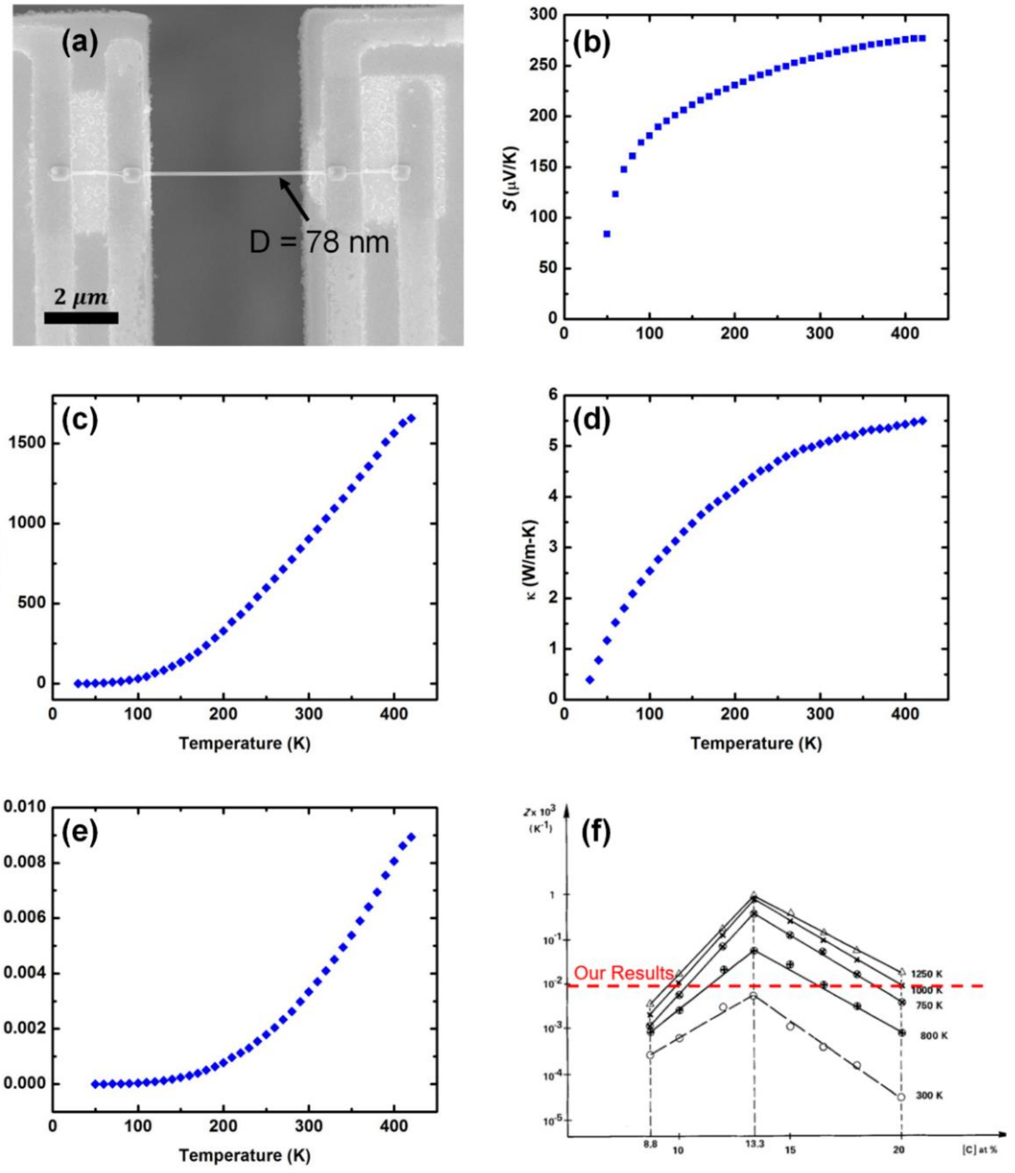

Figure 4.18 Thermoelectric property of one boron carbide nanowire. The ZT was enhanced to twice the bulk value. (a) SEM image showing the nanowires bonded onto the electrodes. Measured (b) Seebeck coefficients; (c) electrical conductivity; (d) thermal conductivity; (e) ZT; (f) comparison of our results to literature value (Bouchacourt & Thevenot 1985).

Doping strategy has already proven to be very efficient to improve the thermoelectric properties. Various dopants have been applied to boron carbides, such as Ni (Hong et al. 2010), Si (Proctor et al. 2015) and Al (Liu 2000). All these dopants showed notable effects on modifying the electronic property of boron carbides. Currently, based on the results accumulated on several nanowires, the relatively low electrical conductivity poses a limit to further enhancement of boron carbide nanowires' thermoelectric properties. Doped boron carbide nanowires with Al have been synthesized, more work will be conducted to explore these nanowires.

4.7 Summary

In this chapter, we observed remarkable thermal resistance at the kinks in boron carbide nanowires, which is attributed to the combined effects of backscattering of highly focused phonons and the required mode conversion. Importantly, we demonstrate that defects, instead of posing resistance, facilitate phonon transport through the kink by scattering phonons into the opposite leg. These discoveries provide insights into phonon transport through kinks or bends in nanostructures and a novel mechanism to engineering thermal conductivity. Given that several high-performance thermoelectric materials, such as Bi_2Te_3 (Zhao et al. 2008) and SnSe (Zhao et al. 2014), are also of strong elastic anisotropy and possess highly crystallographic direction-dependent thermal conductivity, introducing kinks in nanostructured Bi_2Te_3 and SnSe could further reduce their thermal conductivities and enhance thermoelectric performance. Our findings also have important implications in precise thermal management of nanoelectronic devices given the ubiquitous kink-like wire morphology in nanoelectronic circuits.

Preliminary thermoelectric measurements showed that the thermoelectric property of boron carbide nanowires is improved compared with bulk. Meanwhile, the results indicate a strong increasing trend of the ZT as a function of temperature. It could make a desirable high temperature thermoelectric material in consideration of its thermal stability and significant thermoelectric power. The results show that nanostructured boron carbides could be an interesting candidate for high temperature thermoelectrics.

5. Thermal Transport in Quasi-1D vdW Crystal Nanowires

The discovery of graphene (Novoselov et al. 2004) and other two-dimensional (2D) materials has fueled enormous interest in exploration of new groups of vdW nanomaterials and their novel properties. Similar to the case of graphite, whose successful exfoliation could lead to monolayer or few-layer graphene, successful separation of quasi-one-dimensional (quasi-1D) vdW crystals gives rise to quasi-1D vdW nanowires owing to their excellent scalability (Autès et al. 2015, Liu et al. 2016, Ning et al. 2015). The quasi-1D structures hold lots of interesting properties, such as topological insulator (Autès et al. 2015, Huang & Duan 2016) and superconductor-insulator transition (Ning et al. 2015). They have also demonstrated potentials for practical applications, such as in thermoelectrics (Chung et al. 2000) and transistors (Buscema et al. 2015, Liu et al. 2016). One important application is as interconnects in nanoelectronics (Stolyarov et al. 2016), taking advantage of their excellent scalability and considering the ever-escalating resistivity from miniaturizing the commonly used copper interconnects.

Thermal properties of vdW crystals are important considerations for many of their applications and have attracted significant attention (Ghosh et al. 2010, Henry et al. 2010, Pop et al. 2012). Critical questions such as the effects of dimensionality and phonon focusing on thermal transport in these materials have been debated but a comprehensive understanding still has not been achieved. Moreover, while 2D vdW materials have been intensively studied, thermal transport properties of quasi-1D vdW crystals have been rarely probed, while exploration of these materials systems could provide important new data to understand thermal transport in vdW crystals (Cai et al. 2017, Liu et al. 2016, Stolyarov et al. 2016).

The quasi-1D vdW crystals also make an excellent system for probing ballistic phonon transport. It has been predicted that for truly 1D materials, thermal conductivity becomes divergent, manifested by the continuously increasing thermal conductivity with the sample length (Henry & Chen 2009, Liu & Yang 2012). In reality, defects and Umklapp scattering can lead to finite thermal conductivity and the thermal conductivity has been demonstrated to increase with sample length for up to 10 µm at room temperature (Liu et al. 2017). As such, it is interesting to examine the length dependence of the thermal conductivity of quasi-1D vdW materials to understand the effects of dimensionality and to see how persistent ballistic phonon transport can be in these materials. In view of the great potential of quasi-1D vdW crystals and the importance of their thermal properties, in this chapter, we report on the first experimental study of the thermal conductivity of quasi-1D $Ta_2Pd_3Se_8$ (TPdS) nanowires.

5.1 Microstructure and Sample Preparation

Figure 5.1(a-c) depict the highly anisotropic microstructure of TPdS, which consists of TPdS molecular chains extending along the axial direction (*c*-axis) as the fundamental building blocks. The inter-chain interactions are mediated by vdW forces between the Pd and Se atoms of neighboring chains, which is ~17 times weaker than the intra-chain covalent bonds between Pd and Se (Liu et al. 2016). It has been shown that individual molecular chains can extend along the *c*-axis up to centimeters, as determined from the synthesized centimeters long needle-like crystals (Liu et al. 2016). TPdS nanowires were prepared by liquid exfoliation, using isopropyl alcohol (IPA) as solvent through ultra-sonication (Ning et al. 2015). Nanowires acquired through direct exfoliation of high quality bulk materials are single crystals, making excellent specimens for subsequent property characterization. As shown in **Figure 5.1(e)**, the chain structure can be clearly identified in HRTEM examinations. The obtained nanowire suspension was then diluted and drop-casted onto a PDMS substrate. After the solvent evaporated, individual nanowires were selected, picked up using a sharp probe attached to the micromanipulator, and transferred to the measurement device to bridge two suspended membranes as heat source and heat sink. EBID was done to minimize the contact thermal resistance and establish good electrical contacts, as shown in **Figure 5.1(d)**.

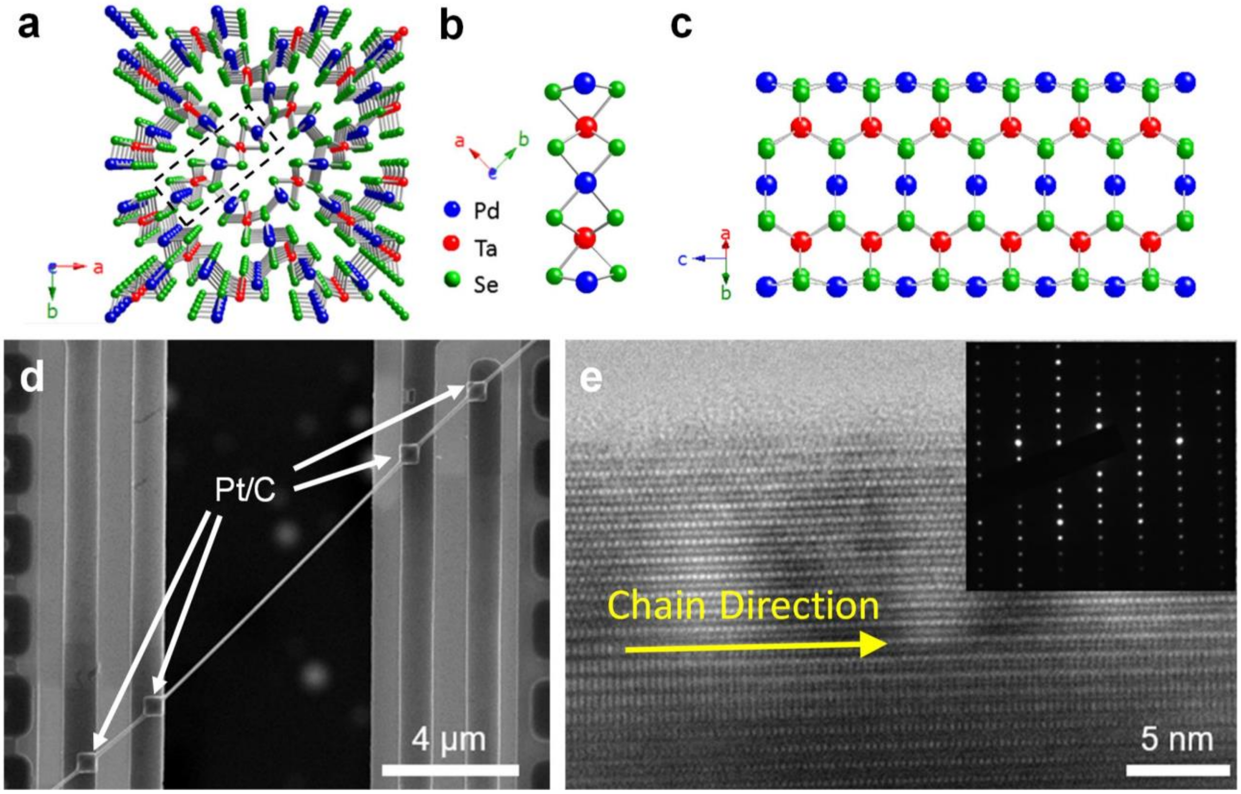

Figure 5.1 Crystal structure and thermal conductivity measurement scheme of TPdS nanowires. (a) perspective view of bulk TPdS viewed along *c*-axis. (b) Schematic of a single molecule ribbon along *c*-axis. (c) Side-view of a molecule ribbon extending along *c*-axis. (d) The nanowire was anchored onto the measurement device by EBID Pt. (e) HRTEM image showing perfectly aligned molecular chains. The inset is diffraction pattern, indicating the single crystalline structure.

Thermal conductivity measurements were subsequently conducted in a high vacuum cryostat, following the procedures described in Chapter 2. The contact thermal resistance has been confirmed to be negligible by comparing the measured thermal conductance after the first and second rounds of EBID, which delivered the same measurement results, as shown in **Figure 5.2**. To probe the length dependence of the thermal conductivity, the same nanowire was cut using the micromanipulator and re-suspended for several times with the length of the suspended section ranging from 2 μm to 21 μm (Yang et al. 2011).

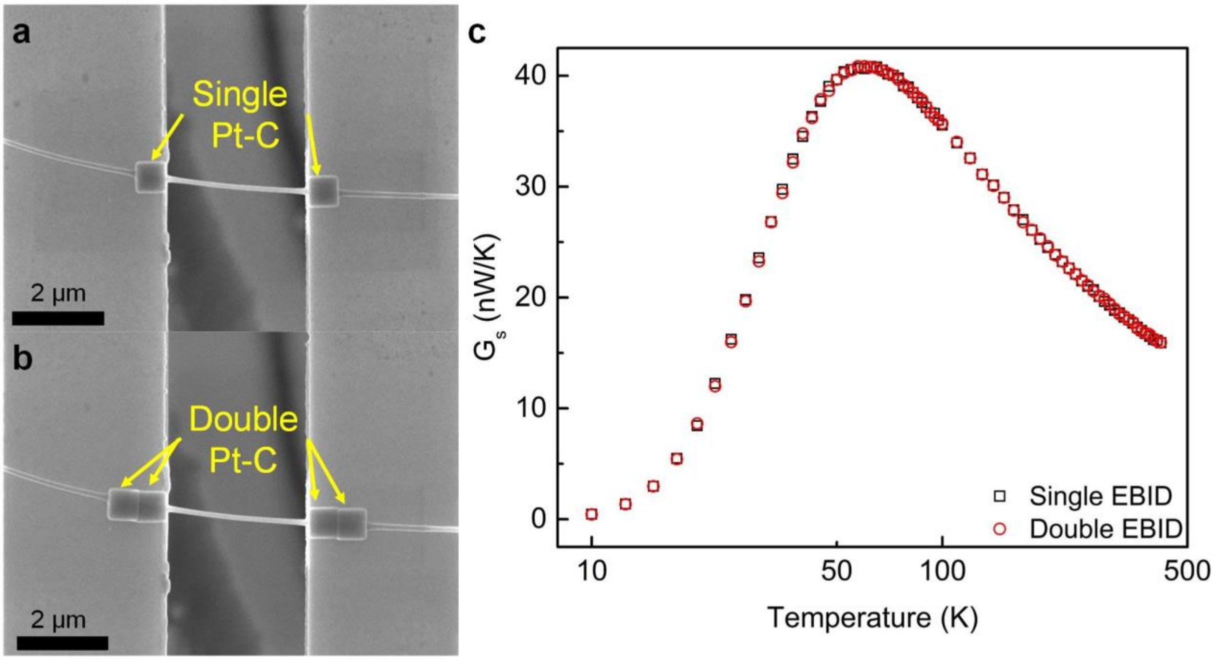

Figure 5.2 Contact thermal resistance characterization. SEM images showing the samples bonded with underlying device after (a) single EBID Pt-C bonds and (b) double EBID Pt-C bonds. (c) The measured thermal conductance of the control nanowire sample before and after doubling the contact area between the nanowire and the underneath membranes.

Different from nanowires synthesized with chemical vapor deposition, the cross sections of these exfoliated quasi-1D nanowires tend to be of irregular shapes. As such, detailed cross section characterization of each measured nanowire has to be carried out to allow for accurate determination of the thermal conductivity. To view the cross-section, we first used the focused ion beam (FIB, FEI Helios NanoLab G3) to deposit a layer of Pt on the nanowire and then applied a high ion current to cut open the cross-section. The deposited Pt served as an anchor and a protection layer to prevent damage of the nanowire surface during the cutting process. The obtained cross-section was then subjected to high resolution SEM imaging. The acquired SEM micrographs allow for extraction of the cross-sectional area and surface to volume ratio (SVR) of each nanowire. The SVR has been demonstrated to be a parameter more effective than the Casimir length in evaluating the impact of phonon boundary scattering (Chen et al. 2011, Yang et al. 2016).

5.2 Results and Discussion

Since the intra-chain covalent bonding between Pd and Se is ~17 times higher than the inter-chain vdW interactions between the Pd and Se residing on neighboring chains, it is interesting to see whether the thermal conductivity of the nanowire still display a dependence on the size of the cross-section. **Figure 5.3(a)** plots the thermal conductivity versus temperature for four samples of different SVRs, which indicates that even for such highly anisotropic quasi-1D nanowires, the thermal conductivity still exhibits a clear size effect. The nanowires with smaller SVRs, which correspond to larger cross-sectional areas, possess higher thermal conductivity. Since the length of the nanowires could also have an effect, we select samples of similar lengths for this comparison and make sure that nanowires of smaller SVRs are of shorter suspension lengths. In this way, any effect from the length difference will only counter the trend of SVR dependence so the actual thermal conductivity enhancement with reducing SVR will be more significant.

All four measured nanowires demonstrate a similar temperature dependence as follows. Their thermal conductivity ramps up quickly with increasing temperature from 15 K, reaching a peak value around 55 K, and then decreases with temperature, which is a signature of Umklapp scattering, as shown in **Figure 5.3(b)**. As the temperature rises beyond 100 K, the thermal conductivity display a trend of $T^{-0.6\sim0.7}$, with the exponent dropping from -0.6 to -0.7 as the wire cross-section size increases, approaching the T^{-1} behavior for bulk single crystalline materials. The slower drop rate can be attributed to phonon boundary scattering in nanowires; which also leads to a shift of the peak thermal conductivity towards higher temperature for nanowires of larger SVR, similar to that for silicon nanowires/ribbons (Li et al. 2003b, Yang et al. 2016). As discussed later, ballistic phonon transport still makes significant contribution in these 6-7 μm long wires so boundary scattering at the two ends of the nanowires also contribute to the deviation from the T^{-1} behavior.

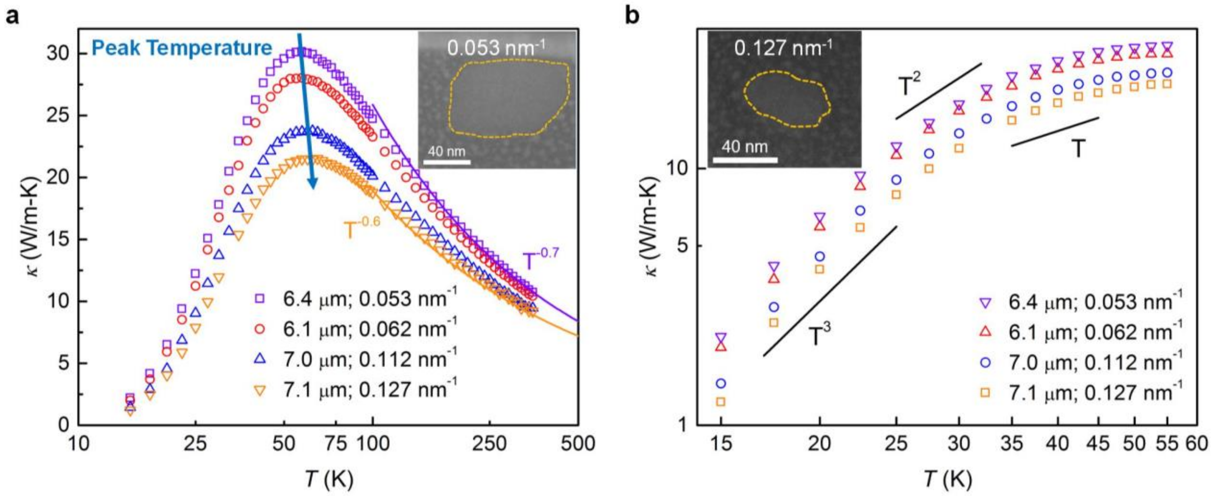

Figure 5.3 Thermal conductivity of TPdS nanowires. (a) Thermal conductivity of full temperature range. (b) Low temperature thermal conductivity of nanowires of varying SVRs, indicating strong size dependence. The curves of T^3, T^2, and T^1 are also shown for comparison. The insets are the HRSEM images showing cross sectional of two selected nanowires of different SVRs, whose contours were outlined by the dashed yellow lines.

The clear size dependency for vdW nanowires with characteristic cross-section length up to ~100 nm (see the inset in **Figure 5.3(a)**) is not as expected based on the behavior of 2D vdW materials. For most well-studied 2D vdW materials, including graphene (Ghosh et al. 2010), h-BN (Lindsay & Broido 2012), and MoS_2 (Gu et al. 2016), their in-plane thermal conductivity decreases as the thickness increases from monolayer to few layers. Importantly, the thermal conductivity quickly reaches bulk values when the number of layers increases to merely ~5, at which point the disturbance from the weak interlayer vdW interactions to phonons propagating within each layer saturates. Similar physics have been argued for ideally oriented 1D PE as well based on molecular dynamics results (Henry et al. 2010). We note that for some other 2D vdW materials, such as black phosphorus (Smith et al. 2017) and Bi_2Te_3, their thermal conductivity have been shown to increase with number of layers but quickly saturate to bulk values when the layer thickness reaches ~10 nm. In general, for vdW materials, the size dependence becomes absent for samples when their thickness or diameter is beyond ~10 nm; and therefore, the observed size dependence for the TPdS vdW nanowires with equivalent diameter up to >100 nm is counter-intuitive.

To understand the size dependence of the TPdS nanowire thermal conductivity, we first examine the temperature dependence of the thermal conductivity at low temperature, which follows the Debye T^3 law between 15 K to 25 K (**Figure 5.3(b)**), different from the expected linear relationship for 1D material systems such as single wall carbon nanotubes (Hone et al. 1999). We note that for graphite, its heat capacity obeys the T^3 law below 10 K, as a result of the contribution of both intra- and inter-layer phonon modes. The trend transitions to T^2 from 10 K to 100 K, when the in-plane phonon modes start to dominate over the low energy cross-plane modes sustained by weak vdW interactions (Klemens 1953, Pop et al. 2012). Compared to graphite, which has an inter-layer bonding energy of 0.05 eV, the inter-chain bonding energy for TPdS is significantly higher, 0.34 eV, which can sustain the propagation of inter-chain phonon modes of much higher energy. The extended temperature range in which the T^3 law holds for TPdS nanowires strongly suggest that this is indeed the case. As such, the inter-chain phonon modes should be able to make more contributions to thermal transport in TPdS than in graphite. On the other hand, while the intra-chain bonding energy, 5.7 eV, is comparable to the intra-layer *sp*^{2} bonding energy of graphite, 5.9 eV, the much more atoms (26) in each unit cell generate more optical phonon modes, facilitating the occurrence of Umklapp scattering. In addition, the much heavier atoms give rise to significantly lower speed of sound along the chain (denoted as the *a*-direction). As a result, the along chain thermal conductivity for TPdS nanowires is two orders of magnitude smaller than the in-plane thermal conductivity of graphite. The much enhanced inter-chain interaction and the significantly reduced contribution to thermal transport from intra-chain vibrations suggest that a notable weight of thermal conductivity along the *c*-axis is due to phonons propagating not along the *c*-direction.

The observed size dependence can then be explained based on the classical size effects from the phonon-boundary scattering. One challenge here is that for this to be true, the phonons propagating not along the *a*-direction need to have long mean free paths, comparable to the equivalent wire diameter of >100 nm. We believe that this could be the case given the recent demonstration of the very long phonon mean free path along the *c*-axis of graphite, which is ~200 nm at room temperature, two orders of magnitude larger than the traditionally believed value of merely a few nanometers (Yang et al. 2014).

In addition to the dependence of thermal conductivity on the cross-sectional size, it is also of great interest to explore its dependence on the sample length to explore ballistic transport along the chain in such quasi-1D materials systems (Liu & Yang 2012). To do so, we have measured the same nanowires with different lengths suspended between the heat source and sink, as shown in **Figure 5.4(a-c)**. As shown in **Figure 5.4d**, the measured thermal conductivity displays a clear dependency on the sample length as it varies from 4.9 μm to 11.2 μm, with higher thermal conductivity for longer suspension length. This trend holds even for rather high temperature of

350 K, as demonstrated in **Figure 5.4(e)**. This length dependence indicates very persistent ballistic phonon transport along the chain direction and invokes an interesting question: what the limit of the ballistic phonon transport length is in these quasi-1D nanowires?

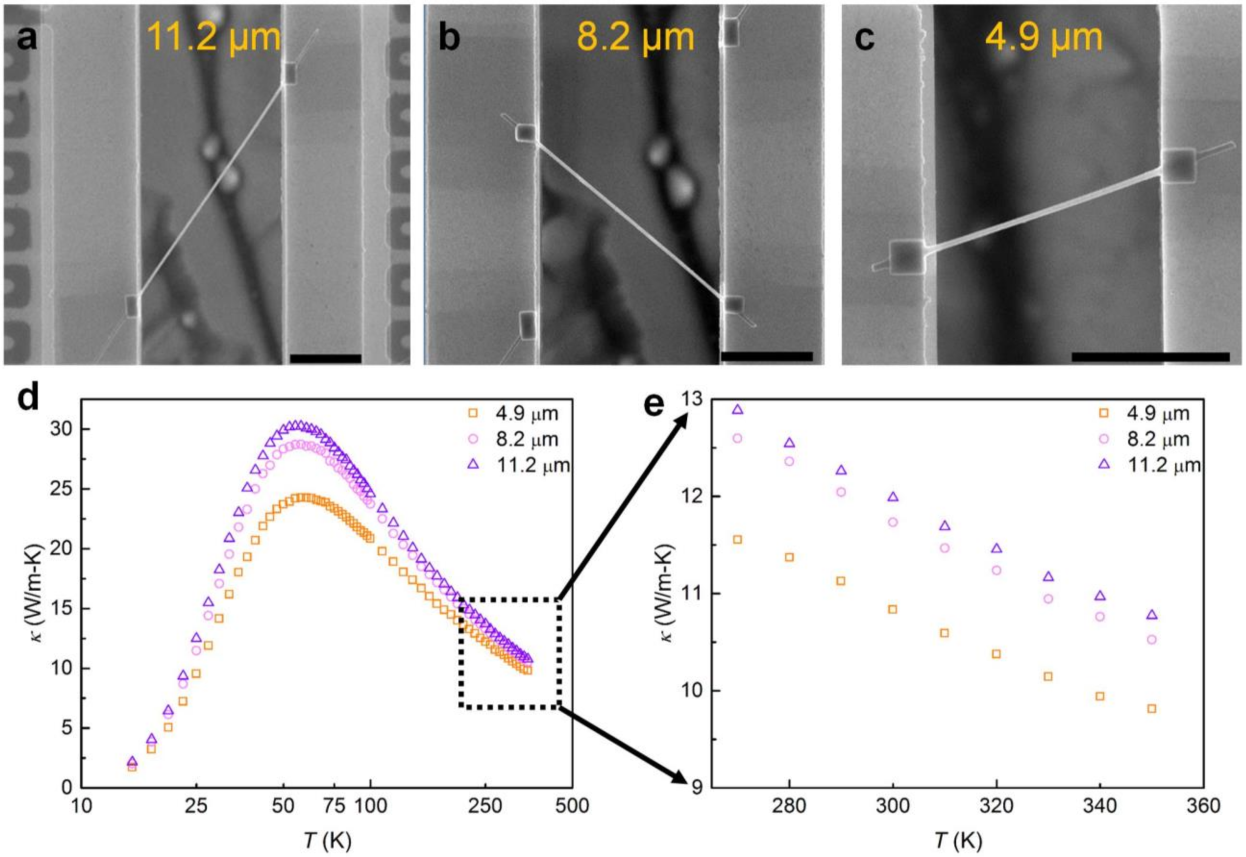

Figure 5.4 Length dependence of the thermal conductivity of one TPdS nanowire. (a-c) The same nanowire has been cut and suspended for a length of 11.2 µm, 8.2 µm, and 4.9 µm, respectively. The scale bars are 3 µm. (d) Measured thermal conductivity of one nanowire for three different suspended lengths plotted against temperature ranging from 15 K to 350 K. (e) Zoom-in view of the high temperature thermal conductivity from 270 K to 350 K.

To explore this limit, we measured the thermal conductivity of several nanowires of different suspended lengths. Since the thermal conductivity varies with the wire cross-section, to ensure meaningful comparison, either a very long nanowire was cut into several segments for different suspended lengths or a relatively long nanowire underwent cutting and re-suspension several times.

Figure 5.5(a&b) presents the measurement results showing the length dependence of thermal conductivity for four samples of different SVRs at both 55 K (the peak temperature) and 300 K, respectively. It can be clearly seen that the length dependence preserves up to 13 µm at 300 K, which is rather surprising, considering the low onset temperature of Umklapp scattering of ~55 K. The ballistic phonon transport can persist up to 13 µm at 300 K, which represents the longest distance that have been reported for room temperature ballistic phonon transport thus far. This value is larger than the reported 8.3 µm demonstrated in SiGe nanowires (Hsiao et al. 2013), and ~10 µm for single wall carbon nanotubes (Liu et al. 2017). This observation is quite unexpected given the clear thermal conductivity dependence on the cross-section size, indicating the significant role of phonon scattering at nanowire surface. It indicates that the along-chain vibrations also contribute a significant portion to the nanowire thermal conductivity and these vibration modes can propagate persistently over a quite long distance before Umklapp scattering occurs.

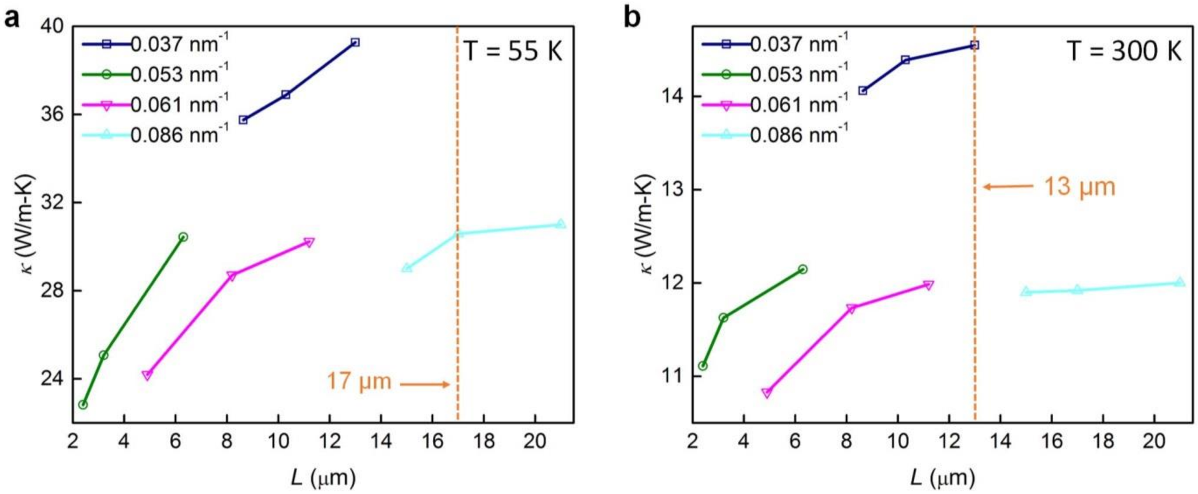

Figure 5.5 Length-dependent thermal conductivity of TPdS nanowires at (a) 55 K and (b) 300 K. The ascending thermal conductivity with increasing suspended length suggests existence of ballistic phonon transport up to 13 µm at 300 K and 17 µm at 55 K as indicated by the yellow dashed lines.

5.3 Summary

To conclude, we presented a systematic experimental study on the thermal conductivity of exfoliated quasi-1D $Ta_2Pd_3Se_8$ vdW nanowires. Interestingly, even though the atomic interactions along individual molecular chains is ~17 times stronger than the inter-chain vdW interactions, the measured thermal conductivity still shows a clear dependence on the cross-section size. The results also disclose that ballistic phonon transport can persist over a length of 13 µm at room temperature, the longest one reported thus far. These data provide new insights into phonon transport though quasi-1D vdW crystals, which are important for various applications of this class of novel materials.

6. Summary

This dissertation presents a series of experimental study on thermal transport through nanowires of fine structures. Using the a suspended microbridge thermal and thermoelectric measurement set-up with enhanced sensitivity, we were able to uncover several interesting thermal transport phenomena that yield better understanding of thermal transport at the nanoscale. This chapter serves to summarize our findings.

To enable an improve sensitivity, a Wheatstone bridge sensing scheme was incorporated to push the sensitivity down to the order of 10 pW/K, an improvement with almost two orders of magnitude better sensitivity than that for traditional 4-probe scheme, which situates at ~0.5 nW/K. Two radiation shields were incorporated in the set-up, which significantly mitigated radiation heat loss from the suspended structure, thereby enabling precise extraction of accurate transport properties of targeted nanostructures. A Monte Carlo approach was adopted to evaluate the uncertainty associated with the electrical thermal measurements and the dimensions determined from SEM, TEM, and AFM.

The relation between the electrospinning fabrication voltage, resulted nanofiber structure, and the corresponding thermal conductivity was experimentally explored. A ~20 times enhancement of the thermal conductivity for a PE nanofiber fabricated at 45 kV was achieved, which was correlated with the significantly improved molecular chain orientation and crystallinity, as carefully characterized using polarized micro-Raman spectroscopy.

Owing to the great potential of boron carbides as efficient thermoelectric materials, the thermal conductivity for individual boron carbide nanowires was carefully studied with the etch-through microdevices. Through systematic experimental measurements, it is shown that single-crystalline, defect-free kinks in boron carbide nanowires can pose a thermal resistance up to ~30 times larger than that of a straight wire segment of equivalent length. Analysis suggests that this pronounced resistance can be attributed to the combined effects of backscattering of highly focused phonons and required mode conversion at the kink. Interestingly, it is also found that instead of posing resistance, structural defects in the kink can actually assist phonon transport through the kink and reduce its resistance.

The thermal conductivity of exfoliated quasi-1D $Ta_2Pd_3Se_8$ vdW nanowires was experimentally probed for the first time. Interestingly, even though the atomic interactions along individual molecular chains is ~17 times stronger than the inter-chain vdW interactions, the measured thermal conductivity still shows a clear dependence on the cross-section size. The results also reveal that ballistic phonon transport can persist over a length of 13 µm along the chain at room temperature, the longest one reported thus far. These data provide new insights into phonon transport though quasi-1D vdW crystals.

REFERENCES

Afanasyev KA, Sansoz F. 2007. Strengthening in Gold Nanopillars with Nanoscale Twins. *Nano Letters*. 7(7):2056–62

An Q, Goddard W, Cheng T. 2014. Atomistic explanation of shear-induced amorphous band formation in boron carbide. *Physical Review Letters*. 113(9):1–5

Anselmi-Tamburini U, Munir ZA, Kodera Y, Imai T, Ohyanagi M. 2005. Influence of Synthesis Temperature on the Defect Structure of Boron Carbide: Experimental and Modeling Studies. *Journal of the American Ceramic Society*. 88(6):1382–87

Aselage TL, Emin D, McCready SS. 2001. Conductivities and Seebeck coefficients of boron carbides: Softening bipolaron hopping. *Physical Review B*. 64(5):54302

Aselage TL, Emin D, Samara GA, Tallant DR, Van Deusen SB, Eatough MO, Tardy HL, Venturini EL, Johnson SM. 1993. Phosphorus doping of boron carbides. *Physical Review B*. 48(16):11759–66

Aselage TL, Emin D, Wood C, Mackinnon I, Howard I. 1987. Anomalous Seebeck Coefficient in Boron Carbides. *MRS Proceedings*. 97(1):27

Ashbee KHG. 1971. Defects in boron carbide before and after neutron irradiation. *Acta Metallurgica*. 19(10):1079–85

Autès G, Isaeva A, Moreschini L, Johannsen JC, Pisoni A, Mori R, Zhang W, Filatova TG, Kuznetsov AN, Forró L, Van den Broek W, Kim Y, Kim KS, Lanzara A, Denlinger JD, Rotenberg E, Bostwick A, Grioni M, Yazyev O V. 2015. A novel quasi-one-dimensional topological insulator in bismuth iodide β-Bi_4I_4. *Nature Materials*. 15(2):154–58

Balakrishnarajan MM, Pancharatna PD, Hoffmann R. 2007. Structure and bonding in boron carbide: The invincibility of imperfections. *New Journal of Chemistry*. 31(4):473

Barth S, Boland JJ, Holmes JD. 2011. Defect Transfer from Nanoparticles to Nanowires. *Nano Letters*. 11(4):1550–55

Bellan LM, Craighead HG. 2008. Molecular orientation in individual electrospun nanofibers measured via polarized Raman spectroscopy. *Polymer*. 49(13–14):3125–29

Berber S, Kwon YYY, Tomanek D, Tománek D. 2000. Unusually high thermal conductivity of carbon nanotubes. *Physical review letters*. 84(20):4613–16

Bhardwaj N, Kundu SC. 2010. Electrospinning: A fascinating fiber fabrication technique. *Biotechnology Advances*. 28(3):325–47

Bouchacourt M, Thevenot F. 1981. Analytical investigations in the BC system. *Journal of The Less-Common Metals*. 82(C):219–26

Bouchacourt M, Thevenot F. 1985. The correlation between the thermoelectric properties and stoichiometry in the boron carbide phase B_4C-$B_{10.5}C$. *Journal of Materials Science*. 20(4):1237–47

Brainerd JG, Jensen AG, Cumming LG, Batcher RR, Begun SG, Black HS, Grown GM, Burrows CR, Busignies H, Cady WG, Carter PS. 1949. Standards on Piezoelectric Crystals. *Proceedings of the IRE*. 37(12):1378–95

Buscema M, Island JO, Groenendijk DJ, Blanter SI, Steele GA, van der Zant HS, Castellanos-Gomez A. 2015. Photocurrent generation with two-dimensional van der Waals semiconductors. *Chem Soc Rev*. 44(11):3691–3718

Cahill DG. 1990. Thermal conductivity measurement from 30 to 750 K: the 3ω method. *Review of Scientific Instruments*. 61(2):802

Cahill DG. 2004. Analysis of heat flow in layered structures for time-domain thermoreflectance. *Review of Scientific Instruments*. 75(12):5119

Cahill DG, Braun P V, Chen G, Clarke DR, Fan S, Goodson KE, Keblinski P, King WP, Mahan GD, Majumdar A, Maris HJ, Phillpot SR, Pop E, Shi L. 2014. Nanoscale thermal transport. II. 2003–2012. *Applied Physics Reviews*. 1(1):11305

Cahill DG, Ford WK, Goodson KE, Mahan GD, Majumdar A, Maris HJ, Merlin R, Phillpot SR. 2003. Nanoscale thermal transport. *Journal of Applied Physics*. 93(2):793

Cai H, Chen B, Wang G, Soignard E, Khosravi A, Manca M, Marie X, Chang SLY, Urbaszek B, Tongay S. 2017. Synthesis of Highly Anisotropic Semiconducting GaTe Nanomaterials and Emerging Properties Enabled by Epitaxy. *Advanced Materials*. 29(8):1605551

Cai K, Nan C-W, Min X. 1999. The effect of silicon addition on thermoelectric properties of a B_4C ceramic. *Materials Science and Engineering: B*. 67(3):102–7

Canetta C, Guo S, Narayanaswamy A. 2014. Measuring thermal conductivity of polystyrene nanowires using the dual-cantilever technique. *Review of Scientific Instruments*. 85(10):104901

Canetta C, Narayanaswamy A. 2013. Measurement of optical coupling between adjacent bi-material microcantilevers. *Review of Scientific Instruments*. 84(10):105002

Caroff P, Dick KA, Johansson J, Messing ME, Deppert K, Samuelson L. 2009. Controlled polytypic and twin-plane superlattices in III–V nanowires. *Nature Nanotechnology*. 4(1):50–55

Caruso AN, Dowben PA, Balkir S, Schemm N, Osberg K, Fairchild RW, Flores OB, Balaz S, Harken AD, Robertson BW, Brand JI. 2006. The all boron carbide diode neutron detector: Comparison with theory. *Materials Science and Engineering: B*. 135(2):129–33

Chang C, Okawa D, Garcia H, Majumdar A, Zettl A. 2007. Nanotube Phonon Waveguide. *Physical Review Letters*. 99(4):45901

Chen J, Zhang G, Li B. 2011. A universal gauge for thermal conductivity of silicon nanowires with different cross sectional geometries. *Journal of Chemical Physics*. 135(20):1–8

Chen R, Hochbaum AI, Murphy P, Moore J, Yang P, Majumdar A. 2008. Thermal Conductance of Thin Silicon Nanowires. *Physical Review Letters*. 101(10):105501

Chen Y, Burgess T, An X, Mai Y-W, Tan HH, Zou J, Ringer SP, Jagadish C, Liao X. 2016. Effect of a High Density of Stacking Faults on the Young's Modulus of GaAs Nanowires. *Nano Letters*. 16(3):1911–16

Chen Y, Li L, Zhang C, Tuan C-C, Chen X, Gao J, Wong C-P. 2017. Controlling Kink Geometry in Nanowires Fabricated by Alternating Metal-Assisted Chemical Etching. *Nano Letters*. 17(2):1014–19

Choy CL. 1977. Thermal conductivity of polymers. *Polymer*. 18(10):984–1004

Choy CL, Leung WP. 1983. Thermal conductivity of ultradrawn polyethylene. *Journal of Polymer Science: Polymer Physics Edition*. 21(7):1243–46

Choy CL, Wong YW, Yang GW, Kanamoto T. 1999. Elastic modulus and thermal conductivity of ultradrawn polyethylene. *Journal of Polymer Science Part B: Polymer Physics*. 37(23):3359–67

Chung D-Y, Hogan T, Brazis P, Rocci-Lane M, Kannewurf K, Bastea M, Uher C. 2000. CsBi4Te6: A High-Performance Thermoelectric Material for Low-Temperature Applications. *Science (New York, N.Y.)*. 287(5455):1024–27

Coleman HW, Steele WG. 2009. *Experimentation, Validation, and Uncertainty Analysis for Engineers*. Hoboken, NJ, USA: John Wiley & Sons, Inc.

Costescu R, Wall M, Cahill D. 2003. Thermal conductance of epitaxial interfaces. *Physical Review B*. 67(5):54302

Dechaumphai E, Lu D, Kan JJ, Moon J, Fullerton EE, Liu Z, Chen R. 2014. Ultralow Thermal Conductivity of Multilayers with Highly Dissimilar Debye Temperatures. *Nano Letters*. 14(5):2448–55

Domnich V, Reynaud S, Haber RA, Chhowalla M. 2011. Boron Carbide: Structure, Properties, and Stability under Stress. *Journal of the American Ceramic Society*. 94(11):3605–28

Dresselhaus MS, Chen G, Tang MY, Yang RG, Lee H, Wang DZ, Ren ZF, Fleurial J-P, Gogna P. 2007. New Directions for Low-Dimensional Thermoelectric Materials. *Adv. Mater.* 19(8):1043–53

Emin D. 1988. Structure and single-phase regime of boron carbides. *Physical Review B*. 38(9):6041–55

Emin D. 1998. Vibrational contribution to the Seebeck coefficient of bipolaronic carriers in boron carbides. *Physica Status Solidi B*. 205(1):385–90

Emin D. 2006. Unusual properties of icosahedral boron-rich solids. *Journal of Solid State Chemistry*. 179(9):2791–98

Emin D, Howard IA, Green TA, Beckel CL. 1987. Microscopic Origin of the Composition-

Dependent Change of the Thermal Conductivity in Boron Carbides. *MRS Proceedings*. 97:83

Ero-Phillips O, Jenkins M, Stamboulis A. 2012. Tailoring Crystallinity of Electrospun Plla Fibres by Control of Electrospinning Parameters. *Polymers*. 4(4):1331–48

Ghosh S, Bao W, Nika DL, Subrina S, Pokatilov EP, Lau CN, Balandin AA. 2010. Dimensional crossover of thermal transport in few-layer graphene. *Nature Materials*. 9(7):555–58

Greiner A, Wendorff JH. 2007. Electrospinning: A fascinating method for the preparation of ultrathin fibers. *Angewandte Chemie - International Edition*. 46(30):5670–5703

Gu X, Li B, Yang R. 2016. Layer thickness-dependent phonon properties and thermal conductivity of MoS_2. *Journal of Applied Physics*. 119(8):85106

Guan Z, Cao B, Yang Y, Jiang Y, Li D, Xu TT. 2014. Observation of “hidden” planar defects in boron carbide nanowires and identification of their orientations. *Nanoscale Research Letters*. 9(1):30

Guan Z, Gutu T, Yang J, Yang Y, Zinn AA, Li D, Xu TT. 2012. Boron carbide nanowires: low temperature synthesis and structural and thermal conductivity characterization. *Journal of Materials Chemistry*. 22(19):9853–60

Gunjishima I, Akashi T, Goto T. 2001. Thermoelectric Properties of Single Crystalline B_4C Prepared by a Floating Zone Method. *MATERIALS TRANSACTIONS*. 42(7):1445–50

He Z, Nguyen HT, Duc Toan L, Pribat D. 2015. A detailed study of kinking in indium-catalyzed silicon nanowires. *CrystEngComm*. 17(33):6286–96

Henry A. 2014. THERMAL TRANSPORT IN POLYMERS. *Annual Review of Heat Transfer*. 17(N/A):485–520

Henry A, Chen G. 2008. High Thermal Conductivity of Single Polyethylene Chains Using Molecular Dynamics Simulations. *Physical Review Letters*. 101(23):235502

Henry A, Chen G. 2009. Anomalous heat conduction in polyethylene chains: Theory and molecular dynamics simulations. *Physical Review B*. 79(14):144305

Henry A, Chen G, Plimpton SJ, Thompson A. 2010. 1D-to-3D transition of phonon heat conduction in polyethylene using molecular dynamics simulations. *Physical Review B*. 82(14):144308

Hochbaum AI, Chen R, Delgado RD, Liang W, Garnett EC, Najarian M, Majumdar A, Yang P. 2008. Enhanced thermoelectric performance of rough silicon nanowires. *Nature*. 451(7175):163–67

Hone J, Whitney M, Piskoti C, Zettl A. 1999. Thermal conductivity of single-walled carbon nanotubes. *Physical Review B*. 59(4):R2514–16

Hong N, Langell M a., Liu J, Kizilkaya O, Adenwalla S. 2010. Ni doping of semiconducting boron carbide. *Journal of Applied Physics*. 107(2):24513

Howard IA, Beckel CL, Emin D. 1987. Bipolarons in boron icosahedra. *Physical Review B*. 35(6):2929–33

Hsiao T-K, Chang H-K, Liou S-C, Chu M-W, Lee S-C, Chang C-W. 2013. Observation of room-temperature ballistic thermal conduction persisting over 8.3 µm in SiGe nanowires. *Nature Nanotechnology*. 8(7):534–38

Hsin C-L, Wingert M, Huang C-W, Guo H, Shih T-J, Suh J, Wang K, Wu J, Wu W-W, Chen R. 2013. Phase transformation and thermoelectric properties of bismuth-telluride nanowires. *Nanoscale*. 5(11):4669

Huang H, Duan W. 2016. Topological insulators: Quasi-1D topological insulators. *Nature Materials*. 15(2):129–30

Hurley DC, Wolfe JP. 1985. Phonon focusing in cubic crystals. *Physical Review B*. 32(4):2568–87

Jang D, Li X, Gao H, Greer JR. 2012. Deformation mechanisms in nanotwinned metal nanopillars. *Nature Nanotechnology*. 7(9):594–601

Jiang J-W, Yang N, Wang B-S, Rabczuk T. 2013a. Modulation of Thermal Conductivity in Kinked Silicon Nanowires: Phonon Interchanging and Pinching Effects. *Nano Letters*. 13(4):1670–74

Jiang J-W, Zhao J-H, Rabczuk T. 2013b. Size-sensitive Young's modulus of kinked silicon nanowires. *Nanotechnology*. 24(18):185702

Jiang J-W, Zhao J, Zhou K, Rabczuk T. 2012a. Superior thermal conductivity and extremely high mechanical strength in polyethylene chains from ab initio calculation. *Journal of Applied Physics*. 111(12):124304

Jiang X, Tian B, Xiang J, Qian F, Zheng G, Wang H, Mai L, Lieber CM. 2011. Rational growth of branched nanowire heterostructures with synthetically encoded properties and function. *Proceedings of the National Academy of Sciences*. 108(30):12212–16

Jiang Z, Qing Q, Xie P, Gao R, Lieber CM. 2012b. Kinked p–n Junction Nanowire Probes for High Spatial Resolution Sensing and Intracellular Recording. *Nano Letters*. 12(3):1711–16

Joseph Kline R, McGehee MD, Toney MF. 2006. Highly oriented crystals at the buried interface in polythiophene thin-film transistors. *Nature Materials*. 5(3):222–28

Kanamoto T, Tsuruta a, Tanaka K, Takeda M, Porter RSS. 1988. Superdrawing of Ultrahigh Molecular Weight Polyethylene. 1. Effect of Techniques on Drawing of Single Crystal Mats. *Macromolecules*. 21:470–77

Kim G-H, Lee D, Shanker A, Shao L, Kwon MS, Gidley D, Kim J, Pipe KP. 2014. High thermal conductivity in amorphous polymer blends by engineered interchain interactions. *Nature Materials*. 14(3):295–300

Kim P, Shi L, Majumdar A, McEuen P. 2001. Thermal Transport Measurements of Individual Multiwalled Nanotubes. *Physical Review Letters*. 87(21):215502

Kim W. 2011. Thermal transport in individual thermoelectric nanowires: a review. *Materials Research Innovations*. 15(6):375–85

Kittel C. 2004. *Introduction to Solid State Physics*, Vol. 8th Editio. John Wiley & Sons, Inc

Klemens P. 1953. The Specific Heat and Thermal Conductivity of Graphite. *Australian Journal of Physics*. 6(4):405

Klemens PG. 1960. Thermal Resistance due to Point Defects at High Temperatures. *Physical Review*. 119(2):507–9

Kwon S, Wingert MC, Zheng J, Xiang J, Chen R. 2016. Thermal transport in Si and Ge nanostructures in the “confinement” regime. *Nanoscale*. 8(27):13155–67

Lagaron J., Dixon N., Reed W, Pastor J., Kip B. 1999. Morphological characterisation of the crystalline structure of cold-drawn HDPE used as a model material for the environmental stress cracking (ESC) phenomenon. *Polymer*. 40(10):2569–86

Lan Y, Minnich AJ, Chen G, Ren Z. 2010. Enhancement of Thermoelectric Figure-of-Merit by a Bulk Nanostructuring Approach. *Advanced Functional Materials*. 20(3):357–76

Lee EK, Yin L, Lee Y, Lee JJW, Lee SJ, Lee JJW, Cha SN, Whang D, Hwang GS, Hippalgaonkar K, Majumdar A, Yu C, Choi BL, Kim JM, Kim K. 2012. Large Thermoelectric Figure-of-Merits from SiGe Nanowires by Simultaneously Measuring Electrical and Thermal Transport Properties. *Nano Letters*. 12(6):2918–23

Lee J, Lee W, Lim J, Yu Y, Kong Q, Urban JJ, Yang P. 2016. Thermal Transport in Silicon Nanowires at High Temperature up to 700 K. *Nano Letters*. 16(7):4133–40

Li D, McGaughey AJH. 2015. Phonon Dynamics at Surfaces and Interfaces and Its Implications in Energy Transport in Nanostructured Materials—An opinion Paper. *Nanoscale and Microscale Thermophysical Engineering*. 19(2):166–82

Li D, Wang Y, Xia Y. 2003a. Electrospinning of Polymeric and Ceramic Nanofibers as Uniaxially Aligned Arrays. *Nano Letters*. 3(8):1167–71

Li D, Wu Y, Kim P, Shi L, Yang P, Majumdar A. 2003b. Thermal conductivity of individual silicon nanowires. *Applied Physics Letters*. 83(14):2934–36

Li D, Xia Y. 2004. Electrospinning of Nanofibers: Reinventing the Wheel? *Adv. Mater.* 16(14):1151–70

Li P, Hu L, McGaughey AJH, Shen S. 2014. Crystalline Polyethylene Nanofibers with the Theoretical Limit of Young's Modulus. *Advanced Materials*. 26(7):1065–70

Liang D, Hsiao BS, Chu B. 2007. Functional electrospun nanofibrous scaffolds for biomedical applications. *Advanced Drug Delivery Reviews*. 59(14):1392–1412

Lin Y-M, Dresselhaus MS. 2003. Thermoelectric properties of superlattice nanowires. *Physical Review B*. 68(7):75304

Lindsay L, Broido DA. 2012. Theory of thermal transport in multilayer hexagonal boron nitride and nanotubes. *Physical Review B*. 85(3):35436

Liu C, Hsu P-C, Lee H-W, Ye M, Zheng G, Liu N, Li W, Cui Y. 2015. Transparent air filter for high-efficiency PM2.5 capture. *Nature communications*. 6:6205

Liu C. 2001. Conductivity transition of semiconducting boron carbide by doping. *Materials Letters*. 49(5):308–12

Liu CHH. 2000. Structure and properties of boron carbide with aluminum incorporation. *Materials Science and Engineering: B*. 72(1):23–26

Liu D, Xie R, Yang N, Li B, Thong JTL. 2014. Profiling Nanowire Thermal Resistance with a Spatial Resolution of Nanometers. *Nano Letters*. 14(2):806–12

Liu J, Li T, Hu Y, Zhang X. 2017. Benchmark study of the length dependent thermal conductivity of individual suspended, pristine SWCNTs. *Nanoscale*. 9(4):1496–1501

Liu J, Yang R. 2012. Length-dependent thermal conductivity of single extended polymer chains. *Physical Review B*. 86(10):104307

Liu L-C, Huang M-J, Yang R, Jeng M-S, Yang C-C. 2009. Curvature effect on the phonon thermal conductivity of dielectric nanowires. *Journal of Applied Physics*. 105(10):104313

Liu X, Liu J, Antipina LY, Hu J, Yue C, Sanchez AM, Sorokin PB, Mao Z, Wei J. 2016. Direct Fabrication of Functional Ultrathin Single-Crystal Nanowires from Quasi-One-Dimensional van der Waals Crystals. *Nano Letters*. 16(10):6188–95

Long YZ, Duvail JL, Li MM, Gu C, Liu Z, Ringer SP. 2010. Electrical Conductivity Studies on Individual Conjugated Polymer Nanowires: Two-Probe and Four-Probe Results. *Nanoscale Research Letters*. 5(1):237–42

Lyeo H-K, Cahill DG. 2006. Thermal conductance of interfaces between highly dissimilar materials. *Physical Review B*. 73(14):144301

Ma J, Zhang Q, Mayo A, Mu R, Bellan L, Li D. 2015a. Thermal Conductivity of Individual Electrospun Polymer Nanofibers. *Volume 8B: Heat Transfer and Thermal Engineering*. V08BT10A031. ASME

Ma J, Zhang Q, Mayo A, Ni Z, Yi H, Chen Y, Mu R, Bellan LM, Li D. 2015b. Thermal conductivity of electrospun polyethylene nanofibers. *Nanoscale*. 7(40):16899–908

Ma J, Zhang Q, Zhang Y, Zhou L, Yang J, Ni Z. 2016. A rapid and simple method to draw polyethylene nanofibers with enhanced thermal conductivity. *Applied Physics Letters*. 109(3):33101

Mackinnon IDR, Aselage T, Van Deusen SB. 1986. High resolution imaging of boron carbide microstructures. *AIP Conference Proceedings*. 140:114–20

Maldovan M. 2011. Micro to nano scale thermal energy conduction in semiconductor thin films. *Journal of Applied Physics*. 110(3):34308

Martin PN, Aksamija Z, Pop E, Ravaioli U. 2010. Reduced thermal conductivity in nanoengineered rough Ge and GaAs nanowires. *Nano letters*. 10(4):1120–24

Mavrokefalos A, Pettes MT, Zhou F, Shi L. 2007. Four-probe measurements of the in-plane thermoelectric properties of nanofilms. *Review of Scientific Instruments*. 78(3):34901

McClellan KJ, Chu F, Roper JM, Shindo I. 2001. Room temperature single crystal elastic constants of boron carbide. *Journal of Materials Science*. 36(14):3403–7

McCurdy AK. 1974. Phonon focusing and phonon conduction in hexagonal crystals in the boundary-scattering regime. *Physical Review B*. 9(2):466–80

Medwick PA, Fischer HE, Pohl RO. 1994. Thermal conductivity and specific heat of boron carbides. *Journal of Alloys and Compounds*. 203(C):67–75

Mingo N, Yang L, Li D, Majumdar A. 2003. Predicting the Thermal Conductivity of Si and Ge Nanowires. *Nano Letters*. 3(12):1713–16

Moore AL, Pettes MT, Zhou F, Shi L. 2009. Thermal conductivity suppression in bismuth nanowires. *Journal of Applied Physics*. 106(3):34310

Moore AL, Saha SK, Prasher RS, Shi L. 2008. Phonon backscattering and thermal conductivity suppression in sawtooth nanowires. *Applied Physics Letters*. 93(8):83112

Moore AL, Shi L. 2011. On errors in thermal conductivity measurements of suspended and supported nanowires using micro-thermometer devices from low to high temperatures. *Measurement Science and Technology*. 22(1):15103

Murphy KF, Piccione B, Zanjani MB, Lukes JR, Gianola DS. 2014. Strain- and defect-mediated thermal conductivity in silicon nanowires. *Nano Letters*. 14(7):3785–92

Nain AS, Wong JC, Amon C, Sitti M. 2006. Drawing suspended polymer micro-/nanofibers using glass micropipettes. *Applied Physics Letters*. 89(18):183105

Naraghi M, Chasiotis I, Kahn H, Wen Y, Dzenis Y. 2007. Mechanical deformation and failure of electrospun polyacrylonitrile nanofibers as a function of strain rate. *Applied Physics Letters*. 91(15):57–60

Ning W, Yu H, Liu Y, Han Y, Wang N, Yang J, Du H, Zhang C, Mao Z, Liu Y, Tian M, Zhang Y. 2015. Superconductor–Insulator Transition in Quasi-One-Dimensional Single-Crystal Nb_2PdS_5 Nanowires. *Nano Letters*. 15(2):869–75

Nishi Y, Arita Y, Matsui T, Nagasaki T. 2002. Isotope Effects on Thermal Conductivity of Boron Carbide. *Journal of Nuclear Science and Technology*. 39(4):391–94

Novoselov KS, Geim AK, Morozov S V., Jiang D, Zhang Y, Dubonos S V., Grigorieva I V., Alexandr A. Firsov. 2004. Electric Field Effect in Atomically Thin Carbon Films. *Science (New York, N.Y.)*. 306(5696):666–69

Nye JF. 1985. *Physical Properties of Crystals: Their Representation by Tensors and Matrices*. Oxford University Press

Pettes MT. 2011. *Experimental Investigations of Thermal Transport in Carbon Nanotubes, Graphene and Nanoscale Point Contacts*. The University of Texas at Austin

Pevzner A, Engel Y, Elnathan R, Tsukernik A, Barkay Z, Patolsky F. 2012. Confinement-Guided Shaping of Semiconductor Nanowires and Nanoribbons: “Writing with Nanowires.” *Nano Letters*. 12(1):7–12

Pop E, Mann D, Wang Q, Goodson K, Dai H. 2006. Thermal Conductance of an Individual Single-Wall Carbon Nanotube above Room Temperature. *Nano Letters*. 6(1):96–100

Pop E, Varshney V, Roy AK. 2012. Thermal properties of graphene: Fundamentals and applications. *MRS Bulletin*. 37(12):1273–81

Porter A, Tran C, Sansoz F. 2016. Intrinsic nanotwin effect on thermal boundary conductance in bulk and single-nanowire twinning superlattices. *Physical Review B*. 93(19):195431

Proctor JE, Bhakhri V, Hao R, Prior TJ, Scheler T, Gregoryanz E, Chhowalla M, Giulani F. 2015. Stabilization of boron carbide via silicon doping. *J. Phys. Condens. Matter*. 27(1):15401

Pye AJ, Faux DA, Kearney MJ. 2015. Coherent thermoelectric transport in single, double, and U-bend structures. *Journal of Applied Physics*. 117(6):64312

Qing Q, Jiang Z, Xu L, Gao R, Mai L, Lieber CM. 2013. Free-standing kinked nanowire transistor probes for targeted intracellular recording in three dimensions. *Nature Nanotechnology*. 9(2):142–47

Sansoz F. 2011. Surface Faceting Dependence of Thermal Transport in Silicon Nanowires. *Nano Letters*. 11(12):5378–82

Sato H, Shimoyama M, Kamiya T, Amari T, Aic S, Ninomiya T, Siesler HW, Ozaki Y. 2002. Raman spectra of high-density, low-density, and linear low-density polyethylene pellets and prediction of their physical properties by multivariate data analysis. *Journal of Applied Polymer Science*. 86(2):443–48

Schmechel R, Werheit H. 1999. Correlation between structural defects and electronic properties of icosahedral boron-rich solids. *Journal of Physics: Condensed Matter*. 11(35):6803–13

Schmechel R, Werheit H. 2000. Structural Defects of Some Icosahedral Boron-Rich Solids and Their Correlation with the Electronic Properties. *J. Solid State Chem.* 154(1):61–67

Sellan DP, Turney JE, McGaughey AJH, Amon CH. 2010. Cross-plane phonon transport in thin films. *Journal of Applied Physics*. 108(11):113524

Shen S, Henry A, Tong J, Zheng R, Chen G. 2010. Polyethylene nanofibres with very high thermal conductivities. *Nature Nanotechnology*. 5(4):251–55

Shi L. 2012. Thermal and Thermoelectric Transport in Nanostructures and Low-Dimensional Systems. *Nanoscale and Microscale Thermophysical Engineering*. 16(2):79–116

Shi L, Hao Q, Yu C, Mingo N, Kong X, Wang ZL. 2004. Thermal conductivities of individual tin dioxide nanobelts. *Applied Physics Letters*. 84(14):2638

Shi L, Li D, Yu C, Jang W, Kim D, Yao Z, Kim P, Majumdar A. 2003. Measuring Thermal and Thermoelectric Properties of One-Dimensional Nanostructures Using a Microfabricated Device. *Journal of Heat Transfer*. 125(5):881–88

Shin HS, Jeon SG, Yu J, Kim Y-S, Park HM, Song JY. 2014. Twin-driven thermoelectric figure-of-merit enhancement of Bi_2Te_3 nanowires. *Nanoscale*. 6(11):6158

Singh V, Bougher TL, Weathers A, Cai Y, Bi K, Pettes MT, McMenamin S a, Lv W, Resler DP, Gattuso TR, Altman DH, Sandhage KH, Shi L, Henry A, Cola BA. 2014. High thermal conductivity of chain-oriented amorphous polythiophene. *Nature Nanotechnology*. 9(5):384–90

Smith B, Vermeersch B, Carrete J, Ou E, Kim J, Mingo N, Akinwande D, Shi L. 2017. Temperature and Thickness Dependences of the Anisotropic In-Plane Thermal Conductivity of Black Phosphorus. *Advanced Materials*. 29(5):1603756

Stolyarov MA, Liu G, Bloodgood MA, Aytan E, Jiang C, Samnakay R, Salguero TT, Nika DL, Rumyantsev SL, Shur MS, Bozhilov KN, Balandin AA, Click M. 2016. Breakdown current density in h-BN-capped quasi-1D $TaSe_3$ metallic nanowires: prospects of interconnect applications. *Nanoscale*. 8(34):15774–82

Stoner R, Maris H. 1993. Kapitza conductance and heat flow between solids at temperatures from 50 to 300 K. *Physical Review B*. 48(22):16373–87

Strobl GR, Hagedorn W. 1978. Raman spectroscopic method for determining the crystallinity of polyethylene. *Journal of Polymer Science: Polymer Physics Edition*. 16(7):1181–93

Suri AK, Subramanian C, Sonber JK, Murthy TSRC. 2010. Synthesis and consolidation of boron carbide: a review. *International Materials Reviews*. 55(1):4–40

Takemoto H, Fugane K, Yan P, Drennan J, Saito M, Mori T, Yamamura H. 2014. Reduction of thermal conductivity in dually doped ZnO by design of three-dimensional stacking faults. *RSC Advances*. 4(6):2661

Tallant DR, Aselage TL, Campbell AN, Emin D. 1989. Boron carbide structure by Raman spectroscopy. *Physical Review B*. 40(8):5649–56

Taylor DE, McCauley JW, Wright TW. 2012. The effects of stoichiometry on the mechanical properties of icosahedral boron carbide under loading. *Journal of Physics: Condensed Matter*. 24(50):505402

Thelander C, Caroff P, Plissard S, Dey AW, Dick KA. 2011. Effects of Crystal Phase Mixing on the Electrical Properties of InAs Nanowires. *Nano Letters*. 11(6):2424–29

Thévenot F. 1990. Boron carbide—A comprehensive review. *J. Eur. Ceram. Soc.* 6:205–25

Thompson WD, Nandur A, White BE. 2016. Thermal transport in Cu_2ZnSnS_4 thin films. *Journal of Applied Physics*. 119(9):95108

Tian B, Xie P, Kempa TJ, Bell DC, Lieber CM. 2009. Single-crystalline kinked semiconductor nanowire superstructures. *Nature Nanotechnology*. 4(12):824–29

Utke I, Hoffmann P, Melngailis J. 2008. Gas-assisted focused electron beam and ion beam processing and fabrication. *Journal of Vacuum Science & Technology B: Microelectronics and Nanometer Structures*. 26(4):1197

Volz SG, Chen G. 1999. Molecular dynamics simulation of thermal conductivity of silicon nanowires. *Applied Physics Letters*. 75(14):2056–58

Wan C, Wang Y, Norimatsu W, Kusunoki M, Koumoto K. 2012. Nanoscale stacking faults induced low thermal conductivity in thermoelectric layered metal sulfides. *Applied Physics Letters*. 100(10):2–6

Wang LH, Ottani S, Porter RS. 1991a. Two-stage drawing of high-molecular-weight polyethylene reactor powder. *Polymer*. 32(10):1776–81

Wang LH, Porter RS, Stidham HD, Hsu SL. 1991b. Raman spectroscopic characterization of the morphology of polyethylene reactor powder. *Macromolecules*. 24(20):5535–38

Wang X, Ho V, Segalman RA, Cahill DG. 2013. Thermal conductivity of high-modulus polymer fibers. *Macromolecules*. 46(12):4937–43

Wang YK, Waldnam D, Lasch JE, Stein RS, Hsu SL. 1982. Raman spectroscopic study of highly deformed polyethylene. *Macromolecules*. 15(5):1452–54

Weathers A, Shi L. 2013. THERMAL TRANSPORT MEASUREMENT TECHNIQUES FOR NANOWIRES AND NANOTUBES. *Annual Review of Heat Transfer*. 16(1):101–34

Wei Z, Wehmeyer G, Dames C, Chen Y. 2016. Geometric tuning of thermal conductivity in three-dimensional anisotropic phononic crystals. *Nanoscale*. 8(37):16612–20

Werheit H. 2006. Thermoelectric Properties of Boron-Rich Solids and their Possibilities of Technical Application. *2006 25th International Conference on Thermoelectrics*, pp. 159–63. IEEE

Werheit H. 2009. Present knowledge of electronic properties and charge transport of icosahedral boron-rich solids. *Journal of Physics: Conference Series*. 176:12019

Werheit H, Kuhlmann U. 2011. Superconductivity in boron carbide? Clarification by low-temperature MIR/FIR spectra. *Journal of Physics: Condensed Matter*. 23(43):435501

Werheit H, Kuhlmann U, Herstell B, Winkelbauer W. 2009. Reliable measurement of Seebeck coefficient in semiconductors. *Journal of Physics: Conference Series*. 176:12037

Werheit H, Leithe-Jasper A, Tanaka T, Rotter HW, Schwetz KA. 2004. Some properties of single-crystal boron carbide. *Journal of Solid State Chemistry*. 177(2):575–79

Werheit H, Shalamberidze S. 2012. Advanced microstructure of boron carbide. *Journal of Physics: Condensed Matter*. 24:385406

Wingert MC, Chen ZCY, Dechaumphai E, Moon J, Kim J, Xiang J, Chen R. 2011. Thermal Conductivity of Ge and Ge–Si Core–Shell Nanowires in the Phonon Confinement Regime. *Nano Letters*. 11(12):5507–13

Wingert MC, Chen ZCY, Kwon S, Xiang J, Chen R. 2012. Ultra-sensitive thermal conductance measurement of one-dimensional nanostructures enhanced by differential bridge. *Review of Scientific Instruments*. 83(2):24901

Wingert MC, Kwon S, Hu M, Poulikakos D, Xiang J, Chen R. 2015. Sub-amorphous Thermal Conductivity in Ultrathin Crystalline Silicon Nanotubes. *Nano Letters*. 15(4):2605–11

Wolfe JP. 1998. *Imaging Phonons: Acoustic Wave Propagation in Solids*. Cambridge University Press, Cambridge

Wood C, Emin D, Gray PE. 1985. Thermal conductivity behavior of boron carbides. *Physical Review B*. 31(10):6811–14

Xie KY, An Q, Sato T, Breen AJ, Ringer SP, Goddard WA, Cairney JM, Hemker KJ. 2016. Breaking the icosahedra in boron carbide. *Proceedings of the National Academy of Sciences*. 113(43):12012–16

Xiong S, Kosevich Y a., Sääskilahti K, Ni Y, Volz S. 2014. Tunable thermal conductivity in silicon twinning superlattice nanowires. *Physical Review B*. 90(19):195439

Yan R, Gargas D, Yang P. 2009. Nanowire photonics. *Nature Photonics*. 3(10):569–76

Yang J, Shen M, Yang Y, Evans WJ, Wei Z, Chen W, Zinn AA, Chen Y, Prasher R, Xu TT, Keblinski P, Li D. 2014. Phonon Transport through Point Contacts between Graphitic Nanomaterials. *Physical Review Letters*. 112(20):205901

Yang J, Waltermire S, Chen Y, Zinn AA, Xu TT, Li D. 2010. Contact thermal resistance between individual multiwall carbon nanotubes. *Applied Physics Letters*. 96(2):23109

Yang J, Yang Y, Waltermire SW, Gutu T, Zinn AA, Xu TT, Chen Y, Li D. 2011. Measurement of the Intrinsic Thermal Conductivity of a Multiwalled Carbon Nanotube and Its Contact Thermal Resistance with the Substrate. *Small*. 7(16):2334–40

Yang J, Yang Y, Waltermire SW, Wu X, Zhang H, Gutu T, Jiang Y, Chen Y, Zinn A a, Prasher R, Xu TT, Li D. 2012. Enhanced and switchable nanoscale thermal conduction due to van der Waals interfaces. *Nature Nanotechnology*. 7(2):91–95

Yang L, Yang Y, Zhang Q, Zhang Y, Jiang Y, Guan Z, Gerboth M, Yang J, Chen Y, Greg Walker D, Xu TT, Li D. 2016. Thermal conductivity of individual silicon nanoribbons. *Nanoscale*. 8(41):17895–901

Yu C, Shi L, Yao Z, Li D, Majumdar A. 2005. Thermal Conductance and Thermopower of an Individual Single-Wall Carbon Nanotube. *Nano Letters*. 5(9):1842–46

Zhan HF, Zhang YY, Bell JM, Gu YT. 2014. Thermal conductivity of Si nanowires with faulted stacking layers. *Journal of Physics D: Applied Physics*. 47(1):15303

Zhang Q, Cui Z, Wei Z, Chang SY, Yang L, Zhao Y, Yang Y, Guan Z, Jiang Y, Fowlkes J, Yang

J, Xu D, Chen Y, Xu TT, Li D. 2017. Defect Facilitated Phonon Transport through Kinks in Boron Carbide Nanowires. *Nano Letters*. 17(6):3550–55

Zhang T, Luo T. 2012. Morphology-influenced thermal conductivity of polyethylene single chains and crystalline fibers. *Journal of Applied Physics*. 112(9):1–5

Zhang T, Luo T. 2015. Giant Thermal Rectification from Polyethylene Nanofiber Thermal Diodes. *Small*. 11(36):4657–65

Zhang T, Luo T. 2016. Role of Chain Morphology and Stiffness in Thermal Conductivity of Amorphous Polymers. *The Journal of Physical Chemistry B*. 120(4):803–12

Zhao L-D, Lo S-H, Zhang Y, Sun H, Tan G, Uher C, Wolverton C, Dravid VP, Kanatzidis MG. 2014. Ultralow thermal conductivity and high thermoelectric figure of merit in SnSe crystals. *Nature*. 508(7496):373–77

Zhao LD, Zhang BP, Li JF, Zhang HL, Liu WS. 2008. Enhanced thermoelectric and mechanical properties in textured n-type Bi_2Te_3 prepared by spark plasma sintering. *Solid State Sciences*. 10(5):651–58

Zheng J, Wingert MC, Dechaumphai E, Chen R. 2013. Sub-picowatt/kelvin resistive thermometry for probing nanoscale thermal transport. *Review of Scientific Instruments*. 84(11):114901

Zhong Z, Wingert MC, Strzalka J, Wang H-H, Sun T, Wang J, Chen R, Jiang Z. 2014. Structure-induced enhancement of thermal conductivities in electrospun polymer nanofibers. *Nanoscale*. 6(14):8283

Zhou J, Yang R. 2011. Ballistic thermoelectricity in double-bend nanowires. *Applied Physics Letters*. 98(17):57–60